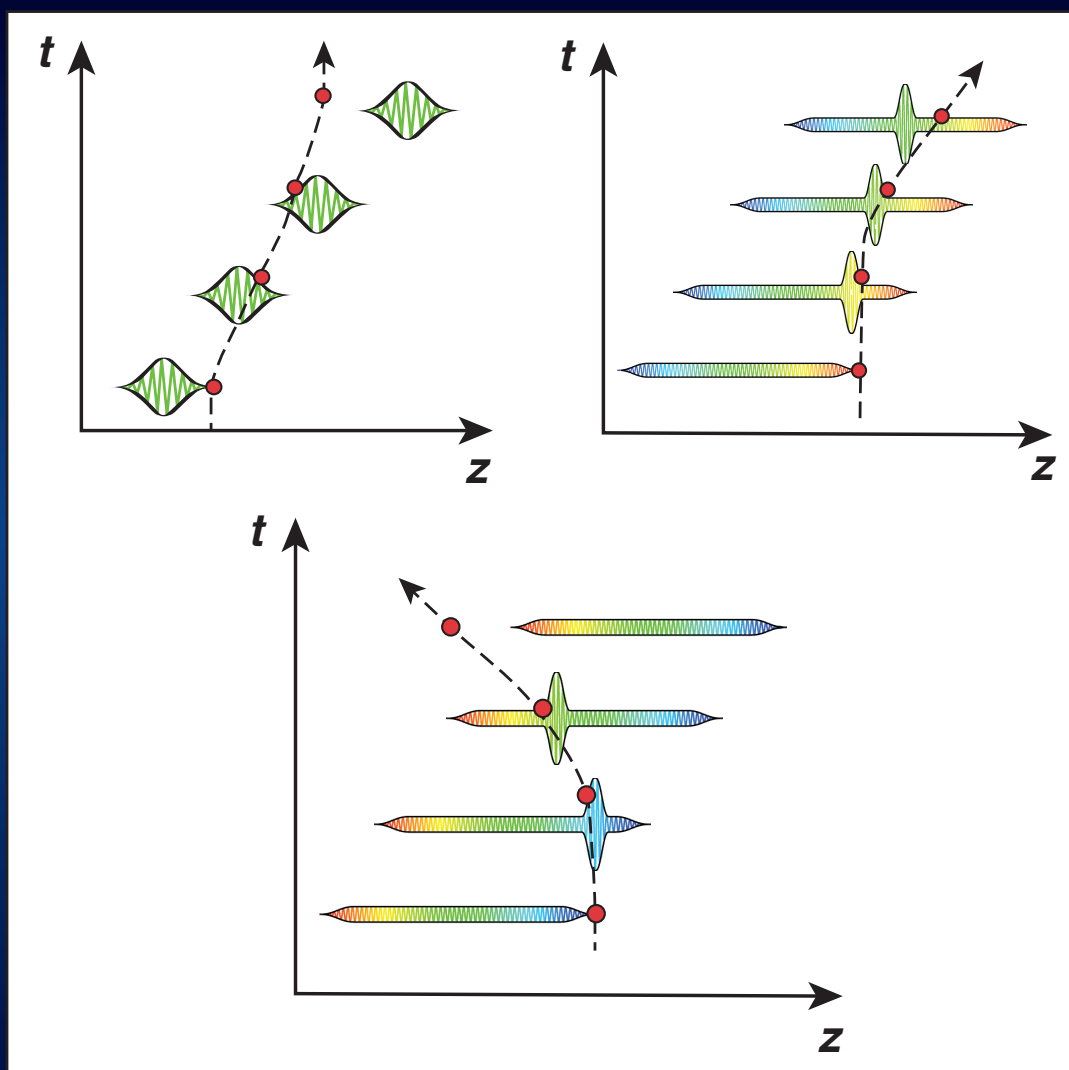


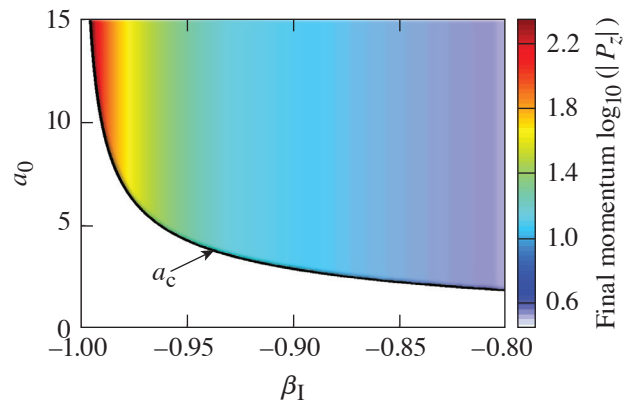
LLE Review

Quarterly Report



About the Cover:

The cover depicts a new vacuum-acceleration technique enabled by the subluminal intensity peaks of flying-focus pulses. The image on the top left shows a typical luminal intensity peak in vacuum. The electron, shown as a red dot, experiences equal and opposite ponderomotive accelerations on the leading and falling edges of the pulse, respectively, and gains no net energy. The image on the top right shows a flying focus with a subluminal intensity peak. After forward acceleration in the leading edge of the intensity peak, the electron outruns the peak and retains the energy it gained. The bottom image inset shows a negatively chirped flying focus with a subluminal intensity peak that travels in the opposite direction of the pulse. After backward acceleration in the leading edge, the electron outruns the intensity peak and retains the energy it gained.



The image at the right shows the final momentum of an electron accelerated in a backward-propagating flying-focus intensity peak. Below a cutoff-normalized vector potential ($a_0 = eA_0/m_e c$), an electron acquires a velocity insufficient to outrun the intensity peak and gains no net energy. Above the cutoff normalized vector potential, an accelerated electron is reflected from and will outrun the intensity peak, retaining the energy it gained, and the final momentum is independent of the maximum value of the normalized vector potential.

This report was prepared as an account of work conducted by the Laboratory for Laser Energetics and sponsored by New York State Energy Research and Development Authority, the University of Rochester, the U.S. Department of Energy, and other agencies. Neither the above-named sponsors nor any of their employees makes any warranty, expressed or implied, or assumes any legal liability or responsibility for the accuracy, completeness, or usefulness of any information, apparatus, product, or process disclosed, or represents that its use would not infringe privately owned rights. Reference herein to any specific commercial product, process, or service by trade name, mark, manufacturer, or otherwise, does not necessarily constitute or imply its endorsement, recommendation, or favoring

by the United States Government or any agency thereof or any other sponsor. Results reported in the LLE Review should not be taken as necessarily final results as they represent active research. The views and opinions of authors expressed herein do not necessarily state or reflect those of any of the above sponsoring entities.

The work described in this volume includes current research at the Laboratory for Laser Energetics, which is supported by New York State Energy Research and Development Authority, the University of Rochester, the U.S. Department of Energy Office of Inertial Confinement Fusion under Cooperative Agreement No. DE-NA0003856, and other agencies.

Printed in the United States of America

Available from

National Technical Information Services
U.S. Department of Commerce
5285 Port Royal Road
Springfield, VA 22161
www.ntis.gov

For questions or comments, contact Jessica L. Shaw, Editor, Laboratory for Laser Energetics, 250 East River Road, Rochester, NY 14623-1299, (585) 276-5618.

www.lle.rochester.edu

LLE Review



Quarterly Report

Contents

IN BRIEF	iii
INERTIAL CONFINEMENT FUSION	
Probing In-Flight Shell Breakup in DT Cryogenic Implosions on OMEGA.....	97
First Temperature and Velocity Measurements of the Dense Fuel Layer in Inertial Confinement Fusion Experiments	100
Self-Radiography of Imploded Shells on OMEGA Based on Additive-Free Multi-Monochromatic Continuum Spectral Analysis	103
Principal Factors in the Performance of Indirect-Drive Laser-Fusion Experiments.....	106
Experiments to Explore the Influence of Pulse Shaping at the National Ignition Facility.....	112
Deficiencies in Compression and Yield in X-Ray–Driven Implosions	118
Azimuthal Uniformity of Cylindrical Implosions on OMEGA	124
Characterizing Laser Preheat for Laser-Driven Magnetized Liner Inertial Fusion Using Soft X-Ray Emission	130
Constraining Physical Models at Gigabar Pressures.....	138
Molecular Dynamics Simulations Reveal Hydrogen Streaming upon Release from Polystyrene Shocked to Inertial Confinement Fusion Conditions.....	141
PLASMA AND ULTRAFAST PHYSICS	
Impact of Spatiotemporal Smoothing on the Two-Plasmon–Decay Instability	143
Vacuum Acceleration of Electrons in a Dynamic Laser Pulse	146

HIGH-ENERGY-DENSITY PHYSICS

Equation of State of CO ₂ Shock Compressed to 1 TPa	149
Shock-Compressed Silicon: Hugoniot and Sound Speed to 2100 GPa	153
Thermal Effects on the Electronic Properties of Sodium Electride Under High Pressures ...	156

DIAGNOSTIC SCIENCE AND DETECTORS

Optimization of a Short-Pulse–Driven Si He _α Soft X-Ray Backlighter.....	159
High-Resolution X-Ray Radiography with Fresnel Zone Plates on the OMEGA and OMEGA EP Laser Systems	161

LASER TECHNOLOGY AND DEVELOPMENT

Overcoming Gas Ionization Limitations with Divided-Pulse Nonlinear Compression	163
--	-----

LASER FACILITY REPORT

FY20 Q3 Laser Facility Report	166
-------------------------------------	-----

PUBLICATIONS AND CONFERENCE PRESENTATIONS

In Brief

This volume of LLE Review 163 covers the period from April–June 2020. Articles appearing in this volume are the principal summarized results for long-form research articles. Readers seeing a more-detailed account of research activities are invited to seek out the primary materials appear in print, detailed in the publications and presentations section at the end of this volume.

Highlights of research presented in this volume include:

- R. C. Shah *et al.* characterize the onset of core x-ray emission from gated images of DT cryogenic implosions (p. 97). This onset is used to diagnose conditions at the start of deceleration of the shell and suggests that other perturbations, not included in models, cause decompression in more-stable, higher-adiabat implosions.
- O. M. Mannion *et al.* made the first temperature and velocity measurements of the shell in cryogenic implosions using the emitted neutron-energy spectrum (p. 100). These measurements, along with areal-density measurements of the shell, now provide a complete set of hydrodynamic properties of the dense fuel layer near peak compression.
- R. Epstein *et al.* develop a method where cryogenic implosions can be self-radiographed by their own core spectral emission without the need for spectral additives (p. 103).
- C. A. Thomas *et al.* analyze implosions on the “Big Foot” Platform the National Ignition Facility and find that performance can be described by a simple function of the laser energy per unit mass, target scale, and implosion symmetry (p. 106).
- C. A. Thomas *et al.* also study implosions with different pulse shapes and find expressions the primary neutron yield and the neutron down-scatter ratio as functions of the laser energy per unit mass, target scale, implosion symmetry, and adiabat (p. 112).
- In addition, C. A. Thomas *et al.* find that the ion temperature, hot-spot areal density, and neutron yield implosion metrics for implosions using the Big Foot Platform are monotonic in laser energy (p. 118). Calculations agree well if the adiabat is increased by a factor of 1.4 relative to expectations.
- D. H. Barnak *et al.* completed analytical calculations that show that shifting the pointing of the OMEGA laser can eliminate the mode-5 perturbation in cylindrical implosions on OMEGA (p. 124).
- D. H. Barnak *et al.* also investigate measurements of the laser entrance hole window disassembly in terms of total emitted x-ray energy and compare this to other measurements and modeling results (p. 130).
- J. J. Ruby *et al.* present an application of Bayesian inference to derive quantitative physical information from integrated high-energy-density experiments (p. 138).
- S. Zhang and S. X. Hu apply a novel approach using many-body reactive force fields combined with first-principle ionization models to reveal species separation and hydrogen stream out of the CH upon shock release from inertial confinement fusion shells (p. 141).

- D. Turnbull *et al.* use a hot-spot model based on speckle statistics and simulation results from *LPSE* to explain higher levels of hot electrons from two-plasmon decay are observed when smoothing by spectral dispersion is turned off in direct-drive fusion experiments on OMEGA (p. 143).
- D. Ramsey *et al.* present a novel mechanism for the first vacuum acceleration of electrons in a single planar-like laser pulse in either the forward or backward direction (p. 146).
- L. E. Crandall *et al.* extend pressure and density measurements of the initially liquid and initially solid CO₂ Hugoniot to 1 TPa and provide the first temperature measurements of shocked CO₂ to 93,000 K (p. 149). They also propose a fluid phase diagram comprising at least three regimes to describe all existing shocked CO₂ data.
- B. Henderson *et al.* present the principal Hugoniot and sound-speed data for silicon shocked to 320 to 2100 GPa (p. 153).
- R. Paul *et al.* use density functional theory to perform molecular dynamics and electro-optical calculations to study the effects of thermal excitations on the electronic properties of electride sodium (p. 156).
- C. Stoeckl *et al.* investigate a number of approaches to increase the brightness of x-ray backlighters and find that silicon targets with a CH shield showed the best performance (p. 159).
- F. J. Marshall *et al.* report on the development of Fresnel zone plates (FZP's) to image x rays emitted by laser-generated plasma on OMEGA and OMEGA EP and show FZP results from *Revolver* experiments (p. 161).
- G. W. Jenkins, C. Feng, and J. Bromage examine the limits on hollow-core-fiber energy scaling and simulate divided-pulse nonlinear compression, which is a method to overcome those limits (p. 163).
- J. Puth *et al.* summarize operations of the Omega Laser Facility during the third quarter of FY20 (p. 166).

Jessica L. Shaw
Editor

Probing In-Flight Shell Breakup in DT Cryogenic Implosions on OMEGA

R. C. Shah,¹ S. X. Hu,¹ I. V. Igumenshchev,¹ J. Baltazar,¹ D. Cao,¹ C. J. Forrest,¹ V. N. Goncharov,¹ V. Gopaldaswamy,¹ D. Patel,¹ F. Philippe,² W. Theobald,¹ and S. P. Regan¹

¹Laboratory for Laser Energetics, University of Rochester

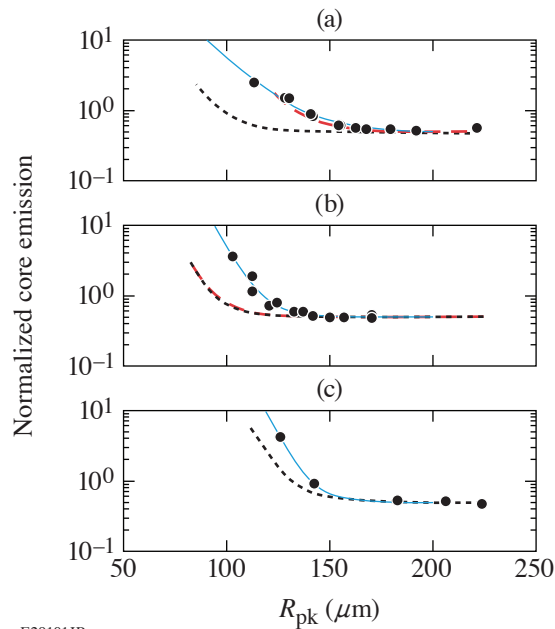
²Commissariat à l'énergie atomique et aux énergies alternatives, France

On the 30-kJ OMEGA laser, experiments are conducted on spherical implosions to create conditions relevant to inertial confinement fusion. Plastic capsules (~1 mm in diameter) containing a cryogenic shell of solid hydrogen fuel are directly imploded by ~20 TW of laser power arriving via 60 beams. The dense shell acts as a piston to create a fusion-relevant pressure (~100 Gbar) and temperature (~3 to 5 keV) in DT plasma termed the “hot spot.” The OMEGA experiments are interpreted by hydrodynamic scaling to the ~2-MJ National Ignition Facility for which the implosion dimensions would be large enough for hot-spot fusion reactions to cause runaway self-heating. Substantial progress has occurred¹ but the hot-spot conditions are not yet sufficient to trigger a self-sustained fusion reaction.²

Hot-spot performance is sensitive to the in-flight shell density ρ_{sh} , which, along with the shell velocity v_{sh} , determines the dynamic pressure of the imploding shell $P_{\text{d}} = \rho_{\text{sh}} v_{\text{sh}}^2$. The dynamic pressure determines the compressive work done to create the hot-spot pressure $P_{\text{hs}} \sim P_{\text{d}}^{5/3}$ (Ref. 3). A fundamental limit on the shell density arises from entropy, which is determined in direct-drive implosions mainly by laser pulse shape and resulting shocks. It is characterized by adiabat α defined as the ratio of the pressure to the Fermi-degenerate pressure at the shell density. However, the ablation surface is hydrodynamically unstable to perturbations,⁴ and implosions having a higher adiabat tend to be more robust due to reduced instability growth rates and a lower-density, thicker shell. A dominant source of perturbations in direct-drive implosions is expected to be laser speckle or laser imprinting.^{5–7}

The instability growth that breaks up the high-density shell leads to a relaxed density profile. A signature of the additional mass entering the hot-spot region is an increase of the early production of hot-spot soft x-ray emission. In this summary we interpret the onset of hot-spot x-ray self-emission from gated images of DT cryogenic implosions. Whereas the advance in onset of emission is well matched by imprint as calculated by the 3-D radiation-hydrodynamic code *ASTER*^{8,9} for a low-adiabat implosion, this is not the case for more-stable, higher-adiabat implosions. The results suggest that other perturbations, not included in models, cause decompression of more-stable implosions.

We first consider three DT cryogenic implosions with α of 1.7, 3.0, and 5.5 (also referred herein as low-, mid-, and high-stability). For the highest-adiabat implosion the cryogenic layer was 30% thicker, thereby further augmenting its stability. The implosions were pinhole imaged at magnification $M = 6$ onto an x-ray framing camera and recorded on film with filtration to record soft (~800-eV) x rays. In these images the ablation front is identified with an outer emission limb. To quantify the advance of the turn-on, we have tracked the increase of the core emission as a function of ablation-front position. The relative core emission is calculated from each framed image as $2 / (R_{\text{pk}} / 2)^2 \int r I(r) dr$, where $I(r)$ is the angle averaged signal normalized to the peak at the emission limb and R_{pk} is the peak position of the limb. These results are plotted for the low-, mid-, and high-stability implosions in Figs. 1(a)–1(c), respectively. The solid black circles and blue line correspond to the experimental measurements and fit; the dotted black line is the uniform *ASTER* calculation; and the dashed red line is the *ASTER* model including imprint. The data and simulation are fit using a delayed exponential with constant offset. A slight difference can be present in the offsets, which likely



E29101JR

Figure 1

Central emission versus inferred ablation front radius for (a) low-, (b) mid-, and (c) high-stability implosions. Data are indicated by solid circles with blue line showing fit. Results from uniform *ASTER* are indicated by dotted black line for all three cases. High-resolution *ASTER* with laser imprinting is shown by dashed red line (low- and mid-stability cases only).

arises from inaccuracies in modeling the coronal plasma. To emphasize the emission turn-on, the fit offsets are subtracted and all curves are identically offset by the value obtained from the fit of the uniform model. The emission turn-on is then defined to occur at the normalized emission of unity. We find for the low-adiabat [Fig. 1(a)], this turn-on occurs at a radius $38.4 \pm 2 \mu\text{m}$ larger than what is determined by the identical analysis of the uniform *ASTER* calculation but is only slightly underpredicted with the *ASTER* model including imprint. From the *ASTER* model we find that the early onset of the emission is the result of mass jetting into the hot spot as a result of the instability growth. Figure 1(b) shows that a substantial discrepancy of $22.7 \mu\text{m}$ with the uniform calculation is present for the mid-adiabat, but that in this case the imprint results in no significant modification of the model. As shown in Fig. 1(c), the discrepancy with the uniform calculation is smallest for the most-stable implosion (such stable implosions show no impact from imprinting in calculations and therefore the 3-D high-resolution calculation was not conducted for this specific case). Several additional implosions were examined and supported the presence of a trend of reduced discrepancy in the emission onset with increased stability. In addition we also observed that for the most-stable implosion, the spatial profile of the emission for that implosion exhibited a flat (top-hat) profile of the core emission. Such a profile is observed in a 1-D calculation. The closer agreement of these characteristics for the 1-D prediction for the highly stabilized implosion suggests a role of unmodeled hydrodynamic perturbations in the cryogenic experiments.

In summary, time- and space-resolved characterization of the onset of core x-ray emission were used to diagnose conditions at the start of deceleration. With respect to understanding current limitations on hot-spot performance, the x-ray emission onset provides first evidence of good agreement with a 3-D radiation-hydrodynamic model of laser imprint in a low-adiabat, integrated DT cryogenic implosion. However, these measurements also suggest that additional perturbations beyond imprint remain to be identified and mitigated in the scaled direct-drive DT cryogenic implosions.

This material is based upon work supported by the Department of Energy National Nuclear Security Administration under Award Number DE-NA0003856, the University of Rochester, and the New York State Energy Research and Development Authority.

1. V. Gopalaswamy *et al.*, *Nature* **565**, 581 (2019).
2. R. Betti *et al.*, *Phys. Rev. Lett.* **114**, 255003 (2015).

3. V. N. Goncharov *et al.*, Phys. Plasmas **21**, 056315 (2014).
4. S. Atzeni and J. Meyer-ter-Vehn, *The Physics of Inertial Fusion: Beam Plasma Interaction, Hydrodynamics, Hot Dense Matter*, 1st ed., International Series of Monographs on Physics, Vol. 125 (Oxford University Press, Oxford, 2004).
5. P. B. Radha *et al.*, Phys. Plasmas **12**, 032702 (2005).
6. V. A. Smalyuk *et al.*, Phys. Rev. Lett. **103**, 105001 (2009).
7. S. X. Hu *et al.*, Phys. Rev. Lett. **108**, 195003 (2012).
8. D. T. Michel *et al.*, High Power Laser Sci. Eng. **3**, e19 (2015).
9. I. V. Igumenshchev *et al.*, Phys. Plasmas **23**, 052702 (2016).

First Temperature and Velocity Measurements of the Dense Fuel Layer in Inertial Confinement Fusion Experiments

O. M. Mannion,¹ A. J. Crilly,² C. J. Forrest,¹ B. D. Appelbe,² Z. L. Mohamed,¹ V. Yu. Glebov,¹ V. Gopalaswamy,¹ V. N. Goncharov,¹ J. P. Knauer,¹ T. C. Sangster,¹ C. Stoeckl,¹ J. P. Chittenden,² and S. P. Regan¹

¹Laboratory for Laser Energetics, University of Rochester

²Centre for Inertial Fusion Studies, The Blackett Laboratory, Imperial College, London

The hydrodynamic properties of the shell in cryogenic inertial confinement fusion (ICF) experiments are of vital importance but have yet to be measured experimentally. Recent theoretical work¹ has demonstrated how the spectral shape of the kinematic edges in the neutron energy spectrum emitted from an ICF target could be used to infer the hydrodynamic properties of the dense DT fuel layer. When an incident neutron of energy $E_{n,i}$ elastically scatters off a stationary ion, the neutron will exit the scattering event at an energy $E_{n,f} = E_{n,i} \left[\frac{A^2 + 1 + 2A \cos(\theta_{cm})}{(A + 1)^2} \right]$, where A is the ion-to-neutron mass ratio and θ_{cm} is the neutron scattering angle in the center-of-mass frame. The minimum energy at which a neutron can exit an elastic-scattering event is called the kinematic limit and occurs when the neutron undergoes a backscatter event ($\theta_{cm} = \pi$), resulting in an outgoing neutron at energy $E_{bs} = E_{n,i} (A - 1) / (A + 1)$. Since no neutron can reach energies lower than E_{bs} through a single elastic-scattering event, the neutron energy spectrum will have a sharp edge feature located at E_{bs} . This feature is referred to as the kinematic (or backscatter) edge.

The kinematic limit is shifted if the scattering ion is moving (see Fig. 1). The magnitude of this shift is dependent on the relative velocity between the ion and neutron.¹ When neutrons scatter off a population of ions with a given ion-velocity distribution, the resulting edge feature is the superposition of the kinematic edge produced from many neutron-ion scattering events. This results in the measured kinematic edge containing information on the ion-velocity distribution. In particular, the mean \bar{v} of the ion-velocity distribution will cause an energy shift in the resulting edge location, while the variance Δ_v^2 of the ion-velocity distri-

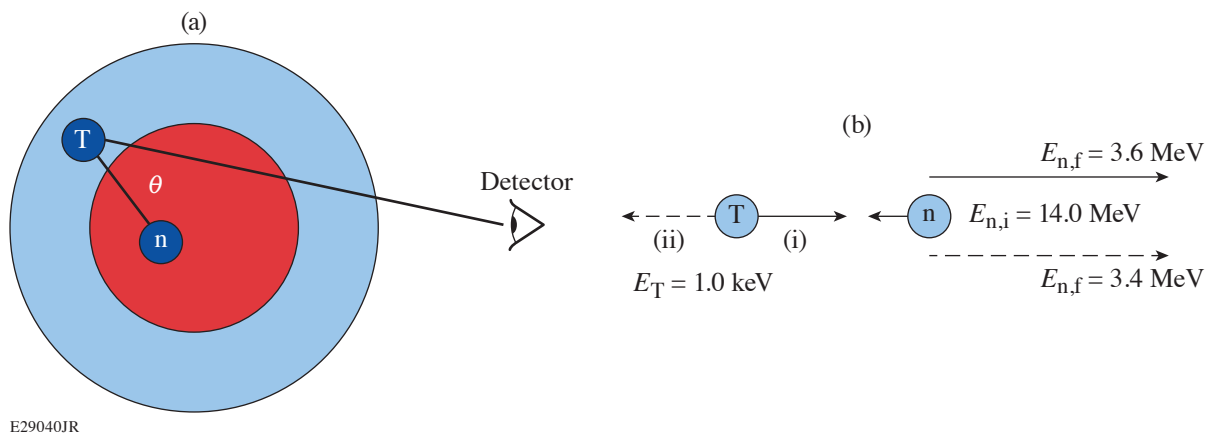
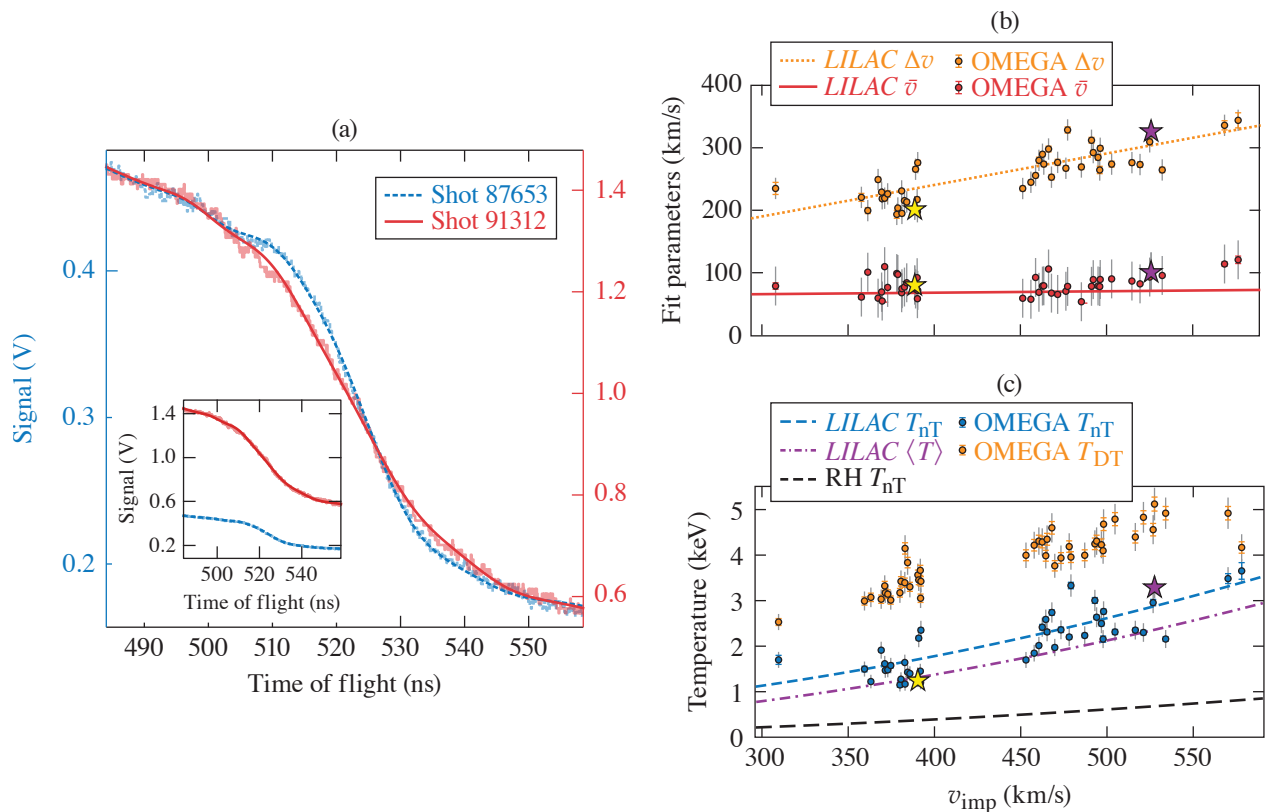


Figure 1
 (a) A schematic of neutron scattering in a compressed ICF target, which consists of a low-density, high-temperature hot spot (red), surrounded by a low-temperature, high-density shell (blue). (b) Backscatter kinematics for a 1-keV triton moving (i) toward and (ii) away from an incident DT neutron.

bution will cause a change in the slope of the edge. Therefore, the spectral shape of the kinematic edge produced when neutrons scatter off a material can be used to diagnose the moments of the ion-velocity distribution within the material.

Neutron scattering occurs throughout the compressed ICF target, which results in the kinematic edges sampling the ion-velocity distributions in many regions of the capsule. The ion-velocity distribution being measured by the kinematic edges from an ICF target is the scatter-weighted, ion-velocity distribution. The shape of this distribution has been studied¹ using the 1-D radiation-hydrodynamic code *LILAC* and found to be well described by a normal distribution with a mean \bar{v} and variance Δv^2 . The mean \bar{v} is the scatter-weighted velocity of the shell, while the variance Δv^2 is related to the scatter-weighted temperature and velocity variance of the shell.

The nT kinematic edge has been measured for an ensemble of direct-drive DT cryogenic implosions on OMEGA using a neutron time-of-flight (nTOF) detector, and a forward-fit analysis has been applied to infer the moments of the triton velocity distribution. Example nT-edge measurements along with the forward fit are shown in Fig. 2. To minimize the effect of implosion asymmetries on the nT-edge measurements, only experiments with apparent ion temperature asymmetry <1.0 keV and hot-spot flow velocities <80 km/s were considered.



E29041JR

Figure 2

(a) The measured nTOF signal (shaded) and forward fit (solid and dashed lines) in the nT-edge region for two experiments. The primary DT neutron yields and areal density for these two experiments were different, resulting in the measured nT edges having different amplitudes. The data have been plotted as two separate signal axes to facilitate comparison of the nT spectral shape. The inset shows the nTOF signals plotted on the same signal axis for reference. (b) The measured (circles) and *LILAC* calculated (lines) values for Δv and \bar{v} as functions of calculated implosion velocity. (c) The measured nT edge (blue circles) and primary DT (orange circles) temperatures as functions of implosion velocity. Also shown are the *LILAC*-inferred temperature from the nT edge (blue dashed line), the *LILAC* scatter-averaged triton temperature (purple dashed–dotted line), and the temperature of the shocked material as calculated by strong shock Rankine–Hugoniot (RH) conditions (black dashed line). The statistical uncertainties are shown as error bars on the points and the systematic uncertainties are shown as gray bars on the points. The results for the experiments in (a) are indicated as stars for shots 87653 (yellow) and 91312 (purple).

The inferred \bar{v} and Δ_v^2 values from the ensemble of experiments are shown in Fig. 2 as a function of the implosion velocity v_{imp} as calculated by *LILAC*. Calculations of Δ_v^2 and \bar{v} from post-shot *LILAC* simulations are in good agreement with the measured values. The inferred shell velocities \bar{v} are uniform across the experiments on OMEGA with an average velocity of 79 km/s and standard deviation of 16 km/s. The measured velocities are small in comparison to the implosion velocity due to the measurement sampling the shell velocity near peak compression [see Fig. 2(b)]. The \bar{v} measurements indicate there is little variability in the shell residual kinetic energy for these implosions, which is expected since these implosions were chosen for their symmetry.

The nT- and DT-inferred temperatures are shown in Fig. 2(c) as functions of implosion velocity. The nT measured temperatures are lower than the DT temperatures. This is a result of the DT-inferred temperature being a neutron-averaged quantity, which results in the inferred value being weighted toward the region in which fusion reactions are occurring (i.e., the hot spot), whereas the nT-inferred temperature is a scatter-averaged quantity, which results in the inferred value being weighted toward the denser and colder regions (i.e., the shell). The increase in the nT-edge temperature with implosion velocity is due to an increase of the thermal conduction from the hot spot into the shell. The thermal conduction of a fully ionized ideal gas² has a temperature dependence of $T^{5/2}$. The higher initial hot-spot temperatures achieved with higher implosion velocities [see Fig. 2(b)] result in an increased thermal conduction of heat from the hot spot into the shell. This increases the temperature of the shell while also increasing the ablation rate of cold material into the hot spot. Consequently, the fraction of neutron scattering in shocked material >1 keV increases linearly with implosion velocity while the contribution from material <1 keV decreases. Since the nT edge temperature is scatter weighted, the increasing contribution from material >1 keV is the dominant contribution to the increased nT inferred temperature.

The temperature and velocity measurements presented here, along with areal-density measurements of the shell, now provide a complete set of hydrodynamic properties of the dense fuel layer near peak compression. The temperature measurements provide a key piece of information required to measure the shell adiabat in cryogenic ICF experiment. The shell-velocity measurements provide the first experimental evidence of residual motion of the shell near peak compression and provide the first insights into the conversion efficiency of shell kinetic energy to thermal energy of the hot spot. Future work will extend this analysis to multiple lines of sight and investigate asymmetric implosions. Additionally, this technique can be applied to other backscatter edges that occur in ICF experiments such as the deuterium backscatter edge at 1.5 MeV in DT cryogenic implosions or the beryllium edge that exists in magnetized liner fusion experiments. Finally, this technique can be applied to a more general set of high-energy-density experiments that require measurements of the hydrodynamic properties of dense shocked materials.

This material is based upon work supported by the Department of Energy National Nuclear Security Administration under Award Number DE-NA0003856, the University of Rochester, and the New York State Energy Research and Development Authority.

1. A. J. Crilly *et al.*, *Phys. Plasmas* **27**, 012701 (2020).
2. L. Spitzer, *Physics of Fully Ionized Gases*, 2nd rev. ed., Interscience Tracts on Physics and Astronomy (Wiley Interscience, New York, 1962).

Self-Radiography of Imploded Shells on OMEGA Based on Additive-Free Multi-Monochromatic Continuum Spectral Analysis

R. Epstein,¹ R. C. Mancini,² D. T. Cliche,² R. C. Shah,¹ T. J. B. Collins,¹ C. Stoeckl,¹ P. W. McKenty,¹ P. B. Radha,¹
S. P. Regan,¹ and V. N. Goncharov¹

¹Laboratory for Laser Energetics, University of Rochester

²University of Nevada, Reno

Cryogenic implosions on the OMEGA Laser System¹ can be self-radiographed by their own core spectral emission near ≈ 2 keV. Utilizing the distinct spectral dependences of continuum emissivity and opacity, the projected optical thickness distribution of imploded shells can be distinguished from the structure of the core emission in images. This can be done without relying on spectral additives (shell dopants), as in previous applications of implosion self-radiography.² Demonstrations with simulated data show that this technique is remarkably well-suited to cryogenic implosions. Imploded room-temperature CH shells can also be self-radiographed at higher spectral energy ($h\nu \approx 3$ to 5 keV) based on the very similar continuum spectrum of carbon. Experimental demonstration of additive-free self-radiography with warm CH shell implosions on OMEGA will provide an important proof of principle for future applications to cryogenic DT implosions.

Externally backlit radiography³ is primarily sensitive to the shape of the limb of the shell as projected onto an image plane and requires spectral filtering and/or temporal gating techniques⁴ to keep the core from outshining the external backlighter as the implosion approaches peak conditions. Self-radiography sidesteps this limitation by using core self-emission as the backlighter to project the structure of the near face of the shell onto an image plane.

We formulate continuum radiography as a spectral analysis of the imaged intensity at each image pixel, based on the free-free and bound-free emissivity and opacity of hydrogen-like ions as described by the Kramer's⁵ semi-classical expressions with power-law Gaunt factor corrections^{6,7} based on Karzas and Latter,⁸ of the form $g_\nu \propto (\nu/\nu_0)^{-q}$. For the anticipated spectral range for CH shell implosions, $3.6 < h\nu_0 < 5.4$ keV, the likely index value at the spectral midpoint is $q \approx 0.11$. The index rises slowly to $q \approx 0.5$ in the limit that the spectral energy greatly exceeds the electron binding energy, which applies to hydrogen.

The shell optical thickness at a nominal spectral frequency ν_0 can be expressed in terms of the power law $\tau_\nu \propto (\nu/\nu_0)^{-(3+q)}$. In local thermodynamic equilibrium, the emissivity spectral form is obtained from the opacity by the Kirchhoff relationship⁹ using the Planck function. The result is a phenomenological expression of the intensity spectrum for a thermal continuum emitter surrounded by a non-emitting layer

$$I_\nu = A(\nu_0/\nu)^q e^{-(1-\nu/\nu_0)/t - \tau_0(\nu_0/\nu)^{3+q}}, \quad (1)$$

where A represents the unabsorbed emission, τ_0 is the optical thickness of the foreground absorber, and $t = kT/h\nu_0$ is a local continuum slope parameter that can be interpreted as an emission-weighted, harmonic mean of the source electron temperature. These three parameters are estimated at each pixel.

The three spectral parameter estimates will be sensitive to signal noise. With three images covering a bandwidth $\Delta\nu$ and with pixel intensities precise to a standard deviation equal to a fraction σ_I , the resulting formal uncertainty of the τ estimates, for example, in the small- $\Delta\nu$ limit is $\delta\tau \cong \sqrt{2/3} \sigma_I (\nu_0/\Delta\nu)^2$. It is clear from the strong $\Delta\nu$ scaling of this expression that broad bandwidth is essential.

We apply our proposed analysis to synthetic data based on radiation-hydrodynamic simulations to show that the emission and absorption separation expressed in Eq. (1) is valid and that radiographs can be successfully inferred. The example selected here is based on a 2-D *DRACO*¹⁰ simulation of the implosion experiment shot 81590 (Ref. 4). Figure 1 shows three simulated images at spectral energies $h\nu = 1.6, 1.8,$ and 2.0 keV, obtained from this simulation at a time near peak neutron production with the radiation-transport postprocessor *Spect3D*.¹¹ The view direction is 30° above the equatorial plane. The *DRACO* simulation includes the effects of nonuniform laser irradiation, including the ideal single-beam intensity profile, OMEGA's 60-beam pattern, and fine-scale beam speckle. The image structure in any one image is the net result of emission followed by absorption. Separating the absorption structure from the emission structure by spectral analysis is the basis of self-radiography.

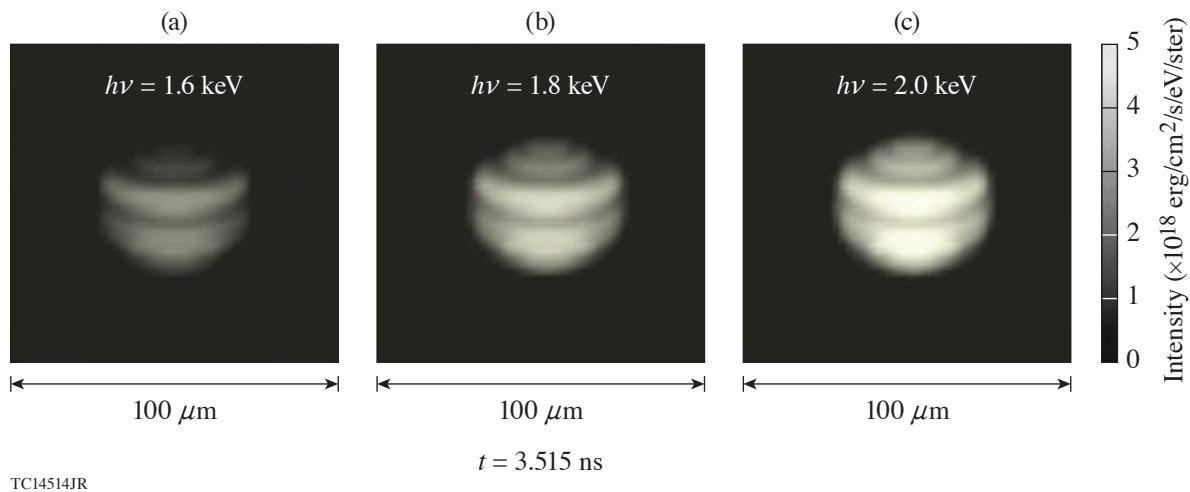


Figure 1

Three simulated monochromatic images of the OMEGA implosion experiment shot 81590 at spectral energies (a) $h\nu = 1.6$, (b) 1.8 , and (c) 2.0 keV at a time near peak neutron production.

Pixel-by-pixel spectral analysis based on Eq. (1) produces the unabsorbed emission distribution shown in Fig. 2(a) and the radiograph in Fig. 2(b), both at $h\nu = 1.8$ keV. The radiograph shows the optical thickness increasing from just below unity at the center to about double that at the edge. This absorption profile changes the roughly uniform appearance of the bare emission distribution in Fig. 2(a) into the centrally bright appearance of the simulated images in Fig. 1.

The radiograph in Fig. 2(b) is most useful within a circular area whose diameter is approximately the length of the red spatial reference arrow. The analysis produces optical thicknesses further out from the center, but this is beyond the outer edge of the emitting core, where the fitting model may be misapplied and where the image signal may be too weak to use, relative to instrumental noise, etc. To show that the radiograph is quantitative where the image signal is reasonably strong, we compare the inferred optical thickness at 20 points on the image plane along the spatial reference arrow with the optical thickness calculated directly from the image simulation model. These are shown as the “inferred” and “actual” points in the plot in Fig. 2(c), respectively. The agreement is very good. The inferred values are all slightly lower than the actual values because a small part of the actual total optical thickness exists in the emitting core where it is only partially effective in attenuating the core emission.

We anticipate a proof-of-principle demonstration of continuum-based self-radiography of OMEGA implosions using imploded CH polymer shells imaged with the multiframe monochromatic imager (MMI) instrument.¹² The MMI combines Bragg reflection with a pinhole array to provide time-gated images of inertial confinement fusion implosions. The quantitative capabilities of the MMI have been most recently characterized quantitatively by Cliche *et al.*¹³ The current configuration operates with a broad 3.5- to 5.5-keV spectral range and independent electro-optic time gating along four strips on a multichannel photoelectron-multiplying detector plate at the image plane. The MMI could be also be used for self-radiography of cryogenic implosions at lower spectral

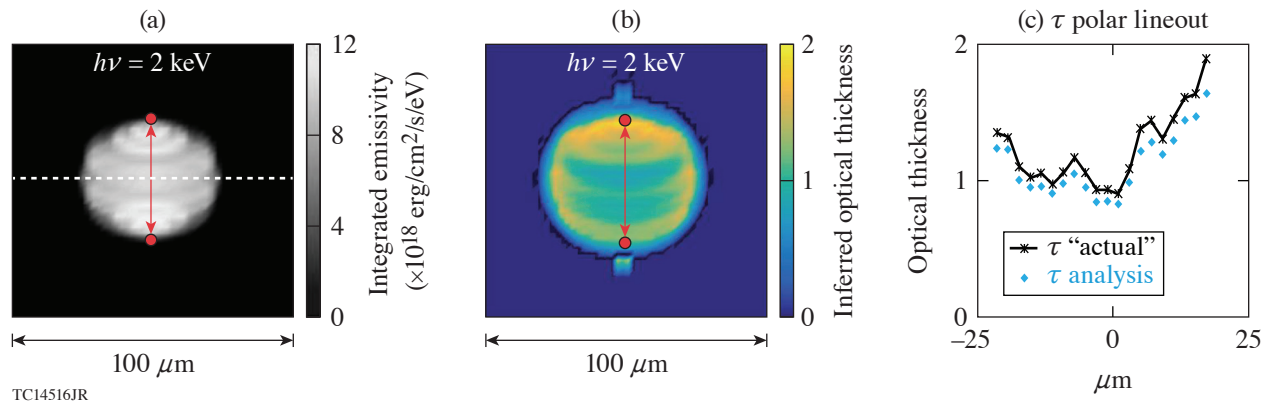


Figure 2

Analysis results showing the (a) unabsorbed emission distribution, (b) inferred radiograph, and (c) a vertical lineout of the radiograph optical thickness showing agreement between inferred and simulated “actual” optical thickness. (a) and (b) represent the spectral energy $h\nu = 1.8 \text{ keV}$.

ranges near $h\nu \approx 2 \text{ keV}$. A theoretical basis for analyzing MMI images of continuum emission in terms of an ideal spherically symmetric source model has already been described.¹⁴ Successful self-radiography of room-temperature CH implosions would be an important and encouraging prelude to continuum-based self-radiography of cryogenic DT shell implosions.

This material is based upon work supported by the Department of Energy National Nuclear Security Administration under Award Number DE-NA0003856, the University of Rochester, and the New York State Energy Research and Development Authority.

1. T. R. Boehly *et al.*, *Opt. Commun.* **133**, 495 (1997).
2. V. A. Smalyuk *et al.*, *Phys. Rev. Lett.* **87**, 155002 (2001); L. A. Pickworth *et al.*, *Phys. Rev. Lett.* **117**, 035001 (2016).
3. R. Epstein *et al.*, *High Energy Density Phys.* **23**, 167 (2017).
4. C. Stoeckl *et al.*, *Phys. Plasmas* **24**, 056304 (2017).
5. H. A. Kramers, *Philos. Mag.* **46**, 836 (1923).
6. J. A. Gaunt, *Proc. R. Soc. Lond. A* **126**, 654 (1930).
7. H. R. Griem, *Principles of Plasma Spectroscopy* (Cambridge University Press, Cambridge, England, 1997).
8. W. J. Karzas and R. Latter, *Astrophys. J. Suppl. Ser.* **6**, 167 (1961).
9. S. Chandrasekhar, *Radiative Transfer* (Dover Publications, New York, 1960).
10. P. B. Radha *et al.*, *Phys. Plasmas* **12**, 032702 (2005); J. A. Marozas *et al.*, *Phys. Plasmas* **25**, 056314 (2018).
11. J. J. MacFarlane *et al.*, *High Energy Density Phys.* **3**, 181 (2007); Prism Computational Sciences Inc., Madison, WI 53711.
12. J. A. Koch *et al.*, *Rev. Sci. Instrum.* **76**, 073708 (2005).
13. D. T. Cliche and R. C. Mancini, *Appl. Opt.* **58**, 4753 (2019).
14. J. A. Koch, S. W. Haan, and R. C. Mancini, *J. Quant. Spectrosc. Radiat. Transf.* **88**, 433 (2004).

Principal Factors in the Performance of Indirect-Drive Laser-Fusion Experiments

C. A. Thomas,¹ K. L. Baker,² D. T. Casey,² M. Hohenberger,² A. L. Kritcher,² B. K. Spears,² S. F. Khan,² R. Nora,² D. T. Woods,² J. L. Milovich,² R. L. Berger,² D. Strozzi,² D. D. Ho,² D. Clark,² B. Bachmann,² L. R. Benedetti,² R. Bionta,² P. M. Celliers,² D. N. Fittinghoff,² G. Grim,² R. Hatarik,² N. Izumi,² G. Kyrala,² T. Ma,² M. Millot,² S. R. Nagel,² P. K. Patel,² C. Yeamans,² A. Nikroo,² M. Tabak,² M. Gatu Johnson,³ P. L. Volegov,⁴ S. M. Finnegan,⁴ and E. M. Campbell¹

¹Laboratory for Laser Energetics, University of Rochester

²Lawrence Livermore National Laboratory

³Massachusetts Institute of Technology

⁴Los Alamos National Laboratory

Experiments at the National Ignition Facility (NIF) are underway to test the physics and engineering limitations of thermonuclear burn at laboratory scales.¹ For an indirect-drive experiment, this begins by heating a high-Z cavity/hohlraum with a shaped laser pulse and ablating a low-Z pusher/capsule at ≈ 300 eV (Refs. 2 and 3). This process generates the pressures (≥ 100 Mbar) needed to implode a thin deuterium–tritium (DT) shell to high velocities (350 to 450 km/s) and make a central hot spot that self-heats. The primary goal of this work is to determine the characteristics of the laser and target that are needed for ignition. As documented elsewhere,^{4–8} several advances have been made, but challenges remain. For example, it is still not possible to reliably relate performance to laser energy or implosion symmetry and account and correct for common variations in either. These sensitivities could suggest that one or more aspects of implosion physics are not understood or reproducible. In addition, it is still uncertain if all data can be taken at face value since multiple measurements of a given quantity can disagree, as shown in Fig. 1. Observations of the hot spot can be related to stagnation properties (and the proximity of ignition), but only if the state of the system is well defined. These issues complicate interpretation and present obstacles to predicting future data. Discrepancies could be due to errors in physics (theory or simulation) or variabilities in the target and facility that do not apply equally to all implosions.

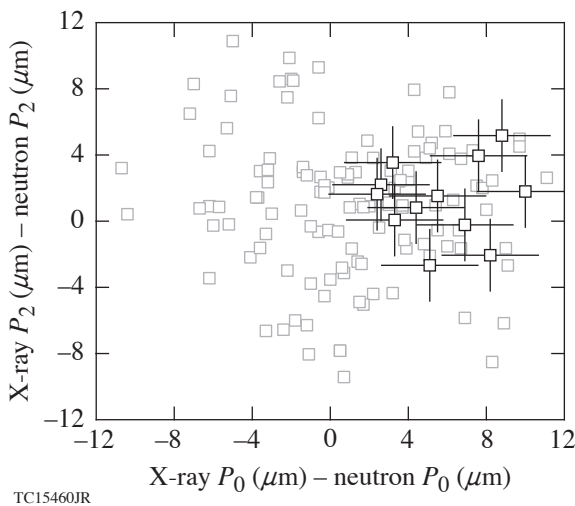


Figure 1

The size and shape of the hot spot (Legendre P_0 and P_2) can differ in independent measurements of x-ray and neutron emission. Inconsistency can be quantified by the scatter in both, as shown here. The inability to correlate hot-spot properties to yield could suggest these data do not resolve or characterize all possible sources of degradation. The expected deviation in the abscissa (ordinate) is 2.5 (2.2) μm , although data on the NIF (open gray squares) vary by 5.2 (4.6) μm . This has not been explained but could indicate small levels of high-Z material (mix) in the hot spot.⁹ Recent data using the BigFoot Platform (open black squares) vary by 2.6 (2.4) μm and have an average abscissa (ordinate) that agrees with simulations.

In this summary, we focus our analyses on experiments using the so-called “BigFoot” platform (see Fig. 2) as described in Ref. 10. These experiments have been designed to reduce complex interactions in the laser, hohlraum, and capsule with the goal of simplifying the integrated system. This required new features in design (discussed below) that do not try to maximize performance. The result has been implosions that are relatively predictable and data that are more self-consistent. Performance compares favorably with theory and, as we show, is a simple function of laser energy per unit target mass (E/M), target scale (S), and low-mode implosion symmetry (hot-spot P_2). Neutron yield Y (measured at 13 to 15 MeV) is found to increase as $(E/M)^{7.6}(S)^4(1 - 0.05|P_2/S|)$ to $\pm 8.7\%$. This analysis suggests that small target flaws and imperfections do not determine the yield, and we can account for small changes in E/M , P_2 , etc. while testing other aspects of inertial confinement fusion (ICF). (Typically, yield can be explained only by detailed calculations in 3-D including flaws unique to each target.^{11,12}) These results provide a useful perspective on data on the NIF and a new baseline for testing the physics of indirect drive.

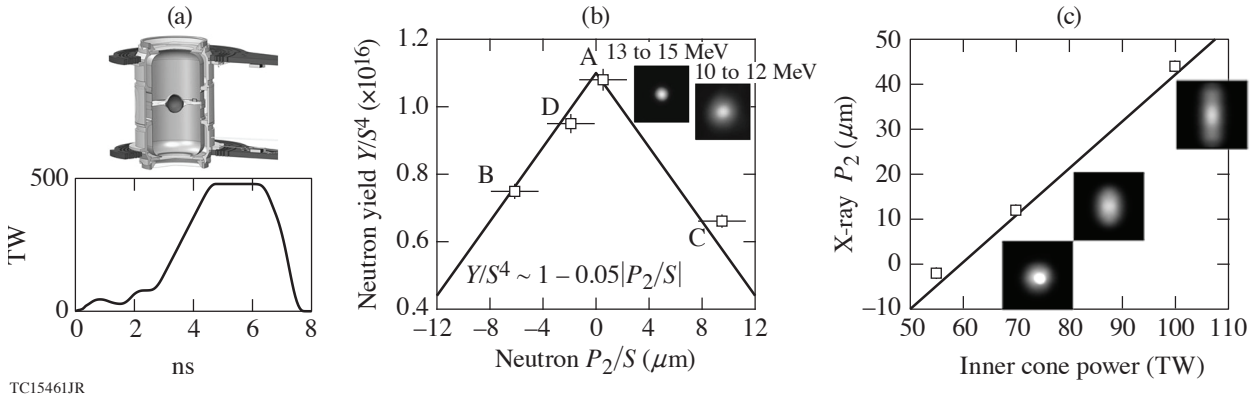


Figure 2

(a) The BigFoot target and laser pulse from shot 180128 at $S = 1.125$. (b) Yield versus hot-spot symmetry for data (open black squares) and simulations (solid line) after normalizing for small differences in target scale. (c) Hot-spot symmetry versus inner cone power at constant total power.

We begin by summarizing the BigFoot design and experimental campaign. The primary features and rationale are as follows: (1) a high-density carbon (HDC) ablator to substantially shorten the laser pulse; (2) a low-gas-fill (LGF) density hohlraum (0.3 mg/cm^3) to reduce laser–plasma instabilities at high power, tamp hohlraum-wall motion, and provide a well-understood radiation source; and (3) a ≥ 12 -Mbar first shock to reduce phase coexistence in the ablator (liquid and solid) and increase hydrodynamic stability. This work also introduced changes in laser pointing, the geometry of the hohlraum, and the pulse shape, which are designed to produce a relatively high-adiabat implosion ($\alpha_v = 4$) as defined in Ref. 10. This shock-timing scheme was characteristic of early experiments in the National Ignition Campaign that gave unexpectedly high yield (e.g., shot 110212) and could reduce perturbations at the fuel–ablator interface. With these choices, the radiation-hydrodynamic code *LASNEX*¹³ is able to predict key aspects of hohlraum performance, such as the time of peak capsule emission ($\pm 100 \text{ ps}$), with the measured laser pulse. This has allowed us to perform symmetric implosions near the power and energy limits of the NIF without employing cross-beam energy transfer.¹⁴ The platform has also allowed us to collect data over a large range in laser energy (0.8 to 1.8 MJ) and primary yield (1.7×10^{14} to 1.7×10^{16}) as needed to study performance.

The first experiments used HDC capsules with an inner radius R of $844 \mu\text{m}$ and a total thickness of $64 \mu\text{m}$ that we define as target scale $S = R/844 = 1$. The equimolar DT layer was $40 \mu\text{m}$ thick to enable high implosion velocities and accurate characterization. The hohlraum was made of Au to avoid concerns with reproducibility (other materials oxidize) and simplify fabrication. The diameter of the hohlraum was $5400 \mu\text{m}$ and its length was $10,130 \mu\text{m}$ [see Fig. 2(a)]. The hohlraum is small so it can reach high radiation temperatures ($\geq 330 \text{ eV}$) without using the maximum energy available on the NIF. This limits the damage to optics and maximizes the potential shot rate. Laser backscatter was limited for all experiments ($\leq 1\%$), and the yield was found to increase monotonically with laser energy E (Ref. 10). Including recent data, the laser energy was increased from 0.8 to 1.3 MJ, and the primary yield from 1.7×10^{14} to 1.0×10^{16} at approximately E^8 . To make a comparison with theory, we assume the mass

forming the hot spot (1) has an initial energy $\sim v^2$ before compression by the cold fuel (it reaches the same implosion velocity as the shell prior to stagnation), (2) is compressed adiabatically with $\gamma = 5/3$ (losses relative to peak compression are small), and (3) achieves a radial compression ratio $\sim (v^2/\alpha_v)^{1/2}$, where the design adiabat α_v is a measure of compressibility.¹⁵ The energy in the hot spot $E_h \sim v^4$ without accounting for alpha heating. If self-heating is included, then we expect $E_h \sim v^{4f}$ with a feedback f greater than 1. If we also assume yield $Y \sim E_h^2$, consistent with $\langle \sigma v \rangle$ at 5 keV (Ref. 16), then we expect $Y \sim v^{8f}$. Scalings of this type are commonly used to explain performance in ICF,² but are difficult to apply to data since the uncertainty in velocity can be 4% to 5%. Alpha heating is not measured and must be inferred. To make more-precise comparisons, this summary uses a surrogate for velocity based on the laser energy E and the initial ablator mass M , which are both known to $<1\%$. If the kinetic energy of the implosion is assumed to scale with E and its mass is proportional to M , then $v^2 \sim E/M$ and $Y \sim (E/M)^{4f}$. Calculations have been used to validate this approach and predict $f \sim 2$ for current experiments. Since implosions could be subject to additional instability or preheat, we will assume $Y \sim (E/M)^N$.

Experiments have also been done with HDC capsules having an inner radius of $950 \mu\text{m}$ at target scale $S = 950/844 = 1.125$. All dimensions of the capsule and hohlraum (and laser pulse) were increased by the same ratio. Peak laser power was increased by S^2 and laser energy by S^3 . The first data of this type (shot number 170524) was compared to experiments at $S = 1$ and the yield was found to increase by a factor of $\approx S^4$ as expected;^{17,18} including prior results, we expect $Y \sim (E/M)^N (S)^4$.

The data can also be used to address low-mode implosion symmetry, i.e., hot-spot P_2 . This is the primary asymmetry on the NIF (laser-irradiation geometry) and two-sided cylindrical hohlraums. Calculations expect the primary loss mechanism to be conduction, and a small P_2 suggests a hot spot with more surface area. This should reduce the time-averaged number density and temperature of the burning plasma. To first order, the change in yield can be captured by an expansion in P_2/P_0 or P_2/S . Small changes in the system can cause asymmetry in P_2 (shot to shot) even for implosions that are designed to be symmetric. In Fig. 2(b) we report the primary neutron yield versus hot-spot P_2 , in microns, for four experiments with the same E/M . The range is $\pm 8 \mu\text{m}$ in P_2 and a factor of 1.6 in yield. The experiments were done in the order shown: A through D. Small changes in the laser, target fabrication, and target alignment could cause this variation. Data and simulation are consistent, and both suggest $Y \sim 1 - 0.05 |P_2/S|$. To show the laser pulse can be adjusted to improve symmetry, we provide Fig. 2(c) in which $\pm 8 \mu\text{m}$ in P_2 is equivalent to $\pm 10\%$ on the inner cone energy (64 beams) or $\mp 5\%$ on the outer cone (128 beams). In net, $Y \sim (E/M)^N (S)^4 (1 - 0.05 |P_2/S|)$.

We determine N with a least squares fit to all data accounting for changes in laser energy, ablator mass, target scale, and implosion symmetry. This analysis can use the x-ray or neutron P^2 since they are well correlated (see Fig. 1), but we choose the latter since neutron data are more directly related to the DT hot spot. In Fig. 3 we assume $Y \sim (E/M)^N (S)^4 (1 - 0.05 |P_2/S|)$ and find $N = 7.6 \pm 0.3$ with a $\chi^2_\nu = 1.2$ normalized per degree of freedom. Given the measurement uncertainty in laser energy is $\pm 0.5\%$ and neutron P_2 is $\pm 1.8 \mu\text{m}$, then we should only fit data to $\approx 8.9\%$. Throughout this summary, we also fit data with subsets of this model and report the residuals. Data are consistent with high levels of alpha heating ($E^{7.6} > E^4$) and require all terms for a good fit. Two experiments are excluded from this process due to known problems with each target: E and F. In one of these experiments the capsule was found to have a defect/hole that would normally disqualify it from use; in the other, the capsule was found to be displaced from target chamber center by $200 \mu\text{m}$ (from one perspective). Most targets are centered to $25 \mu\text{m}$. These issues were identified before each shot and could not be corrected. Both experiments are below trend and demonstrate that our analysis can identify outliers. Anomalies of this type should not be allowed to impact interpretations. All of the other targets met specifications and were not subject to selection effects. These targets used different capsule supports (30- and 45-nm plastic tents) and fill tubes (5- to 10- μm outer radius). Since the data are fit with a simple formula that follows expected sensitivities, it would appear these data can also provide constraints on other factors. Given that sensitivities in laser energy, target scale, and implosion symmetry have now been characterized, this platform can be used to study aspects of implosion physics with high precision. We have started a scan in pulse length that will look at adiabat ($\alpha_v = 2$ to 6) (Ref. 19) and other features in design. These tests will search for unexpected sensitivities and may help explain performance relative to prior data and expectations of ignition.²⁰

To motivate additional work, we briefly discuss the terms in the fit and the physics mechanisms that could play a role. (1) The sensitivity of yield to laser energy reported here is fast relative to prior results⁷ and simple theory with no alpha heating ($\sim E^4$).

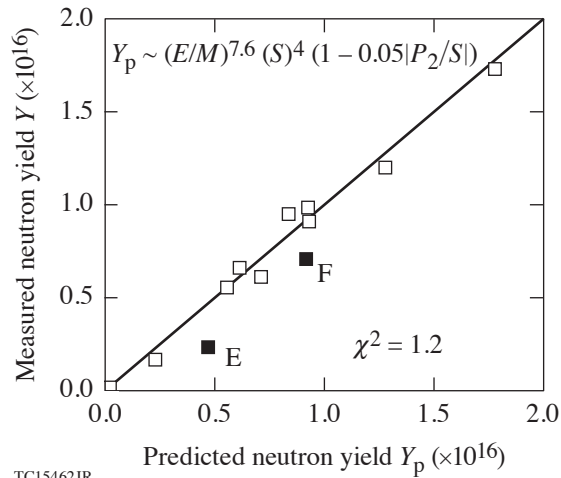


Figure 3
The best fit to data assuming yield is a function of laser energy per unit mass, target scale, and hot-spot symmetry. The residual excluding experiments E and F is 8.7%.

The accuracy of a power law (and its ability to extrapolate) should relate to the range over which it applies. If data are inconsistent with a single value of N or can only be fit over a small range in energy (for a few data points), this could suggest results that are variable (or stochastic). The sensitivity to E/M is a central aspect of performance and the interpretation of other physics. (2) Yield should increase with target scale. BigFoot experiments are intended to be robust and provide the requisite control (shot to shot) to interpret changes in target size. The required level of control is challenging since our analysis shows 6% in E/M can change the yield by a factor of 1.6, similar to a 12% change in S (or $\pm 8 \mu\text{m}$ in P_2). Understanding could be improved by performing experiments with more capsule radii and by making the sensitivity to scale a free variable in the fit to all data. (3) Performance should depend on low-mode symmetry and other observations of the hot spot. This is easy to demonstrate in BigFoot experiments since (a) P_2 is linear in the inner cone power [see Fig. 2(c)] and (b) the impact of target flaws and imperfections are reduced. A small amount of high- Z material can increase x-ray emission (locally), reduce neutron emission, and decorrelate these measurements from each other, and the yield.⁹ Issues of this type would be expected to confuse interpretations of P_0 and P_2 as well as other integrated metrics, such as the burn-averaged pressure. Observations of the hot spot in BigFoot data are self-consistent (as shown in Figs. 1 and 2) and strongly correlate with yield. The uncertainty in subsequent inferences should be reduced. Experiments that make (large) intentional changes in implosion symmetry and stability could be used to extend this work and establish the experimental signature(s) for different failure modes.

Our results can also be used to suggest methods for increasing the yield and alpha heating. As shown in Fig. 4, a straightforward approach would be to increase laser energy by 10% to 20%. If we assume that laser-plasma instabilities do not grow significantly, this will increase the temperature in the hohlraum, the ablation pressure, and the energy coupled to the capsule. Experiments at scale 1 (1.125) have been designed to use 1.5 MJ at 400 TW (2.0 MJ at 500 TW). Using the scalings presented here, this could increase yield by as much as a factor of $(1.5/1.35)^{7.6} = (2.0/1.8)^{7.6} = 2.2$. We have also proposed targets that would use thicker capsules at higher power and energy to further increase E/M (Ref. 10). To determine the expected change in alpha heating, we calculate χ_α (a common metric for ignition¹⁶) and estimate yield amplification as $\exp(\chi_\alpha^{1.2})$. For experiment 180128 (the highest point overall), the measured areal density is $0.620 \pm 0.030 \text{ g/cm}^2$ and primary yield is 1.7×10^{16} . We estimate a total yield of 2.0×10^{16} , $\chi_\alpha = 1.13 \pm 0.06$, and a yield amplification of 3.2 ± 0.2 . Since $\chi_\alpha \sim Y^{0.34}$, a factor of 2.2 in yield would increase χ_α by 30%. This implies that existing targets could demonstrate yield amplifications as high as a factor of $\exp(1.47^{1.2}) = 4.9$. To put this in perspective, the yield amplification in a burning plasma is commonly defined to be 3 to 3.5 (Ref. 16), and for ignition, a factor of 15 to 30. These implosions meet the criteria for an alpha-dominated plasma but are still far from ignition. Nonetheless, we recommend caution with respect to both extrapolations. The measured yield and areal density are consistently below integrated 2-D calculations by a factor of 4 and 1.3, respectively. Also, BigFoot implosions appear to have higher compression ratios than prior data despite having a higher design adiabat ($\alpha_v = 4$). This is inconsistent with theory and may indicate degradation mechanisms that are still unknown²¹ that can be corrected.

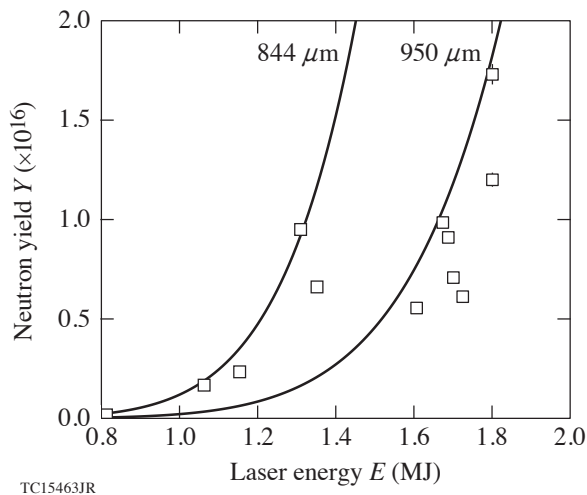


Figure 4

Yield versus laser energy for BigFoot implosions (open black squares) having a capsule inner radius of 844 and 950 μm . For context we show the fit from Fig. 3(a) at each scale [the solid line(s)] in the limit that $P_2 = 0$.

To conclude, we have analyzed implosions that simplify aspects of hohlraum and capsule physics and find that performance can be described by a simple function of laser energy per unit mass (E/M), target scale (S), and implosion symmetry (hot-spot P_2). Neutron yield Y is found to be expressible as $(E/M)^{7.6} (S)^4 \left(\left| 1 - 0.05 P_2/S \right| \right)$ with a residual error that can be accounted for using measurements of E/M and P_2 . This should improve the interpretation of future data and increase confidence in its extrapolation. To build on these results, we have started a scan in design adiabat that will use the same approach and make small changes in the pulse shape (only). We also propose experiments at greater energy per unit mass and will use both studies to address performance limits in indirect drive and criteria for ignition.

This work was made possible by the operations team at the NIF, target fabrication efforts at General Atomics and LLNL, and the encouragement and support of J. H. Nuckolls, J. D. Lindl, W. L. Kruer, and G. B. Zimmerman. We also thank the Senior Leadership Team at the NIF and note that future communications with the first author should be addressed to the Laboratory for Laser Energetics at the University of Rochester. The data that support the findings of this study are available from the corresponding author upon request. This work was performed under the auspices of the U.S. Department of Energy by Lawrence Livermore National Laboratory under Contract DE-AC52-07NA27344, the Department of Energy National Nuclear Security Administration under Award Number DE-NA0003856, the University of Rochester, and the New York State Energy Research and Development Authority.

1. J. Nuckolls *et al.*, *Nature* **239**, 139 (1972).
2. J. D. Lindl, *Inertial Confinement Fusion: The Quest for Ignition and Energy Gain Using Indirect Drive* (Springer-Verlag, New York, 1998).
3. S. Atzeni and J. Meyer-ter-Vehn, *The Physics of Inertial Fusion: Beam Plasma Interaction, Hydrodynamics, Hot Dense Matter, International Series of Monographs on Physics*, Vol. 125 (Oxford University Press, Canada, 2009).
4. O. L. Landen *et al.*, *Plasma Phys. Control. Fusion* **54**, 124026 (2012).
5. M. J. Edwards *et al.*, *Phys. Plasmas* **20**, 070501 (2013).
6. O. A. Hurricane *et al.*, *Nature* **506**, 343 (2014); **510**, 432(E) (2014).
7. D. A. Callahan *et al.*, *Phys. Plasmas* **22**, 056314 (2015).

8. L. F. Berzak Hopkins *et al.*, Phys. Rev. Lett. **114**, 175001 (2015).
9. T. Ma *et al.*, Phys. Plasmas **24**, 056311 (2017).
10. K. L. Baker *et al.*, Phys. Rev. Lett. **121**, 135001 (2018).
11. D. S. Clark *et al.*, Phys. Plasmas **23**, 056302 (2016).
12. C. R. Weber *et al.*, Phys. Plasmas **24**, 056302 (2017).
13. G. B. Zimmerman and W. L. Kruer, Comments Plasma Phys. Control. Fusion **2**, 51 (1975).
14. P. Michel *et al.*, Phys. Plasmas **17**, 056305 (2010).
15. R. Betti *et al.*, Phys. Plasmas **8**, 5257 (2001).
16. R. Betti *et al.*, Phys. Rev. Lett. **114**, 255003 (2015).
17. D. T. Casey *et al.*, Phys. Plasmas **25**, 056308 (2018).
18. R. L. Berger *et al.*, Phys. Plasmas **26**, 012709 (2019).
19. C. A. Thomas *et al.*, "Experiments to Explore the Influence of Pulse Shaping at the National Ignition Facility," to be submitted to Physics of Plasmas.
20. M. C. Herrmann, M. Tabak, and J. D. Lindl, Nucl. Fusion **41**, 99 (2001).
21. B. Cheng *et al.*, Plasma Phys. Control. Fusion **60**, 074011 (2018).

Experiments to Explore the Influence of Pulse Shaping at the National Ignition Facility

C. A. Thomas,¹ K. L. Baker,² D. T. Casey,² M. Hohenberger,² A. L. Kritcher,² B. K. Spears,² S. F. Khan,² R. Nora,² D. T. Woods,² J. L. Milovich,² R. L. Berger,² D. Strozzi,² D. D. Ho,² D. Clark,² B. Bachmann,² L. R. Benedetti,² R. Bionta,² P. M. Celliers,² D. N. Fittinghoff,² G. Grim,² R. Hatarik,² N. Izumi,² G. Kyrala,² T. Ma,² M. Millot,² S. R. Nagel,² C. Yeamans,² A. Nikroo,² M. Tabak,² M. Gatu Johnson,³ P. L. Volegov,⁴ S. M. Finnegan,⁴ and E. M. Campbell¹

¹Laboratory for Laser Energetics, University of Rochester

²Lawrence Livermore National Laboratory

³Massachusetts Institute of Technology

⁴Los Alamos National Laboratory

A primary goal of the National Ignition Facility (NIF) is to determine the laser and target requirements for thermonuclear ignition and propagating burn.¹ From detailed numerical simulations and theory, implosion performance should depend on the shape of the laser pulse and the design adiabat α_v of the DT fusion fuel.^{2,3} By convention, α_v is the pressure in the cold fuel relative to Fermi-degenerate DT at the maximum velocity of the implosion.⁴ In the absence of mechanisms that disturb the fuel, such as preheat, the laser pulse should determine compressibility, and the terms “pulse shaping” and adiabat can be interchangeable. So far, experiments on the NIF have primarily reported tests at $\alpha_v = 1.5$ (Refs. 5 and 6) and $\alpha_v = 2$ to 2.5 (Refs. 7–9) using indirect drive. The integrated performance has improved as issues with hot-spot mix,¹⁰ and target engineering features^{11,12} have been identified and mitigated. Changes in the pulse shape may also have played a role but have not been as easy to study. In part, this is because uncertainties in hohlraum and capsule physics complicate the interpretation of simple tests.¹³ Existing pulse shapes are also calculated to be at (or near) local optima, making it difficult to motivate new concepts.

To provide new insight, this summary takes advantage of the “BigFoot” platform that was developed to facilitate single-variable studies.¹⁴ This design uses conservative features that are to reduce the number of mechanisms that impact data. As shown in prior work,¹⁵ the yield is a simple and expected function of laser energy per unit target mass, size/scale, and implosion symmetry and shows little to no sensitivity to target quality. These properties simplify the interpretation of data and reduce the number of experiments needed to study changes in pulse shape. As a consequence, we have used this platform to do implosions at two different design adiabats ($\alpha_v = 4$ and 3 ± 0.1) for comparison to calculations, finding that yield and areal density can decrease when adiabat is reduced. Our findings suggest that the optimum design adiabat is presently above 3 and one or more aspects of simulation are incomplete. We have not been able to explain these results in high-resolution calculations using known details of the targets or facility. This study also provides the first direct evidence that performance can increase with compression, although it may be necessary to correct physics that are still unknown to make significant progress.

For background, we briefly explain features of the BigFoot design that make it useful for this work [see Fig. 1(a)]. First, the length of the laser pulse is shorter (and the radius of the hohlraum entrance hole is larger) than calculations suggest is needed for a higher-performing implosion. This reduces the energy coupled to the target (and the expected yield) but makes it easier to control implosion symmetry if changes are made to the laser pulse. Second, BigFoot experiments have minimal laser–plasma instabilities and show no evidence of energetic electrons. This remains true even when changes are made in the length, power, or energy of the laser pulse.¹⁶ Third, the first shock in the ablator/DT is also considerably stronger (≥ 12 Mbar) than should be necessary for hydrodynamic stability. This reduces the maximum-possible compression of the DT fuel in calculations, but it also limits instabilities seeded by target flaws and imperfections (e.g., the capsule support and fill tube). Fourth, calculations in

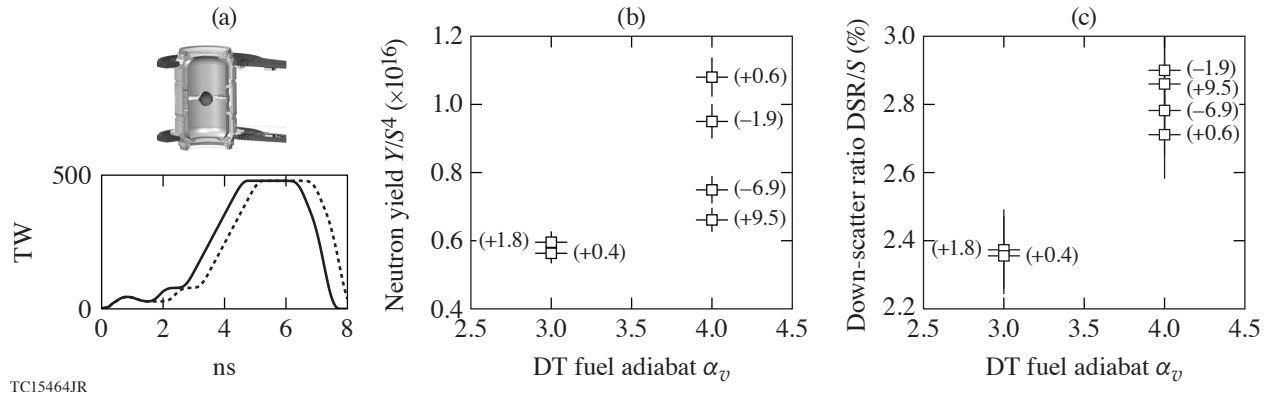


Figure 1

(a) The BigFoot target and laser pulse at $\alpha_v = 4$ (3) are shown by the solid (dashed) line. We also show (b) yield and (c) neutron down-scatter ratio (DSR) normalizing for small changes in target size/scale for six experiments that can be directly compared. The implosion velocity for each is 430 ± 10 km/s. For reference we provide the shape of the hot spot in Legendre P_2 in microns (in parentheses). The yield is correlated to the amplitude of P_2 ; DSR is not.

*LASNEX*¹⁷ are able to predict the time of peak emission (± 100 ps) and implosion symmetry ($\pm 5 \mu\text{m}$ in P_2) using the measured laser pulse.^{18,19} Together, these features make it possible to quickly demonstrate symmetric implosions at different conditions²⁰ with changes to the laser pulse²¹ and to study performance as a function of adiabat.

This summary reports the result of two experiments where the length of the foot (the lower-power section of the laser pulse) is increased by approximately 400 ps, as shown in Fig. 1(a). According to 2-D integrated calculations in *LASNEX*, this should lower the mass-average adiabat of the cold DT fuel from $\alpha_v = 4$ to 3 ± 0.1 , increase the DT density at peak implosion velocity, and increase the final neutron yield and DT areal density by factors of 2.9 and 1.15, respectively. We also increased the laser cone fraction (the power on the inner laser cones of the NIF divided by the total) by 3%. Consistent with calculations and prior experiments, these changes reduce the adiabat of the DT but keep other important variables constant, such as the implosion velocity and symmetry.²¹ (The shocks launched at each rise in the laser pulse are made to overtake closer to the inner radius of DT ice rather than the DT–ablator interface.) In Fig. 1(b), we show the primary neutron yield Y , as measured at 13 to 15 MeV, and in Fig. 1(c), the neutron–down-scatter ratio (DSR) averaged across multiple measurements. The DSR is a function of neutron emission at 10 to 12 MeV and can be related to the burn-averaged DT areal density (in g/cm^2) as $\rho R_b = 20 \text{ DSR}$ (Ref. 6). [The DSR is averaged over all lines of sight since (1) most implosions are close to symmetric (consistent with imaging data), and (2) diagnostics with a similar line of sight can vary by more than the uncertainty in each.] In contrast to calculations, we find the yield and DSR are reduced at a lower adiabat. Figure 2 addresses the statistical significance of these results. Here, we show a fit to prior BigFoot data at $\alpha_v = 4$ that agrees with the measured yield to $\pm 9\%$ (Ref. 15) and predict the new data in the same way. We find the experiments at lower adiabat are below trend by 40% to 50%, or 4 to 5 σ (40% to 9% ≈ 4). It is not possible to explain these results by normal shot-to-shot variations. The yield and DSR at $\alpha_v = 3$ are even below prior data at $\alpha_v = 4$ using smaller capsules at reduced laser energy.

We can illustrate the principles involved with simple models. It is necessary to only assume that the mass forming the hot spot (1) has an initial energy $\sim v^2$ before compression by the cold fuel (it reaches the same implosion velocity as the shell prior to stagnation), (2) is compressed adiabatically with $\gamma = 5/3$ (losses relative to peak compression are small), and (3) achieves a peak radial compression ratio $C_p \sim (v^2/\alpha_v)^{1/2}$ (Ref. 22). If so, the energy in the hot spot $E_h \sim v^2 C_p^2 \sim v^4 \alpha_v^{-1}$. If we also assume that $Y \sim E_h^2$, consistent with $\langle \sigma v \rangle$ at 5 keV (Ref. 23), then $Y \sim v^8 \alpha_v^{-2}$ without accounting for details in hot-spot physics that are uncertain. Since the kinetic energy of the shell is roughly proportional to laser energy E , when the coupling between the hohlraum and capsule is fixed, this is roughly comparable to $Y \sim (E/M)^4 (\alpha_v)^{-2}$, where M is the initial mass of the ablator. This derivation has few assumptions, and it clearly outlines the expected relationship between adiabat, compression, and yield. Since areal density $\sim C_p^2$, it follows that $\text{DSR} \sim (E/M)(\alpha_v)^{-1}$. We can increase the sophistication of these models and derive exponents that are slightly

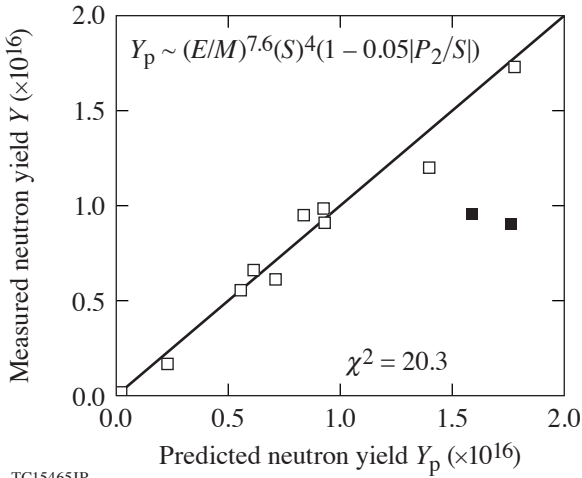


Figure 2
The measured and predicted yield for BigFoot implosions using the analysis in Ref. 15. This model appears to predict data at a design adiabat of 4 (open black squares) but not 3 (solid black squares).

changed (e.g., by including alpha heating, which increases the sensitivity to all terms), but this is not important to interpretation. The yield and DSR should increase together (as shown in Fig. 1) but not by increasing the design adiabat.

To quantify experimental results in the same way, we fit all data to a power law including adiabat and determine the exponents in a least squares sense. For greater accuracy we account for understood changes in laser energy per unit mass (E/M), target size/scale (S), and implosion symmetry (P_2) as in Ref. 15. This exercise is then repeated for DSR with no dependence on P_2 since the data in Fig. 1(c) show no sensitivity. In Fig. 3(a) we assume $Y \sim (E/M)^{N_1}(S)^4(1 - 0.05|P_2/S|)(\alpha_v)^{N_2}$ and find $N_1 = 7.5 \pm 0.3$ and $N_2 = 2.0 \pm 0.1$, for $\chi^2_\nu = 1.2$ (per degree of freedom). In Fig. 3(b) we assume $DSR \sim (E/M)^{N_3}(S)(\alpha_v)^{N_4}$ and find $N_3 = 0.9 \pm 0.2$ and $N_4 = 0.6 \pm 0.1$, for $\chi^2_\nu = 1.1$. These fits are a good representation of data since $\chi^2_\nu \sim 1$, and they behave as expected with the exception of adiabat. In this summary we demonstrate the significance of these findings by fitting the data to subsets of the full model (with no dependence on adiabat) and show that all terms are needed for a good fit. We have proposed to extend this work to a larger range in design adiabat, from 2 to 6. Since these results were unexpected, it is possible that we will find a more-complicated relationship than shown here, with a peak in yield and DSR at a design adiabat other than 4. The value for testing individual aspects of implosion physics is evident, and here, we also discuss the importance of shot-to-shot variability (or reproducibility) to the interpretation of these scalings.

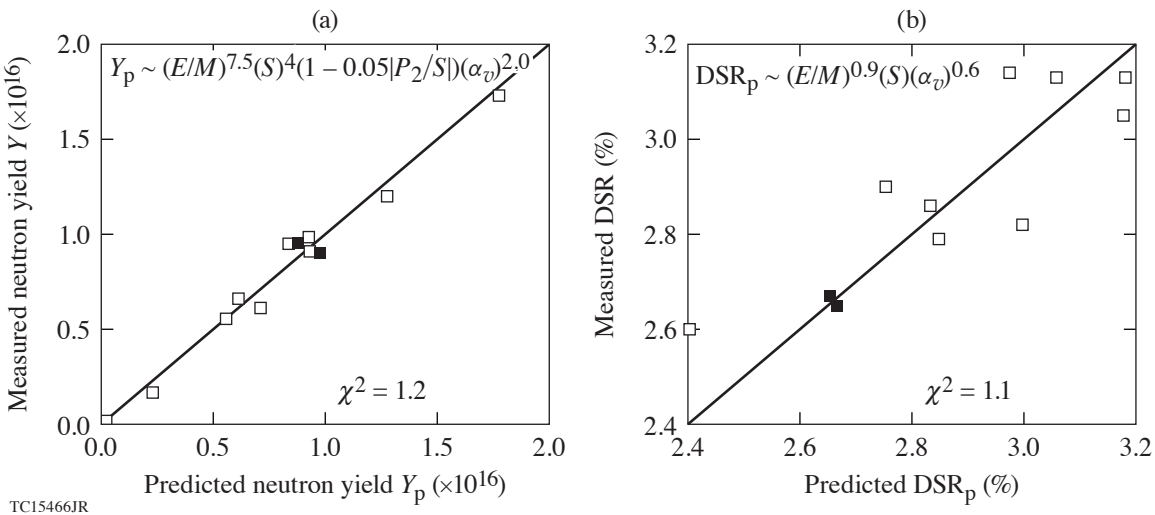


Figure 3
The best model(s) for yield and areal density versus laser energy per unit mass, target scale, hot-spot symmetry, and design adiabat. The residuals are 8.6% and 3.9%, respectively. For reference, we differentiate data at $\alpha_v = 4$ (open black squares) and 3 (solid black squares).

We now examine the peak compression ratio C_p in BigFoot data to check for self-consistency. This quantity is estimated using measurements of the cold fuel since observations of the hot spot (neutron and x-ray imaging) do not have to correlate with $p dV$ work. We begin by defining the areal density at peak compression (without alpha heating) as $\rho R_{p,c} + \rho R_{p,h}$ and at peak burn (with alpha heating) as $\rho R_{b,c} + \rho R_{b,h}$ with contributions from the cold shell and hot spot, respectively. We measure only the latter ρR (typically) but note that alpha heating and electron conduction tend to add energy and mass to the hot spot and reduce the total areal density; as a consequence, $\rho R_{p,c} \geq \rho R_{b,c} + \rho R_{b,h}$. If we then assume that the cold fuel at peak compression has the same mass as the initial DT layer (with areal density $\rho_0 t_0$) and has a relatively thin shell (corrections for a finite hot spot and cold shell are only 1% to 3%), we can put a lower bound on $C_p^2 = (\rho R_{b,c} + \rho R_{b,h}) / \rho_0 t_0 = 20 \text{ DSR} / \rho_0 t_0$. This formula can be used to compare implosions of different sizes and types when alpha heating is modest ($\rho R_{p,h} \ll \rho R_{b,c} + \rho R_{b,h}$) even if hot-spot properties change shot to shot (e.g., due to mix). Figure 4 shows C_p as a function of the mass-averaged first shock velocity in the fusion fuel, u_1 , in km/s. This shock is a reasonable surrogate for the design adiabat as described in Ref. 24. Energy deposition should scale as u_1^2 , and in simulations we find $\alpha_v \approx 1 + 1.4 \times 10^{-3} u_1^2 - 1.4 \times 10^{-7} u_1^4$ for $u_1 \leq 60$ km/s. The goal of pulse shaping is to maximize compression, so we focus on the upper envelope of data. BigFoot implosions with a mass average $\alpha_v = 4$ ($u_1 \approx 55$ km/s) have a compression ratio of 22 to 23. When BigFoot implosions are performed at a lower adiabat ($\alpha_v = 3$ and $u_1 \approx 40$ km/s) with the same implosion velocity and symmetry, they have a compression ratio of 20 and are more consistent with prior results. We find this analysis can also be used to study compression (relative to expectations) independent of calculations. It is only necessary to decide which data can serve as a reference and project $C_p \sim \alpha_v^{1/2}$. If we assume data at a high adiabat are closer to theory, then this type of extrapolation is given by the solid line in Fig. 4. BigFoot data at $\alpha_v = 3$ appear to be deficient in compression and DSR by 25% and 50%, respectively. Offsets at this level are significant since the laser energy needed to ignite $E_{\text{ign}} \sim v^{-6} \alpha_v^2$ (Ref. 25). If $C_p \sim (v^2/\alpha_v)^{1/2}$, this is equivalent to $E_{\text{ign}} \sim v^{-2} C_p^{-4} \sim v^{-2} (20 \text{ DSR} / \rho_0 t_0)^{-2}$. We expect these discrepancies to have an impact on performance and the probability of ignition.

Given these results, we will briefly discuss the mechanisms that could play a role. These could include errors in the strength or timing of shocks.²⁴ We do not suspect issues of this type because (1) these inferences have been validated using VISAR (velocity interferometer system for any reflector)²⁶ and (2) we have not identified a systematic error that would cause a U-shaped sensitivity in u_1 (see Fig. 4). It is also possible that we have made an error in the DT equation of state, the stagnation adiabat, or both. Although not presented here, we find that simulations can match the measured yield, temperature, and DSR of BigFoot implosions if they use a higher adiabat than intended by a factor ≥ 1.4 . For capsules that absorb 200 to 250 kJ of x rays, this is equivalent to adding 80 J to the cold DT shell. Simulations would have to underestimate sources of instability, mix at the fuel–ablator interface, or vorticity at small scales.²⁷ An increase in the effective adiabat could result from residual motion in the cold DT proportional to u_1 , which would increase internal energy as u_1^2 after hydrodynamic growth (compression and thermalization). If the ablator were to mix with the DT fuel, this would also increase its absorption of hard x rays. For insight, we will continue to quantify sensitivities in pulse shaping and work to characterize the state of the DT fuel.²⁸ We also propose to test aspects of stability and,

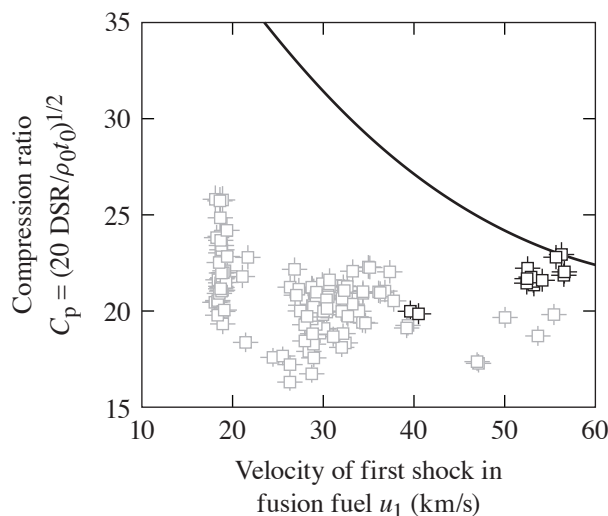


Figure 4

BigFoot data (open black squares) are compared to previous results (open gray squares) on aspects of pulse shaping. Experiments at u_1 of 18, 32, 40, and 55 km/s correspond to α_v of 1.5, 2.3, 3.0, and 4.0, respectively. The solid line is the expected value for a BigFoot-type implosion assuming $C_p \sim \alpha_v^{-1/2}$ at a given velocity and DT mass.

TC15467JR

as a start, have made capsules with different levels of high-Z dopant and crystallinity to address hypotheses regarding preheat and microscopic sources of turbulence.²⁹

In summary, we have used a platform that is well-suited to single-variable studies to test implosions with different pulse shapes and find $Y \sim (E/M)^{7.5} (S)^4 \left(1 - 0.5 \left| P_2/S \right| \right) (\alpha_v)^{2.0}$ and $DSR \sim (E/M)^{0.9} (S) (\alpha_v)^{0.6}$. All terms behave as we expect with the exception of adiabat. These sensitivities will be used to help interpret future work, particularly in circumstances where small or inadvertent changes are made in the laser pulse. If we consider Fig. 4, this could have important implications to compression, and the proximity of ignition. If we only consider the data shown here, a deficit in compression of 25% would be expected to increase the energy needed to ignite by a factor of $1.25^4 \approx 2.4$ relative to expectations.

This work was made possible by the Operations Team at the NIF, target fabrication efforts at General Atomics and LLNL, and the encouragement and support of J. H. Nuckolls, J. D. Lindl, W. L. Kruer, and G. B. Zimmerman. We also thank the Senior Leadership Team at the NIF and note that future communications with the first author should be addressed to the Laboratory for Laser Energetics at the University of Rochester. The data that support the findings of this study are available from the corresponding author upon request. This work was performed under the auspices of the U.S. Department of Energy by Lawrence Livermore National Laboratory under Contract DE-AC52-07NA27344, the Department of Energy National Nuclear Security Administration under Award Number DE-NA0003856, the University of Rochester, and the New York State Energy Research and Development Authority.

1. J. Nuckolls *et al.*, *Nature* **239**, 139 (1972).
2. J. D. Lindl, *Inertial Confinement Fusion: The Quest for Ignition and Energy Gain Using Indirect Drive* (Springer-Verlag, New York, 1998).
3. S. Atzeni and J. Meyer-ter-Vehn, *The Physics of Inertial Fusion: Beam Plasma Interaction, Hydrodynamics, Hot Dense Matter*, 1st ed., International Series of Monographs on Physics, Vol. 125 (Oxford University Press, Oxford, 2004).
4. J. Meyer-ter-Vehn, *Nucl. Fusion* **22**, 561 (1982).
5. O. L. Landen *et al.*, *Plasma Phys. Control. Fusion* **54**, 124026 (2012).
6. M. J. Edwards *et al.*, *Phys. Plasmas* **20**, 070501 (2013).
7. O. A. Hurricane *et al.*, *Nature* **506**, 343 (2014).
8. D. A. Callahan *et al.*, *Phys. Plasmas* **22**, 056314 (2015).
9. L. F. Berzak Hopkins *et al.*, *Phys. Rev. Lett.* **114**, 175001 (2015).
10. T. Ma *et al.*, *Phys. Plasmas* **24**, 056311 (2017).
11. D. S. Clark *et al.*, *Phys. Plasmas* **23**, 056302 (2016).
12. C. R. Weber *et al.*, *Phys. Plasmas* **24**, 056302 (2017).
13. O. L. Landen *et al.*, *High Energy Density Phys.* **36**, 100755 (2020).
14. K. L. Baker *et al.*, *Phys. Rev. Lett.* **121**, 135001 (2018).
15. C. A. Thomas *et al.*, "Principal Factors to Performance in Indirect-Drive Laser Fusion," to be submitted to *Physics of Plasmas*.
16. R. L. Berger *et al.*, *Phys. Plasmas* **26**, 012709 (2019).

17. G. B. Zimmerman and W. L. Kruer, *Comments Plasma Phys. Control. Fusion* **2**, 51 (1975).
18. O. S. Jones *et al.*, *J. Phys.: Conf. Ser.* **717**, 012026 (2016).
19. O. S. Jones *et al.*, *Phys. Plasmas* **24**, 056312 (2017).
20. D. T. Casey *et al.*, *Phys. Plasmas* **25**, 056308 (2018).
21. M. Hohenberger *et al.*, *Phys. Plasmas* **26**, 112707 (2019).
22. R. Betti *et al.*, *Phys. Plasmas* **8**, 5257 (2001).
23. R. Betti *et al.*, *Phys. Rev. Lett.* **114**, 255003 (2015).
24. H. F. Robey *et al.*, *Phys. Plasmas* **19**, 042706 (2012).
25. M. C. Herrmann, M. Tabak, and J. D. Lindl, *Nucl. Fusion* **41**, 99 (2001).
26. H. F. Robey *et al.*, *Phys. Plasmas* **21**, 022703 (2014).
27. B. Cheng *et al.*, *Plasma Phys. Control. Fusion* **60**, 074011 (2018).
28. A. L. Kritcher *et al.*, *Phys. Rev. Lett.* **107**, 015002 (2011).
29. D. D. M. Ho *et al.*, *J. Phys.: Conf. Ser.* **717**, 012023 (2016).

Deficiencies in Compression and Yield in X-Ray-Driven Implosions

C. A. Thomas,¹ K. L. Baker,² D. T. Casey,² M. Hohenberger,² A. L. Kritcher,² B. K. Spears,² S. F. Khan,² R. Nora,² T. Woods,² J. L. Milovich,² R. L. Berger,² D. Strozzi,² D. D. Ho,² D. Clark,² B. Bachmann,² R. Benedetti,² R. Bionta,² P. M. Celliers,² D. N. Fittinghoff,² G. Grim,² R. Hatarik,² N. Izumi,² G. Kyrala,² T. Ma,² M. Millot,² S. R. Nagel,² P. K. Patel,² C. Yeamans,² A. Nikroo,² M. Tabak,² M. Gatu Johnson,³ P. L. Volegov,⁴ S. M. Finnegan,⁴ and E. M. Campbell¹

¹Laboratory for Laser Energetics, University of Rochester

²Lawrence Livermore National Laboratory

³Massachusetts Institute of Technology

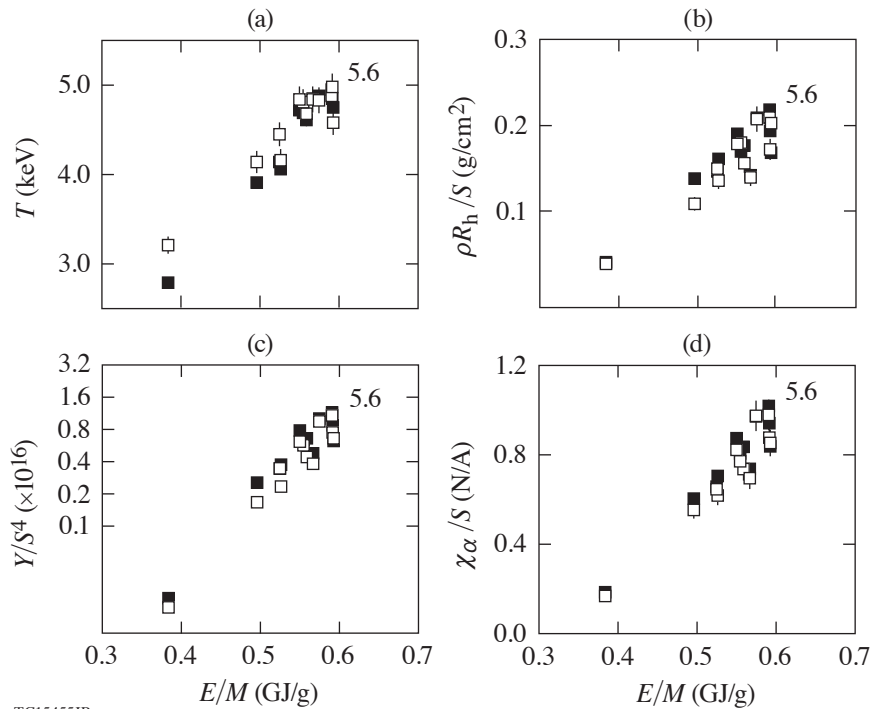
⁴Los Alamos National Laboratory

Implosion performance in inertial confinement fusion (ICF) is generally considered to be a function of hot-spot mix, x-ray symmetry, velocity, and pulse shaping, which is a factor in the adiabat (compressibility) of deuterium–tritium (DT) fusion fuel.^{1,2} We define the design adiabat α_v by the pressure in the fuel relative to Fermi-degenerate DT at the peak velocity of the implosion (as calculated by simulations). To maximize compression it is important to avoid mechanisms that disturb or (pre)heat the fuel and thereby minimize the effective adiabat. Relative to the first experiments at the National Ignition Facility (NIF),^{3,4} improvements in stability have led to increased yield and self-heating as detailed in prior work.^{5–7} Still, it is relatively difficult to explain and project performance since these advances have convolved improvements in target quality, the power and energy delivered by the laser, and a reduction in compression that are not fully understood (individually). Most experiments can be reconciled only with 3-D calculations that include features unique to each target^{8,9} that may not capture (or be aware of) other important aspects in target physics. In addition, it is not easy to control or maintain implosion symmetry, or velocity, at the level necessary to interpret other factors.¹⁰ The primary limitations to temperature, areal density, and self-heating are not yet known, nor are the changes needed to increase fusion yield.

This summary uses results from the so-called “BigFoot” Campaign, which was designed to simplify aspects of hohlraum and capsule physics.¹¹ Calculations were not used to optimize yield but, instead, to select a parameter space that would reduce reliance on 3-D simulations to interpret and extrapolate data. Nonetheless, these implosions have not performed as expected, but in the first half of this summary, we show that measurements are in good agreement with calculations at a higher design adiabat ($\alpha_v = 5.6$) than intended ($\alpha_v = 4.0$). These results are important because they demonstrate a persistent and significant deficit in compression relative to modeling. At the same time these data achieve areal densities (and yields) representing some of the highest-performing experiments on the NIF. To understand the importance of compression more generally, we use the second half of this summary to develop a simple model for interpreting data and find that even small improvements in compression ($\geq 10\%$) could present a pathway to ignition.

Details of the BigFoot target, laser pulse, and strategy can be found in prior work.^{11–13} The platform has been used to test hypotheses in physics since implosions (1) behave as expected with respect to laser energy, target scale, and implosion symmetry, and (2) show little to no sensitivity to target quality and engineering features (within standard specifications).¹⁴ These data are also unusual in that no changes were made in design (shot-to-shot), even though experiments were performed over a large range in laser energy. This makes it possible to study individual data in a manner that is statistically significant, as well as trends. Figures 1 and 2 show the burn-averaged ion temperature T , hot-spot areal density ρR_h , neutron yield Y , and ignition metric χ_α (Ref. 15) versus the laser energy per unit ablator mass (E/M) and neutron down-scatter ratio (DSR) as the open black squares. E/M is a surrogate

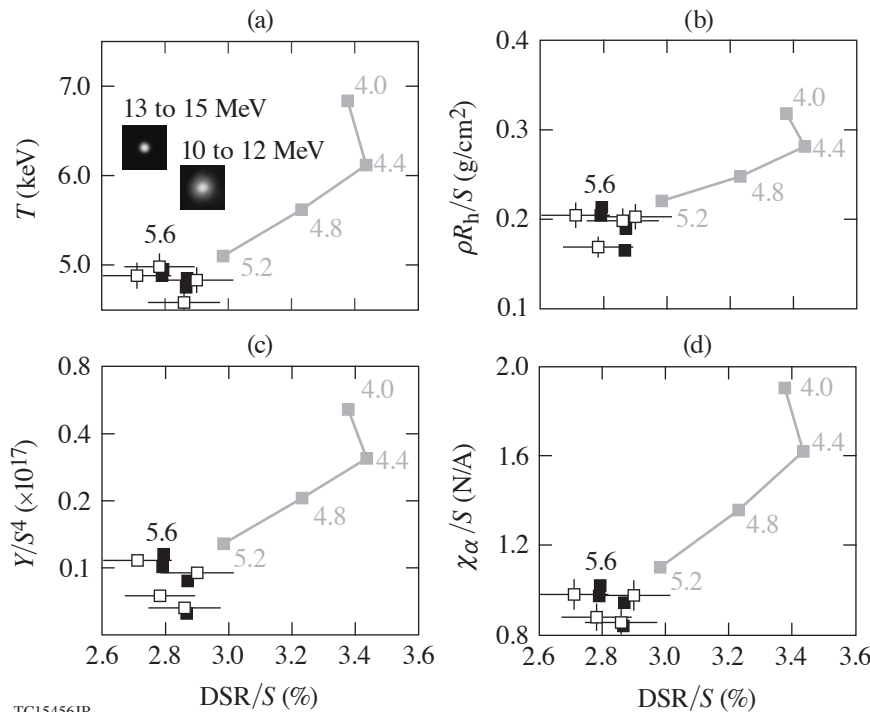
for velocity (and energy density) that is measured on all experiments, and DSR is a common measure of compression proportional to neutron scattering at 10 to 12 MeV. The burn-averaged areal density (in g/cm^2) is given by $\rho R_b = 20 \text{ DSR}$ (Ref. 4). Experiments used a capsule inner radius R of 844 (950) μm , which we define as target scale $S = R/844 = 1$ (1.125). All implosions were designed



TC15455JR

Figure 1

The (a) burn-averaged ion temperature, (b) hot-spot areal density, (c) neutron yield, and (d) χ_α for Big-Foot implosions (open black squares) as a function of laser energy per unit ablator mass E/M normalizing for small differences in target size/scale S . Measurements are a close match to calculations in *LASNEX* (solid black squares) having a design adiabat $\alpha_v = 5.6$. The nominal design adiabat is 4.0.



TC15456JR

Figure 2

The four highest-performing BigFoot experiments (open black squares) are compared to calculations in *LASNEX* at a design adiabat of 5.6 (solid black squares) and 5.2 to 4.0 (solid gray squares) on (a) burn-averaged ion temperature, (b) hot-spot areal density, (c) neutron yield, and (d) χ_α as a function of neutron down-scatter ratio (DSR). The discontinuity coincides with common criteria for ignition ($T \sim 5 \text{ keV}$ and $\rho R_b \geq 0.3 \text{ g}/\text{cm}^2$).

to be self-similar except for the change in scale,¹⁶ so we normalize all of these metrics as appropriate. This simplifies visualization but does not adjust interpretation. The burn-averaged ion temperature is derived from time-of-flight measurements and averaged across multiple lines of sight. Most implosions are symmetric, or nearly so [time-integrated neutron emission data are shown inset to Fig. 2(a)], so measurements of yield and DSR are averaged in the same way. No data stand out from the series, even though we have inferred asymmetries in the ion temperature of 200 to 300 eV and residual motion(s) in the hot spot of 40 to 120 km/s. The areal density of the hot spot is inferred from the ion temperature, neutron yield, neutron burnwidth, and time-integrated neutron hot-spot radius (defined by the 17% intensity contour in emission at 13 to 15 MeV) as outlined in Cerjan *et al.*¹⁷ This approach avoids ambiguities with respect to x-ray emission that cause uncertainty in the volume of the hot spot and can lead to unphysical values for the inferred hot-spot density, pressure, etc. χ_α is a simple function of the burn-averaged areal density, yield, and DT mass and can be used to estimate the distance to ignition with the formula in Ref. 15. Consistent with these interpretations, these data include the highest-performing implosions done on the NIF and have a yield amplification from alpha heating that agrees with $\chi_\alpha \approx 1$. (Separate experiments confirm this result and will be published separately.¹⁸) The experiments shown here have used capsules from different batches, thick and thin capsule supports (30- versus 45-nm tents), and capsule fill tubes (10 μm versus 5 μm) as available. Despite these variations, the data are highly monotonic in E/M , which suggests that engineering details do not dominate performance. This summary will consider other factors, including the DT adiabat.

We note that fitting an ensemble of data with few assumptions provides more confidence in any interpretation. It is difficult to make predictions if each implosion has a unique source of degradation, particularly if multiple mechanisms play a role. This is common in ICF because (1) implosions tend to be complicated and (2) high-resolution calculations must make approximations in physics (e.g., in transport) to study the importance of microscopic imperfections. When simulations reach a certain level of complexity, and/or computational expense, they can be validated only by experiments. Since the metrics in Figs. 1 and 2 are very regular, our efforts have focused on finding a methodology that is insensitive to small details. For the experiments reported here, we find the best fit to data is achieved in simulations that increase the DT fuel adiabat by a factor of 1.4 relative to expectations. This “effective adiabat” lets us reduce the compressibility of all simulations in the same way and serves as the functional replacement for a physics mechanisms that may not be known. We are unable to attribute this change to errors in the x-ray drive,¹⁹ instabilities,²⁰ or mix/preheat²¹ as currently understood. This is accomplished by adding 80 J of internal energy to capsules that absorb 200 to 250 kJ of x rays. To make the best comparisons with data, we use integrated calculations in *LASNEX*²² that reproduce the x-ray drive inferred by VISAR data²³ and the times of peak neutron and x-ray emission (± 100 ps) using the measured laser pulse.^{24,25} Calculations of this type also reproduce the measured implosion velocity, the burn-averaged ion temperature, and the neutron yield in experiments that lack a cryogenic DT layer and have fewer sources of uncertainty. We forward-simulate all diagnostics (as discussed above) and interpret them in the same way. Results are also provided in Figs. 1 and 2. Simulations with a design adiabat of 5.6 are given by the solid black squares and provide a good match to data, even though the expected design adiabat is 4.0. To address requirements for ignition (and standard expectations), we also show the result of calculations at $\alpha_v = 5.2$ to 4.0 by the solid gray squares. Simulations predict the burn-averaged ion temperature to exceed 5 keV along with the onset of ignition when the hot spot has sufficient areal density to rapidly self-heat ($\approx 0.3 \text{ g/cm}^2$) (Refs. 1 and 2). The neutron DSR is directly related to the burn-averaged compression of the DT fuel. Per prior work,²⁶ a lower bound for the no-burn compression ratio is $C_p \approx (20 \text{ DSR}/\rho_0 t_0)^{1/2}$, where $\rho_0 t_0$ is the initial areal density of the cryogenic layer. Typical values for ρ_0 and t_0 are 0.25 g/cm^3 and 40 to 75 μm , respectively. BigFoot experiments are consistent with a deficit in DSR of 20% (or a deficit in compression of 10%) and are otherwise predicted to ignite. Once ignition is achieved in simulation, all performance metrics are discontinuous in DSR, so it is no longer an accurate measure of peak compression.

To understand these results, this summary provides simple models for compression as a function of velocity, DT adiabat, and other details of a given implosion. It also develops simple estimates for the areal density, yield, and χ_α as functions of the same. These derivations are not included in this summary to reserve space for data and will be provided upon request. To make comparisons with data, we note that BigFoot (NIF) implosions are meant to have velocities of 430 (380) km/s and have typically been characterized by a DT mass of 140 (200) μg . The design adiabat is not measured, but it is predicted to depend on the velocity of the first shock in the fusion fuel, u_1 , which is measured in km/s (Ref. 19). If we fit published literature,^{3,5,11} then $\alpha_v \approx 1.2 + 1.0 \times 10^{-3} u_1^2$. Figure 3(a) provides C_p as a function of u_1 for BigFoot (NIF) implosions as the solid black (gray) line, whereas data are the open black (gray) squares. BigFoot implosions have relatively high compression ratios ($C_p \approx 22$ to 23) but are

below theory by at least 10%, consistent with the calculations in Fig. 2. The estimated impacts on areal density, yield, and χ_α is given in Figs. 3(b)–3(d) as C_p^2 , C_p^5 , and C_p^3 , respectively. The minimum deficit relative to expectations is -15% , -30% , and -20% , respectively. (The maximum deficit is considerably larger.) If we extrapolate using the upper envelope of all data (which appears to be continuous), it seems that measurements would approach theory at $u_1 \geq 60$ km/s. Many experiments are below the upper envelope of data and could be sensitive to details that are not known, or not included (e.g., reduced implosion velocity). We note that 3-D calculations tend to result in higher DSR since cold fuel can approach the center of the hot spot and increase the mass-average ρR_b . If so, the formula used here could overestimate the compression ratio in experiments that are unstable. If we consider Fig. 2, BigFoot implosions are designed to approach ignition if compression were to agree with theory. According to Ref. 27, the laser energy needed to ignite E_{ign} should scale as $\approx v^{-6} \alpha_v^2$. Since we expect $x \gg 1$ and $C_p^2 \sim v^2 / \alpha_v$, then $E_{\text{ign}} \sim v^{-2} C_p^{-4}$. It is clear that (1) errors in compression are critical to understanding and (2) even small improvements could enable ignition. A 10% deficit in compression (as shown here) is equivalent to 20% in PdV work on the hot spot. If future efforts are not able to find and correct this discrepancy, the data in this paper can also be used to motivate other changes in target physics. High-performing experiments already achieve 5 keV, so it is only necessary to find an increase in energy per unit mass (or target scale) that allow a hot-spot areal density of 0.3 g/cm² or higher. Above this threshold we expect fusion alpha particles to strongly couple to the hot spot and the DT burnup fraction to depend on the total areal density of the fuel (primarily). If we extrapolate linearly using Fig. 1(b), this would require an increase in E/M of 20% (to overcome the deficit in C_p^2) or an increase in S of 30% (equivalent to a factor of 2.2 in additional laser energy or laser-capsule coupling). Both of these changes can be made in design calculations and are the subject of existing proposal(s).^{11,14}

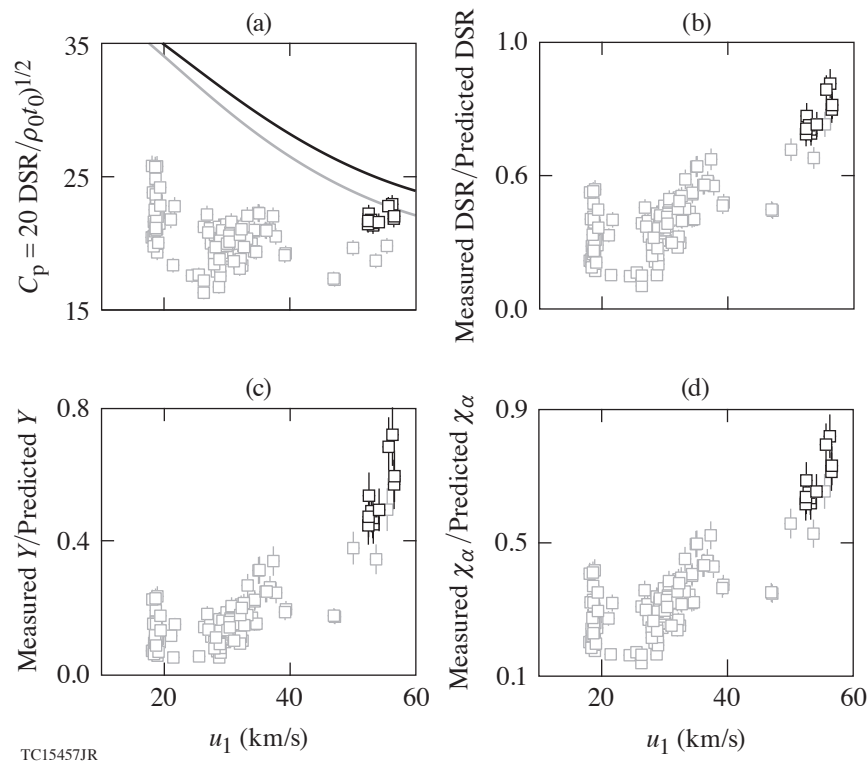


Figure 3

(a) The peak compression ratio C_p as a function of first shock velocity u_1 (a surrogate for adiabat) in BigFoot implosions (open black squares) and prior NIF data (open gray squares). Theoretical expectations are given by the black (gray) line assuming an implosion velocity of 430 (380) km/s and a DT mass of 140 (200) μg . These estimates imply a deficit in (b) DSR, (c) yield, and (d) χ_α that is strongly correlated to adiabat.

In conclusion, we have analyzed x-ray-driven implosions using the BigFoot platform on the NIF and find that performance metrics including ion temperature, hot-spot areal density, and neutron yield are monotonic in laser energy, and calculations are a good match to the data if the adiabat is increased by a factor of 1.4 relative to expectations ($\alpha_v = 5.6$ versus 4.0). Even so, these experiments achieve relatively high compression and yield, and we have developed a simple model to interpret observations. We have proposed implosions at higher laser energy per unit mass, some of which would include larger targets, to provide more insight into potential performance limitations on the NIF. We also plan to test the sensitivities reported here and will make small/iterative changes to the laser pulse in an attempt to improve compression.²⁶

This work was made possible by the operations team at the NIF, target fabrication efforts at General Atomics and LLNL, and the encouragement and support of J. H. Nuckolls, J. D. Lindl, W. L. Kruer, and G. B. Zimmerman. We also thank the Senior Leadership Team at the NIF and note that future communications with the first author should be addressed to the Laboratory for Laser Energetics at the University of Rochester. The data that support the findings of this study are available from the corresponding author upon request. This work was performed under the auspices of the U.S. Department of Energy by Lawrence Livermore National Laboratory under Contract DE-AC52-07NA27344, the Department of Energy National Nuclear Security Administration under Award Number DE-NA0003856, the University of Rochester, and the New York State Energy Research and Development Authority.

1. J. D. Lindl, *Inertial Confinement Fusion: The Quest for Ignition and Energy Gain Using Indirect Drive* (Springer-Verlag, New York, 1998).
2. S. Atzeni and J. Meyer-ter-Vehn, *The Physics of Inertial Fusion: Beam Plasma Interaction, Hydrodynamics, Hot Dense Matter*, 1st ed., International Series of Monographs on Physics, Vol. 125 (Oxford University Press, Oxford, 2004).
3. O. L. Landen *et al.*, *Plasma Phys. Control. Fusion* **54**, 124026 (2012).
4. M. J. Edwards *et al.*, *Phys. Plasmas* **20**, 070501 (2013).
5. O. A. Hurricane *et al.*, *Nature* **506**, 343 (2014).
6. D. A. Callahan *et al.*, *Phys. Plasmas* **22**, 056314 (2015).
7. L. F. Berzak Hopkins *et al.*, *Phys. Rev. Lett.* **114**, 175001 (2015).
8. D. S. Clark *et al.*, *Phys. Plasmas* **23**, 056302 (2016).
9. C. R. Weber *et al.*, *Phys. Plasmas* **24**, 056302 (2017).
10. O. L. Landen *et al.*, *High Energy Density Phys.* **36**, 100755 (2020).
11. K. L. Baker *et al.*, *Phys. Rev. Lett.* **121**, 135001 (2018).
12. R. L. Berger *et al.*, *Phys. Plasmas* **26**, 012709 (2019).
13. M. Hohenberger *et al.*, *Phys. Plasmas* **26**, 112707 (2019).
14. C. A. Thomas *et al.*, “Principal Factors to Performance in Indirect-Drive Laser Fusion,” to be submitted to *Physics of Plasmas*.
15. R. Betti *et al.*, *Phys. Rev. Lett.* **114**, 255003 (2015).
16. D. T. Casey *et al.*, *Phys. Plasmas* **25**, 056308 (2018).
17. C. Cerjan, P. T. Springer, and S. M. Sepke, *Phys. Plasmas* **20**, 056319 (2013).

18. K. L. Baker *et al.*, “Alpha Heating of Indirect-Drive Implosions on the National Ignition Facility,” to be submitted to *Physics of Plasmas*.
19. H. F. Robey *et al.*, *Phys. Plasmas* **19**, 042706 (2012).
20. D. D. M. Ho *et al.*, *J. Phys.: Conf. Ser.* **717**, 012023 (2016).
21. B. Cheng *et al.*, *Plasma Phys. Control. Fusion* **60**, 074011 (2018).
22. G. B. Zimmerman and W. L. Kruer, *Comments Plasma Phys. Control. Fusion* **2**, 51 (1975).
23. H. F. Robey *et al.*, *Phys. Plasmas* **21**, 022703 (2014).
24. O. S. Jones *et al.*, *J. Phys.: Conf. Ser.* **717**, 012026 (2016).
25. O. S. Jones *et al.*, *Phys. Plasmas* **24**, 056312 (2017).
26. C. A. Thomas *et al.*, “Experiments to Explore the Influence of Pulse Shaping at the National Ignition Facility,” to be submitted to *Physics of Plasmas*.
27. M. C. Herrmann, M. Tabak, and J. D. Lindl, *Nucl. Fusion* **41**, 99 (2001).

Azimuthal Uniformity of Cylindrical Implosions on OMEGA

D. H. Barnak,¹ M. J. Bonino,¹ P.-Y. Chang,² J. R. Davies,¹ E. C. Hansen,³ D. R. Harding,¹ J. D. Moody,⁴ J. L. Peebles,¹ B. B. Pollock,⁴ and R. Betti¹

¹Laboratory for Laser Energetics, University of Rochester

²Institute of Space and Plasma Sciences, National Cheng Kung University, Taiwan

³Department of Physics and Astronomy, University of Rochester

⁴Lawrence Livermore National Laboratory

Introduction

Magnetized liner inertial fusion (MagLIF) employs a cylindrical implosion to compress magnetized preheated fuel to fusion-relevant conditions. The MagLIF concept was originally designed around a Z-pinch compression,^{1,2} which is naturally uniform barring instabilities that form at the inner and outer surfaces.^{3–5} To adapt the MagLIF concept to a laser-driven platform, a beam-pointing scheme that achieves a uniform cylindrical implosion must be established. Direct-drive cylindrical implosion platforms have been developed using the OMEGA laser⁶ with the interest of studying Rayleigh–Taylor instability growth^{7,8} and magnetic-flux compression⁹ in cylindrical geometry. Such designs employed in the past have demonstrated axial and azimuthal uniformity with measurements and simulations.¹⁰ Unfortunately, the aspect ratio of the laser-driven MagLIF targets and available distributed phase plates prohibit using these experimental designs.

The axial pointing is empirically derived^{11,12} since many effects, such as cross-beam energy transfer^{13,14} and angle of incidence dependence on laser absorption, complicate finding an analytic solution; an axially uniform illumination does not result in an axially uniform implosion. Calculating azimuthal uniformity has no such complications; an azimuthally uniform illumination gives an azimuthally uniform implosion. Using a finite number of beams will always have some nonuniformity in the illumination of a cylinder, so it is important to quantify how these perturbations affect the drive symmetry. The geometry of the OMEGA laser¹⁵ has four rings of ten beams available to use for a cylindrical implosion, which means at the very least there will be some mode-10 perturbation imposed by the illumination pattern.

Experimental Setup

The standard pointing experiments used parylene-N plastic cylinders that were coated on machined and polished stainless-steel mandrels to 20-, 24-, and 30- μm thicknesses and an 11- to 14-atm fill of D_2 gas. Outer diameters ranged from as low as 550 μm to as high as 610 μm . The shell shape was determined from end-on self-emission x-ray images of the shell in flight. Given the view of the camera and opacity effects from the target, the self-emission images represent the drive uniformity from the ten beams closest to the camera. The laser energy in that group of beams was raised and lowered accordingly to achieve axial uniformity on the cylinder, but the azimuthal uniformity measured by the x-ray images depends only on the distribution and relative intensities of individual beams. The relative imbalance between adjacent beams in the group is no more than 5% rms and does not affect the azimuthal illumination pattern on the cylinder.

The uniform pointing experiments utilized Rexolite tubes with no gas fill, an outer diameter of 640 μm , and 30- μm thickness. Shell shape was determined by x-ray self-emission as before, but in these recent experiments, used the uniform pointing calculated from illuminating the 600- μm -diam hard cylinder. The energy in all of the beams was fixed to ensure axial uniformity, and the imbalance between subsequent beams was, at most, 2% rms. The difference in the imposed perturbation between the 600- μm

and 640- μm cylinders is small enough to be insignificant, but since it is larger, it can infer that smaller-diameter targets will have the same degree of uniformity or better.

The differences between the standard and uniform pointing used and the outer diameters of the target are highlighted by calculating the hard cylinder illumination profile, as shown in Fig. 1. A lineout of each illumination pattern is taken through the beam centers from the ring of beams that drives the end of the cylinder imaged in the radiographs. The lineout is then decomposed into cylindrical modes using Fourier’s trick. The amplitude of the n th mode, A_n , is

$$A_n = \frac{1}{\pi} \int_0^{2\pi} F(\theta) e^{-in\theta} d\theta, \tag{1}$$

where $F(\theta)$ is the lineout in angular space. Note that to have only positive modes, the mode amplitudes must be normalized to $1/\pi$. From this analysis we can compare the mode-5 and mode-10 amplitudes for the standard beam pointing on the nominal 600- μm cylinder, the uniform pointing on the same outer diameter, and the adjusted pointing on the 640- μm cylinder in Fig. 2. All other cylinder mode amplitudes are a fraction of a percent comparatively in these cases.

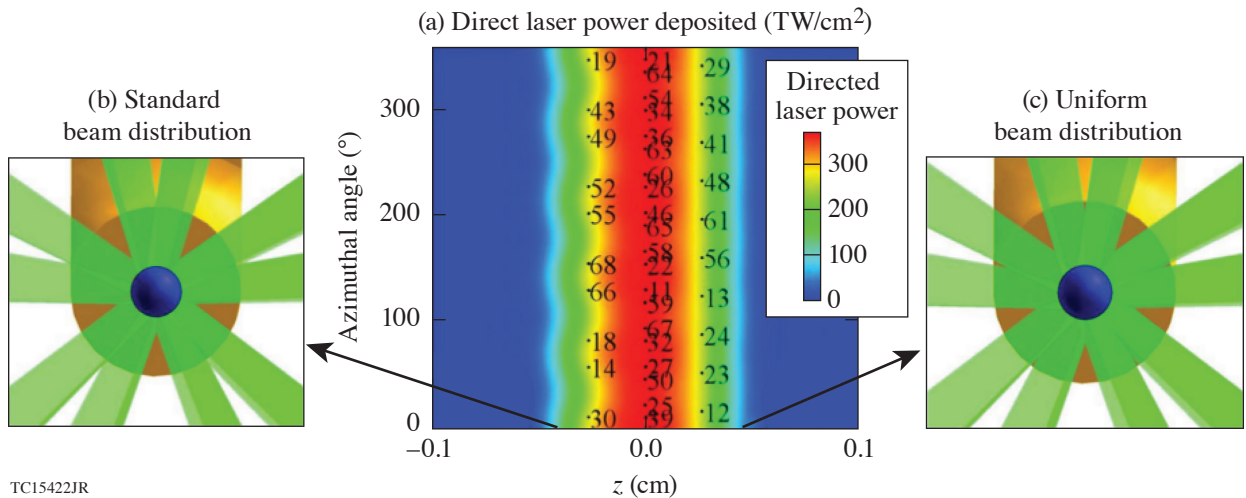


Figure 1 Pointing configuration of the standard and adjusted uniform pointing. (a) The total laser power deposited on the surface of a 600- μm -outer-diam hard cylinder. [(b),(c)] The beams that drive the end of the cylinder closest to the observer, with the cylinder axis coming out of the page. This view of the cylinder is congruent with the view of the framing camera that captured the images of the cylindrical shell in flight. The difference between the two pointings is visually imperceptible; however, this small shift reduces the overall mode-5 perturbation.

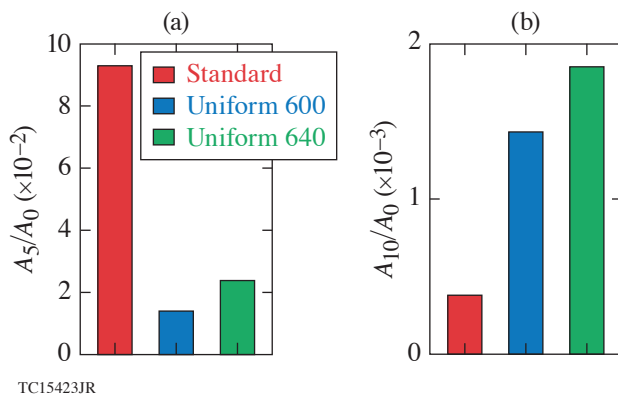


Figure 2 Initial cylindrical mode amplitudes for (a) mode 5 and (b) mode 10 for the standard pointing and the uniform pointing for a 600- μm -outer-diam cylinder and a 640- μm -outer-diam cylinder. The total sum difference between the uniform and standard pointing is a decrease in the mode-5 amplitude by a factor of 6 and an increase in the mode-10 amplitude by a factor of 4. Mode 5 still remains the dominant perturbation.

Standard Pointing Results

Measurements taken with the x-ray framing camera provide time-resolved measurements of the cylindrical mode amplitude growth. Representative images for the three different shell thicknesses used in the standard pointing experiment are shown in Fig. 3. The mode amplitudes are then calculated from the average azimuthal lineout using Fourier's trick, as seen for the irradiation profile in Eq. (1). The modes calculated from the integral are normalized by the mode-0 amplitude, which is

$$A_0 = \int_0^{2\pi} \frac{1}{2\pi} F(\theta) d\theta \quad (2)$$

and is dependent on the camera settings and other hard-to-quantify values such as charge-coupled-device response and gain droop across the strip. Mode 5 is the dominant mode seen growing over time for almost all cases, except for a few cases where there instead appears to be a mode 6. It is difficult to reason why a mode-6 growth would be preferred, given the shape of the initial nonuniformity imposed by the laser, but it is not unreasonable to assume that a target defect or some other feature in the target is responsible.

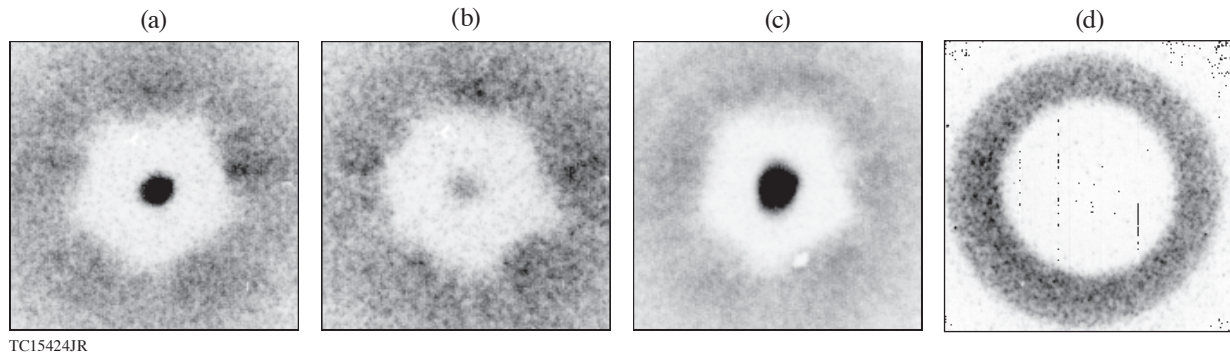


Figure 3

Representative sample images of the cylindrical shell in flight for the standard pointing for (a) 30 μm , (b) 24 μm , and (c) 20 μm . A pentagon structure is visible in all three images. The image sizes are twice the size of the centering circle's diameter, so the image is averaged radially over 70% of the image presented. The 24- μm shell in (b) shows a slight deformation on the left side of the pentagon, which is reflected in the analysis as a growing mode-6 amplitude. (d) A sample x-ray radiograph of a 30- μm -thick, 635- μm -OD cylinder driven by the uniform pointing shows the shell shape staying round to within $\pm 10 \mu\text{m}$.

The briefest and most-complete summary of the results from the standard pointing is that regardless of cylinder diameter and shell thickness, if a mode-5 perturbation of sufficient amplitude is imposed by the laser drive, a mode-5 perturbation will grow. The question of what constitutes a sufficient amplitude will be covered in **Uniform Pointing Results** (p. 127). The amplitude of the perturbation is 6.7% for the smallest outer diameters and 9.3% for the largest outer diameters. The modes grow linearly in time since the acceleration of the ablation surface against the denser shell is stable. The shape of the implosion imposed by the laser likely seeds deceleration-phase Rayleigh–Taylor perturbations after the drive has been turned off. The reduction in mode amplitude from smaller-OD targets does not affect the amplitude growth rate of mode 5 to within the error bars as shown in Fig. 4. Mode-5 growth is also uncorrelated with shell thickness and initial gas pressure.

Three-Dimensional HYDRA Simulations

Simulations using the radiation-hydrodynamic code *HYDRA* were used to produce synthetic radiographs of four configurations: (1) a 30- μm -thick, 600- μm -OD shell driven with a 2.0-ns-long pulse using the standard beam pointing; (2) a 20- μm -thick, 580- μm -OD shell with the same laser drive as case 1; (3) a 30- μm -thick, 640- μm -OD shell driven by a 1.5-ns-long pulse using the uniform pointing; and (4) a 20- μm -thick, 580- μm -OD shell with the same laser drive as case 3.

Self-emission x-ray images from the end of the cylinder are generated in a post-processing routine using the Yorick interpreted language.¹⁶ The simulated radiographs for both pointing cases for 30- μm and 20- μm shells are shown in Fig. 5. Each image is calculated from opacity and emissivity tables along the cylindrical axis line of sight using 0.01- to 10-keV x rays and including the transmission of a 25.4- μm -thick Be filter to match the filters used in the experiment. The image has a field of view of $600 \times$

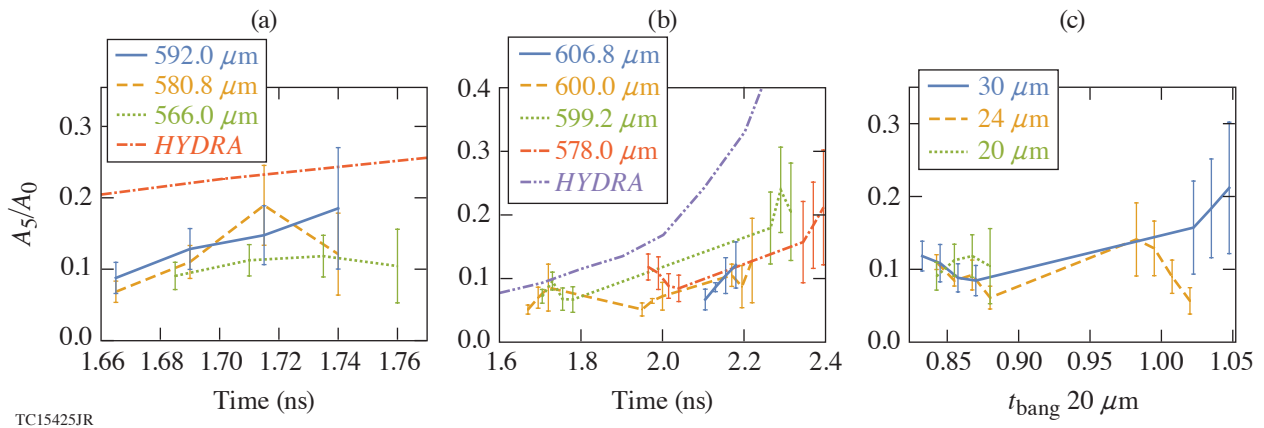


Figure 4

Plots of mode-5 growth for (a) 20- μm and (b) 30- μm -thick cylinders. Between the two thicknesses, different outer diameters do not have a statistically relevant trend of having higher or lower mode-5 perturbation growth over time. *HYDRA* simulations predict a faster mode growth and larger mode amplitude close to the peak x-ray emission of the core. (c) Plots for mode-5 amplitude plotted as a function of time normalized to the x-ray bang time of the 20- μm -thick shells demonstrate that the mode-5 amplitude does not depend on shell thickness.

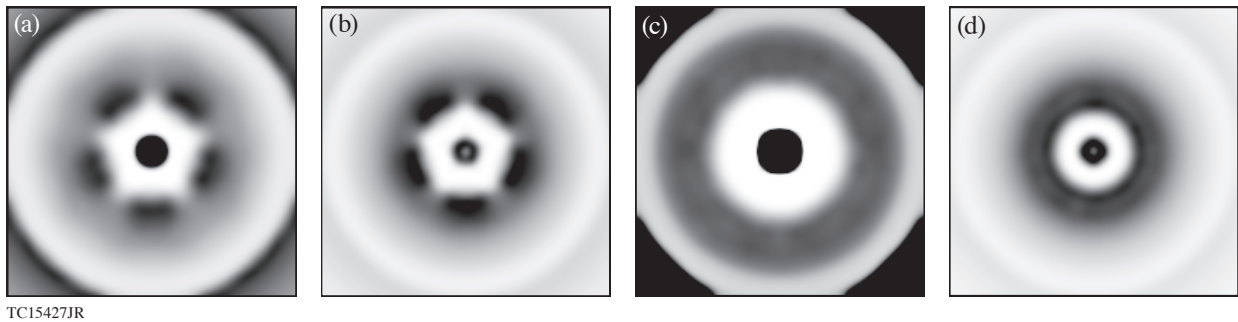


Figure 5

Images of *HYDRA* simulated x-ray radiographs of the standard pointing for (a) a 30- μm and (b) a 20- μm shell and the uniform pointing for (c) a 30- μm and (d) a 20- μm shell. The radiographs for the standard pointing exhibit the same pentagonal structure as the experimental radiographs. The uniform pointing radiographs are round to ± 1 pixel, which is the same as the experiment.

600 μm resolved by 200×200 pixels. Each image is convolved with the same point-spread function associated with the framing cameras and is processed identically to the experimental images, which is described in the previous sections. Since the images are free of noise, no error bars are reported for the mode amplitudes recovered from simulations. Residuals from the fit of Fourier decomposition to the simulated azimuthal profile are too small to represent graphically.

Uniform Pointing Results

The simulations are plotted with the experimental results for the uniform pointing in Fig. 6. Unfortunately, there are no experimental data for the 20- μm shells in this case. The briefest and most-complete summary of the uniform pointing shots is that there is no longer a mode-5 growth shown in Fig. 6 or a mode 10 imposed from the adjustments as shown in Fig. 6. The degree of uniformity of the implosion is best shown by the radiograph in Fig. 3(d).

Conclusions

Azimuthal uniformity was calculated analytically by shifting the beams to minimize the mode-5 perturbation from the standard pointing of the OMEGA laser. Data taken using the standard pointing show that, independent of cylinder outer diameter and shell thickness, a mode-5 perturbation grows as a result of the mode-5 asymmetry from the drive. The lowest-possible amplitude that gives a pentagonal-shaped shell is 6.7%, which is inferred from the different cylinder outer diameters used in the experiment.

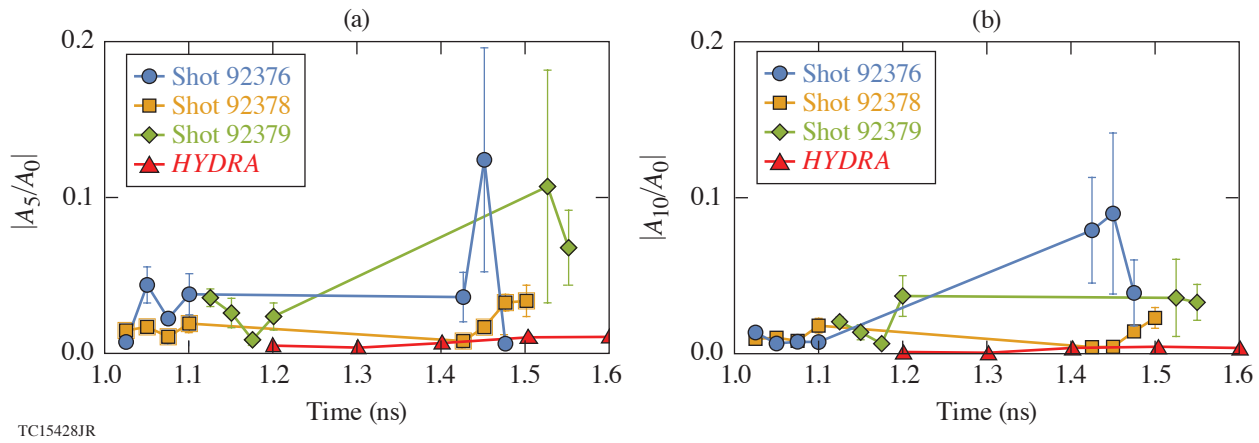


Figure 6

(a) Mode-5 and (b) mode-10 amplitudes for 30- μm -thick shells for the uniform laser drive. The *HYDRA* predictions of the mode-5 and mode-10 amplitudes for the 30- μm shells are well below the measurements later in time. The 20- μm -thick shells (not shown) have similar results from *HYDRA*.

The adjustment made to the standard pointing reduces this initial perturbation to 2.2%, which completely eliminates the observed mode 5. The increase of mode 10 as a result of this adjustment is less than the mode-5 amplitude at 2%, and no mode-10 growth on the shell is observed. The experiments are reproduced using 3-D *HYDRA* simulations, although the perturbation amplitude is overestimated for the standard pointing case. Both simulations and experiments show that the uniform pointing gives a circular implosion to within a 10- μm resolution.

The information, data, or work presented herein was funded in part by the Advanced Research Projects Agency-Energy (ARPA-E), U.S. Department of Energy, under Award No. DE-AR0000568, the Department of Energy National Nuclear Security Administration under Award No. DE-NA0001944, DE-NA0003856, and in part under contract 89233218CNA000001, the U.S. Department of Energy Office of Inertial Confinement Fusion under Cooperative Agreement No. DE-FC52-08NA28302, the University of Rochester, and the New York State Research and Development Authority. Los Alamos National Laboratory, an affirmative action/equal opportunity employer, is operated by Triad National Security, LLC for the National Nuclear Security Administration of U.S. Department of Energy under contract 89233218CNA000001.

1. S. A. Slutz *et al.*, *Phys. Plasmas* **17**, 056303 (2010).
2. S. A. Slutz and R. A. Vesey, *Phys. Rev. Lett.* **108**, 025003 (2012).
3. K. J. Peterson *et al.*, *Phys. Plasmas* **20**, 056305 (2013).
4. K. J. Peterson *et al.*, *Phys. Rev. Lett.* **112**, 135002 (2014).
5. K. J. Peterson *et al.*, *Phys. Plasmas* **19**, 092701 (2012).
6. C. W. Barnes *et al.*, *Rev. Sci. Instrum.* **70**, 471 (1999).
7. D. Tubbs *et al.*, *Laser Part. Beams* **17**, 437 (1999).
8. J. P. Sauppe *et al.*, *Matter Radiat. Extremes* **4**, 065403 (2019).
9. O. V. Gotchev *et al.*, *Phys. Rev. Lett.* **103**, 215004 (2009).
10. J. P. Sauppe *et al.*, *Phys. Plasmas* **26**, 042701 (2019).
11. E. C. Hansen *et al.*, *Plasma Phys. Control. Fusion* **60**, 054014 (2018).

12. E. C. Hansen *et al.*, Phys. Plasmas **25**, 122701 (2018).
13. A. K. Davis *et al.*, Phys. Plasmas **23**, 056306 (2016).
14. V. N. Goncharov *et al.*, Plasma Phys. Control. Fusion **59**, 014008 (2016).
15. R. S. Craxton, Laboratory for Laser Energetics Report No. DOE/DP 40200-101, University of Rochester (1989).
16. D. H. Munro and P. F. Dubois, Comp. Phys. **9**, 609 (1995).

Characterizing Laser Preheat for Laser-Driven Magnetized Liner Inertial Fusion Using Soft X-Ray Emission

D. H. Barnak,¹ M. J. Bonino,¹ P.-Y. Chang,² J. R. Davies,¹ E. C. Hansen,³ D. R. Harding,¹ J. L. Peebles,¹ and R. Betti¹

¹Laboratory for Laser Energetics, University of Rochester

²Institute of Space and Plasma Sciences, National Cheng Kung University

³Department of Physics and Astronomy, University of Rochester

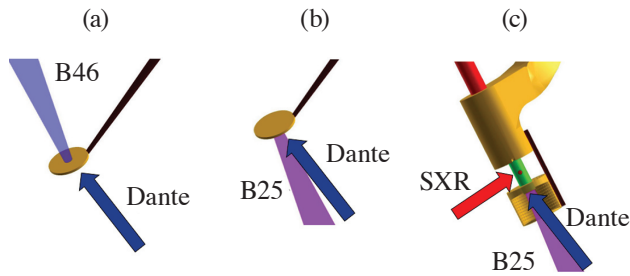
Introduction

MagLIF (magnetized liner inertial fusion) is a magnetized target fusion scheme utilizing a cylindrical implosion with an axial magnetic field to compress preheated deuterium–tritium fuel to fusion-relevant densities and temperatures. The magnetic field mitigates the radial conduction losses and allows these implosions to happen $\sim 3\times$ slower than direct or indirect laser fusion spherical implosions. The lower volume decrease with equal convergence ratios for cylinders versus spheres requires that the fuel start at a much higher temperature than in traditional inertial confinement fusion schemes. This is accomplished by using an axial laser to heat the fuel via inverse bremsstrahlung absorption prior to the implosion. In both the laser-driven and pulsed-power versions of MagLIF, the gas in the cylinder is held in by a thin window at the top that the laser must burn through to heat the gas. The most important aspects about preheat to quantify are the gas temperature as a function of time, mix due to the window being pushed into the implosion region by the preheat beam, mix due to wall ablation into the gas, and how the initial axial magnetic field affects the preheat. Characterizing the preheat process is critical to the success of MagLIF as described in several publications.^{1–4}

For the laser-driven MagLIF design, a $1.84\text{-}\mu\text{m}$ polyimide foil window was used to cover the laser entrance hole (LEH) and contain the ~ 10 atm of $2\%_{\text{at}}$ Ne-doped D_2 gas inside a parylene-AF4 ($\text{C}_8\text{H}_4\text{F}_4$) cylinder. To study the LEH window disassembly in terms of laser transmission, backscatter, sidescatter, and x-ray emission, a series of LEH foil-only shots was performed along the axis of a single beam of the OMEGA laser. LEH window shots were performed in two configurations: one to measure backscatter, sidescatter, and transmission using Beamline 25 and the other to measure transmission and forward scatter using Beamline 46. The Beamline 25 configuration was then used to heat the gas cylinders. Dante, an array of K-edge–filtered x-ray diodes, was used to measure the total x-ray flux from the LEH window disassembly, which is proportional to the laser energy absorbed by the window. The temperature of the gas in the front 1 mm of the cylinder was also measured by Dante after the window had expanded and cooled. The temperature of the wall and the gas in the implosion region was measured using a three-channel K-edge–filtered soft x-ray imager (SXR). Each configuration is illustrated in Fig. 1. Six cylinders in total were shot: two with an initial 15-T magnetic field and an initial gas density of 1.5 mg/cm^3 ; two without a magnetic field at the same gas density; one at $1/2$ the initial gas density; and one at $3/2$ the initial gas density. The transmission, backscatter, and sidescatter data from the LEH window and cylinder shots are summarized in another publication,⁵ whereas the x-ray emission and radiation temperature are presented in this summary alongside plasma temperature measurements of the gas and the wall of the cylinder as a function of time.

Analysis of LEH Window Disassembly Using Dante

An array of filtered x-ray diodes called Dante⁶ was used to characterize the x-ray spectrum and total energy of x rays emitted by the exploding window during the laser pulse. Each diode in the array has its own aperture, filter, signal cable, electrical attenuator, power tee, and transient digitizer. The combination of all of these components is referred to as a channel. Traditionally, 11 channels are employed to diagnose radiation temperatures for hohlraums. This makes Dante ideal to use for diagnosing both the LEH window-only shots and the full-cylinder preheat shots. Voltage signals from Dante are used to recover both time-resolved and time-integrated spectra of an emitting plasma.

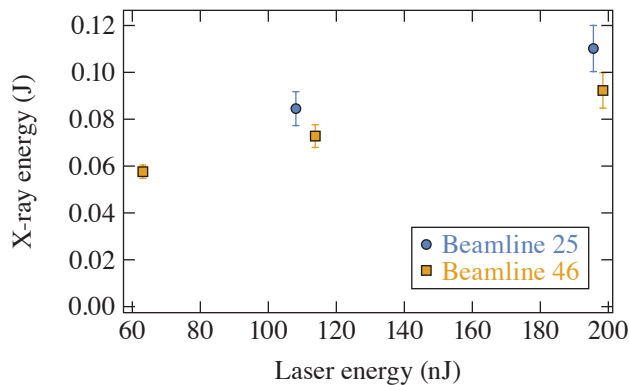


TC15397JR

Figure 1

Two opposing lasers of the OMEGA Laser System, (a) Beamline 46 and (b) Beamline 25, were used to illuminate a standalone LEH window to measure the window forward transmission, backscatter, and soft x-ray emission to track the window disassembly. (c) A Ne-doped D_2 gas inside a fluorinated plastic cylinder with an identical LEH window and a diagnostic side window drilled out of it was then heated using Beamline 25 to measure the preheat temperature over time.

With limited signal information and a unique amalgam of elements present in the plasma, several well-established methods of recovering the x-ray spectrum are impossible to employ.^{7,8} A cubic-spline spectral unfold technique⁹ was used to recover information about the total radiated power and infer the total x-ray power emitted from the LEH window. Time-integrated x-ray spectra from the LEH window-only shots show only a marginal increase in total x-ray energy emitted by the exploding window with increasing laser energy. This is consistent with the laser absorption and backscatter measurements that do not change significantly with laser energy.⁵ The total x-ray energy is found by integrating the recovered time-integrated spectrum over photon energy. The error bars on the results shown in Fig. 2 were calculated analytically according to the cubic-spline interpolation algorithm.⁹



TC15399JR

Figure 2

A summary of the x-ray energy emitted in nanojoules as a function of the laser energy incident on the LEH window-only targets. Total x-ray energy emitted by the foil is minimal and changes very little with respect to initial laser energy incident on the foil. The x-ray energy incident on Dante is also affected by which beam configuration is used. Dante looks directly at the laser-foil interaction in the Beamline 25 configuration, whereas it is blocked by the foil in the Beamline 46 configuration.

1. Comparison of Dante Data from LEH Window Shots to 2-D Simulations

Dante can also be used to verify hydrocode results for the LEH foil-only experiments. The four channels provide an entire spectral range pertinent to both the continuum and line emission relevant to polyimide plastic, and a high confidence in the plasma conditions predicted by hydrocodes can be established by direct comparison.

The output of two codes, *FLASH* and *DRACO*, is post-processed using *Spect3D* detailed atomic modeling to produce a spectrum.¹⁰ The spectrum is then convolved with the instrument and filter response functions to produce synthetic x-ray diode traces that can be compared to the data, seen in Figs. 3 and 4. For the window-only shots, *FLASH* is able to predict the plasma conditions well enough to reproduce the x-ray diode data across all channels with a margin no larger than 30%. *DRACO* can reproduce time-integrated spectra very well, but it cannot reproduce individual channel curves to the same accuracy as *FLASH*.

The discrepancy between these two codes and the experiment alludes to a mechanism of channel formation that expands and pushes away the plasma generated by the laser-window interaction, thereby limiting the amount of laser energy absorbed by the window. Despite better agreement, *FLASH* overpredicts the laser absorption in the window at $\sim 30\%$, with similar LEH burn-through times, window material propagation speed, and preheat temperatures predicted by *DRACO*. The analysis of the window x-ray emission is in good agreement with previously published data⁵ that indirectly measured laser absorption, which is shown in Fig. 5. This suggests that the source of the overestimation in both codes is missing physics.

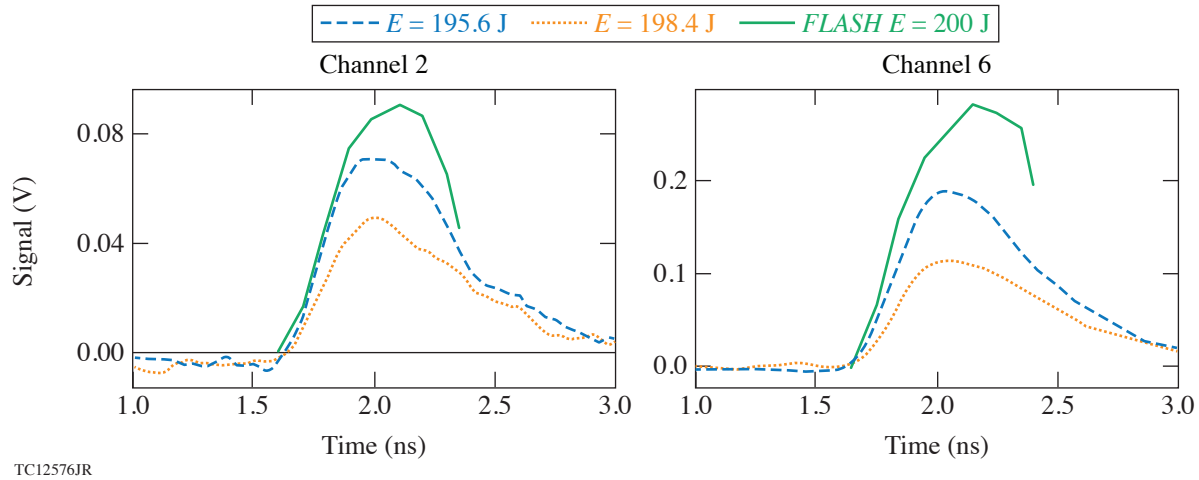


Figure 3 X-ray diode data compared to results from post-processing the 2-D hydrocode *FLASH* using *Spect3D* detailed atomic physics. The agreement between data and simulation across all x-ray diode channels is within a margin no larger than 30%.

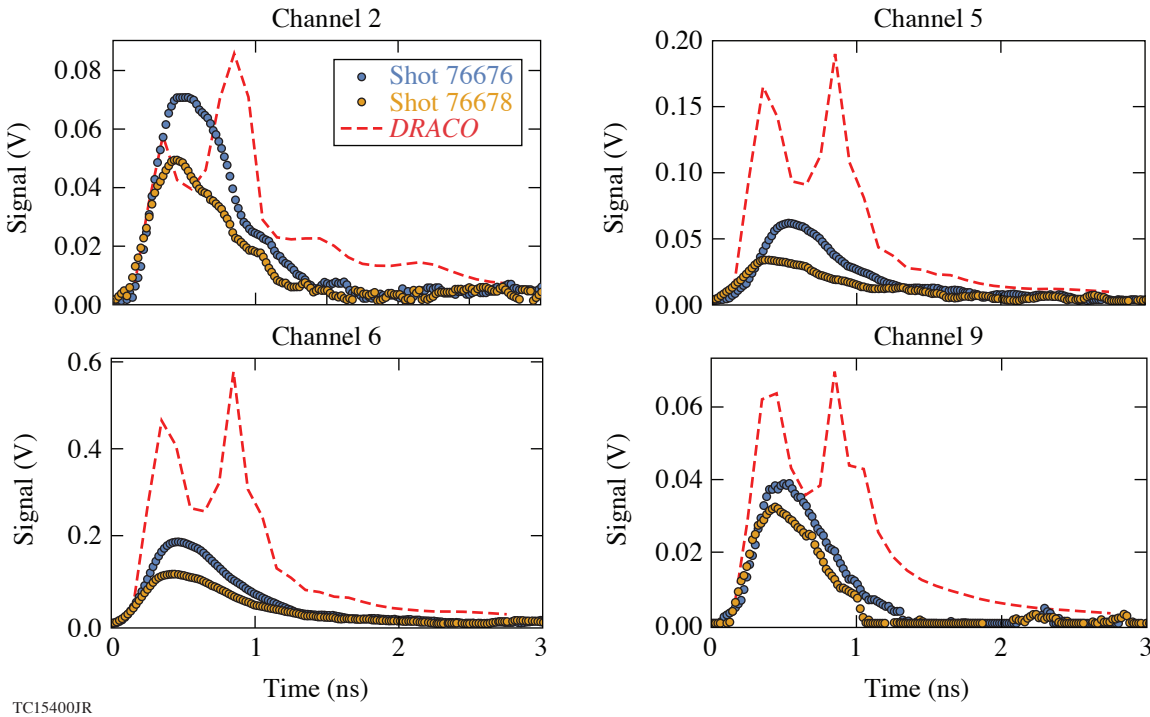


Figure 4 *DRACO* simulation results compared to Dante experimental data. The laser energy used in the simulation is 200 J, 195.6 J for shot 76676, and 198.4 J for shot 76678.

2. Inferring Gas Temperature from Dante Measurements of Cylinders

The viewing angle of Dante to the cylinder targets suggests that the first 1 mm of the target, which includes a region of gas outside of the implosion region, can be seen by Dante. A schematic view of the Dante line of sight is shown in Fig. 6. The neon doping in the gas should contribute to the x-ray spectrum in a region easily measurable by Dante, so that a gas temperature can be recovered from Dante from specific channels. Simulations from *DRACO* are used to decompose each channel into fractional contributions to the signal in each channel from the window, wall, and gas.

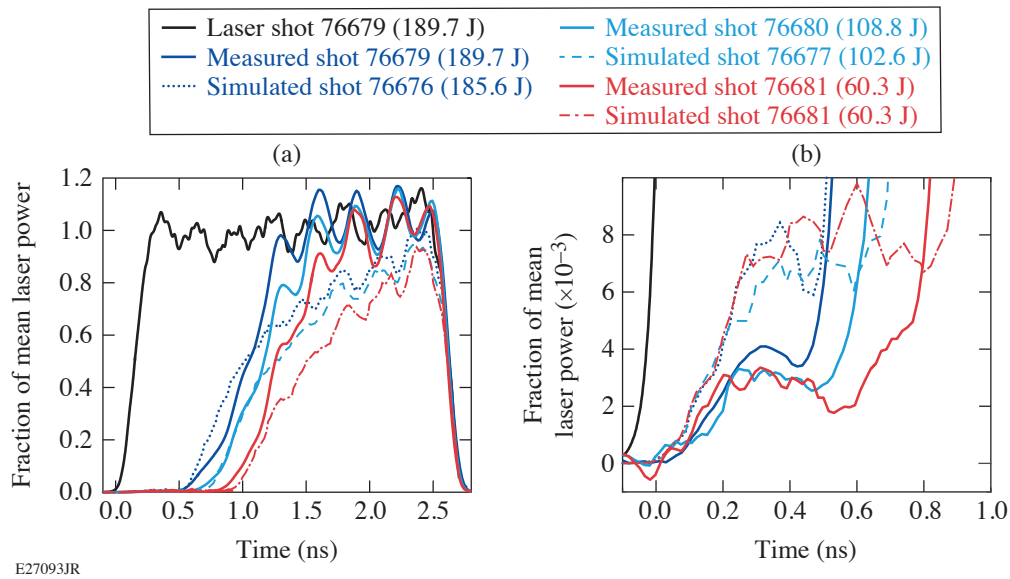


Figure 5

The laser transmission as a function of time is shown for (a) the entirety of the laser pulse and (b) at the start of the pulse in better detail. The laser absorption in the window early in time is overestimated in the simulation, but the simulations and experiments show that laser absorption is independent of the incident laser power. The experiments show the transmitted laser light quickly growing to the full power of the laser pulse, whereas the simulations reach full power only toward the end of the pulse.⁵

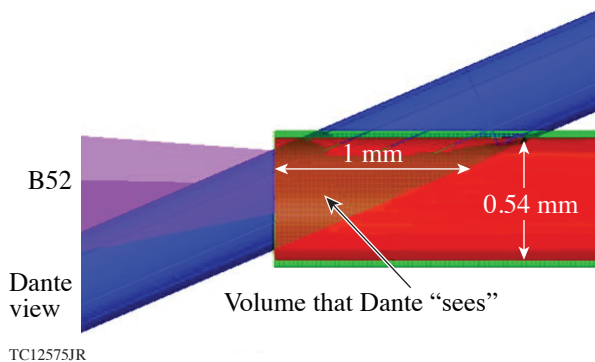


Figure 6

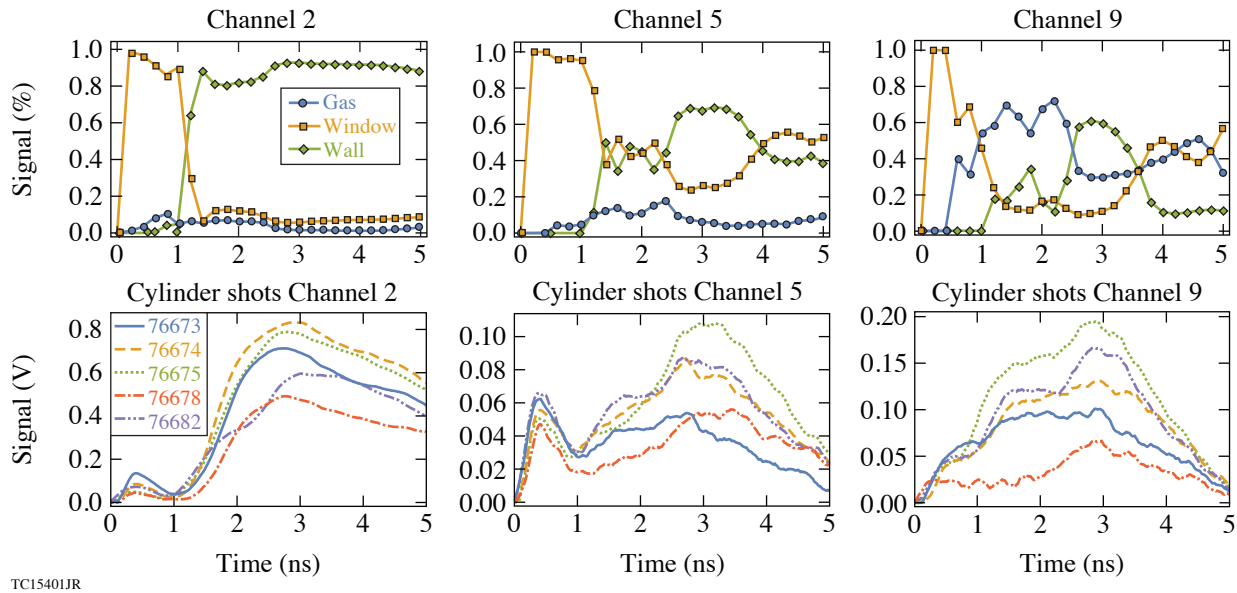
Schematic view of the Dante view down the cylinder. Dante is able to see emission from the gas as far as 1 mm into the cylinder.

To avoid issues concerning opacity, a series of three simulations from *DRACO* was post-processed in *Spect3D* considering x-ray emission from the wall only; the wall and the window; and the wall, window, and gas. A self-consistent decomposition of the percent contribution from wall, window, and gas of the signal in each channel is made. Select channels are shown decomposed into the three possible contributors along with the raw data of the corresponding channel in Fig. 7.

Based on the signal decomposition of Channel 9 from Fig. 7, times between 1.1 and 2.2 ns were considered to be the best times to compare spectra for gas emission. Instead of comparing signals convolved with instrument response functions, the adaptive cubic spline unfold method can be used to compare spectra recovered from Dante directly with *Spect3D* simulation results from *DRACO*. The spectral power emitted must be a function of electron temperature in the gas, and the data from the *DRACO* simulation are used to construct a conversion function of the form

$$k_{T_e} + b_{T_e} P_9 = T_e, \quad (1)$$

which takes the spectral power in the Channel 9 region, P_9 , and calculates the electron temperature T_e . Both k_{T_e} and b_{T_e} are free-fitting parameters with associated errors σ_k and σ_b . The spectral power over the Channel 9 region for the cubic-spline unfold is



TC15401JR

Figure 7

Decomposed signals from Channels 2, 5, and 9 are shown in percent contributions from the window, wall, and gas using results from *DRACO* post-processed in *Spect3D*. This is compared to the raw signals from the respective channels to determine the composition of the signal at different times. Lower-photon-energy channels show only window and wall emission, whereas higher-energy channels have most of their signal contributed by the gas in the front 1 mm of the cylinder. This allows Dante to be used to estimate a time-resolved gas temperature measurement.

then plugged into Eq. (1) to recover a measurement of electron temperature. The resulting error of the total calculation takes into account the error propagation of the cubic spline and the standard error of the linear model fit

$$\sigma_{T_e}^2 = (b_{T_e} P_9)^2 \left[\left(\frac{\sigma_b}{b_{T_e}} \right)^2 + \left(\frac{\sigma_{P_9}}{P_9} \right)^2 \right] + \sigma_k^2, \quad (2)$$

where σ_{P_9} is the associated error in spectral power calculated analytically from the cubic spline.⁹ The comparisons between experimentally inferred gas electron temperature and predictions by *DRACO* between 1.0 and 2.1 ns are shown in Fig. 8. The temperature from *DRACO* is calculated as a volumetric average over the front 0.5 mm of the cylinder for the full cylinder radius. The electron temperature quickly saturates at ~ 200 eV due to a drop in inverse bremsstrahlung absorption and cooling due to expansion. The ion temperature slowly thermalizes with the electron population. By the end of the laser pulse, the entirety of the cylinder including the implosion region reaches an ion temperature of 200 eV. This confirms the ability of a single OMEGA beam to reach adequate preheating conditions for a MagLIF implosion.

3. Proof of Thermal Conduction Wall Heating Suppression with Magnetic Fields

Another useful result of the signal decomposition technique is the demonstration of the reduction in wall emission and wall heating due to magnetic-field suppression of thermal conduction from the window and the gas. One of the six cylinder shots that was initially magnetized with an ~ 15 -T magnetic field prior to the start of the laser pulse has enough signal in Dante to make a comparison to the two other unmagnetized shots at equal initial gas pressure.

Looking at the signal composition for each channel from Fig. 7, the magnetic field provides an $\sim 20\%$ to 40% reduction in signal for the regions in each channel that correspond to wall emission. Since the portion of the spectrum that contributes to these channels is heavily line dominated, a 20% reduction in signal infers a significant decrease in the temperature of the wall blow-off plasma. The main mechanism in the formation of the wall blowoff is thermal conduction from the hot window plasma and gas into the wall according to 2-D simulations. This implies that the magnetic field limits the amount of thermal energy transfer from

the window and gas to the wall. Looking at Dante signal traces for Channels 2, 5, and 6, where wall emission comprises >50% of the signal in Fig. 9, the case of 15-T initial field sees a reduction in signal by about a factor of 2.

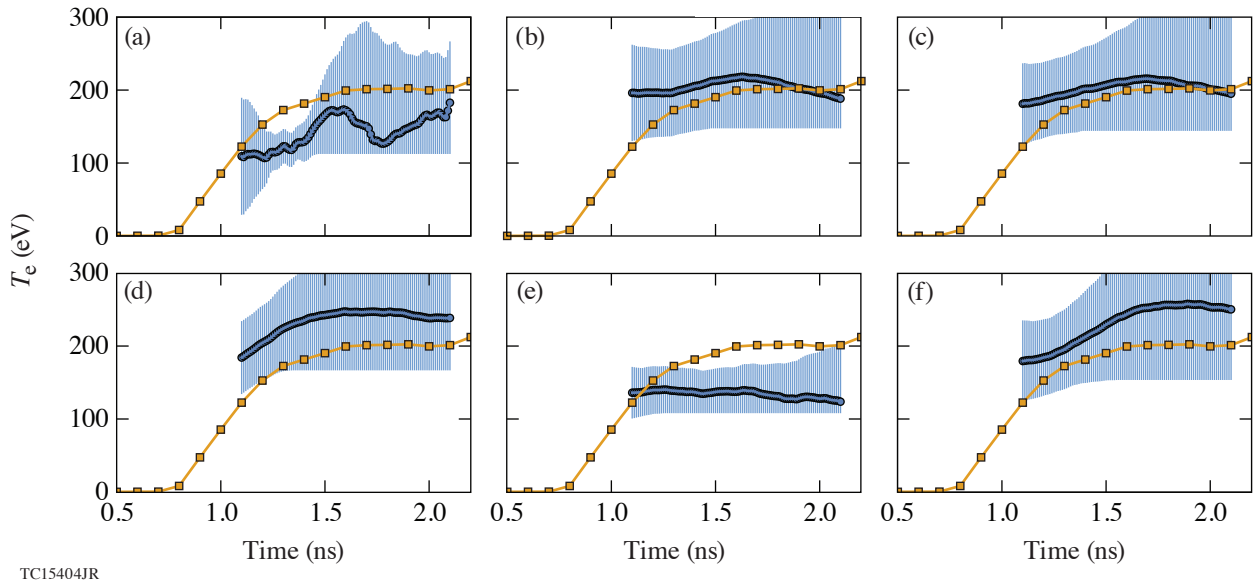


Figure 8
Preheat curves for all six cylinder shots where the squares represent results from *DRACO*. In general, the electron temperature follows the predicted *DRACO* electron temperatures fairly closely, within shot-to-shot variations. Comparisons between [(a), (b)] shots with and [(c), (d)] shots without an initial axial magnetic field show no appreciable difference between electron temperatures. A shot with (e) 5-atm initial pressure shows less preheating than the 10-atm *DRACO* prediction and (f) a shot with a higher initial pressure shows greater preheating than the 10-atm prediction. It can even be implied that (d) has roughly the same initial pressure as (f), although no direct measurement of the gas pressure exists for these two cases.

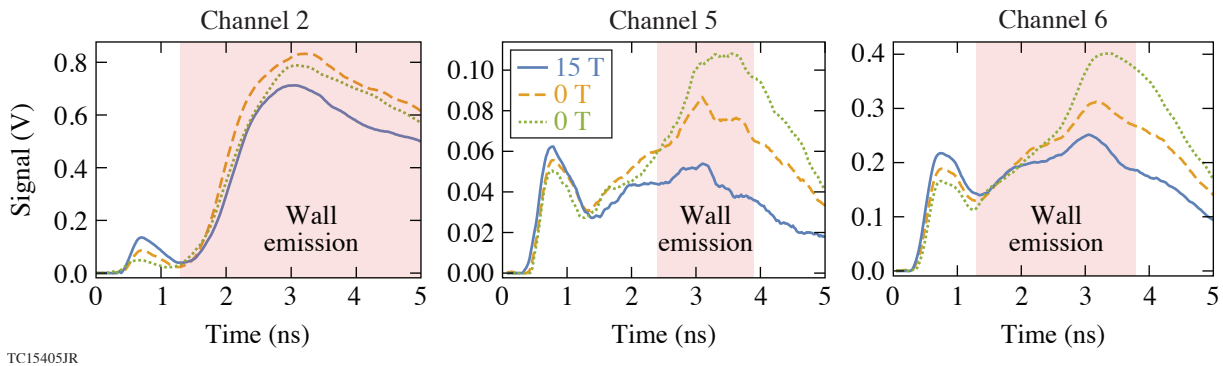


Figure 9
Raw Dante signals for Channels 2, 5, and 6 for the cases of 15 T and 0 T. In every channel where wall emission comprises >50% of the signal (shaded region), the case with 15-T initial field has an ~20% to 40% decrease in signal.

Measuring Gas Temperature in the Implosion Region Using Ne Soft X Rays

The cylinder experiments used a diagnostic window drilled into the side and resealed with a 1.84- μm polyimide film to look at soft x-ray emission from the gas and the wall. Spatially and temporally resolved images of the side diagnostic window are measured using SXR, which is a three-channel differentially filtered imager. The spectral responses of each filtered channel are shown in Fig. 10.

There is no possible way to recover the spectrum of the plasma from these three channels. Furthermore, SXR is not an absolutely calibrated diagnostic, so each channel signal must be compared with another for any useful information to be extracted. Using results from 2-D hydrocodes as a guide, a set of possible 2-D plasma profiles was constructed. The spectrum for each possible combination of temperature and density is calculated using *Spect3D* detailed atomic modeling and then convolved with response functions of SXR to generate a grid of possible solutions. The channel ratios from the data are then converted to temperature and density by using the solution grid under the condition that $T_{\text{gas}} > T_{\text{wall}}$. Since the system is highly degenerate, the main result from this analysis establishes a lower bound on the possible gas temperature of 100 eV at 1.3 ns into the laser pulse, which is shown in Fig. 11. This result is consistent with the Dante-inferred temperatures toward the front of the cylinder and confirms that the goal of at least a 100-eV preheat is achieved with a single OMEGA laser beam.

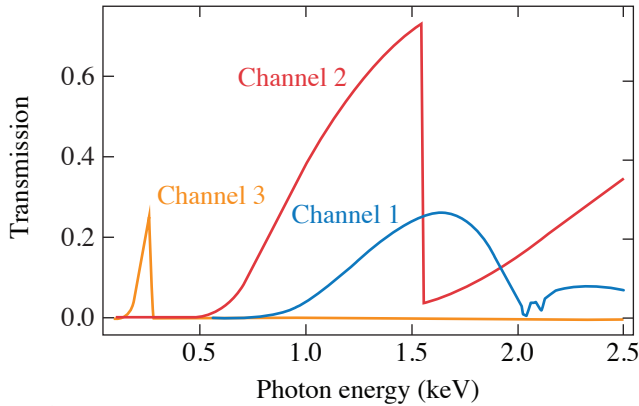


Figure 10
Response functions for the three channels of SXR used to measure preheat temperature.

TC12574JR

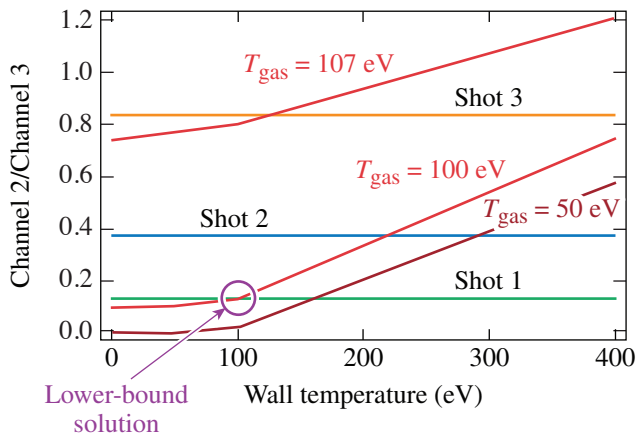


Figure 11
The lower-bound solution for the temperature of the preheated D₂ gas. Other channel ratios give a solution higher than 100 eV. The solutions always find the case where $T_{\text{gas}} = T_{\text{wall}}$ given the constraint of $T_{\text{gas}} \geq T_{\text{wall}}$ as shown in the plot.

TC13143JR2

Conclusions

Measurements of the LEH window disassembly in terms of total emitted x-ray energy demonstrate that there is a small variation of laser light absorbed by the window as a function of the intensity of the laser. This is consistent with results obtained from analysis of the backscatter and sidescatter measurements. Furthermore, both *DRACO* and *FLASH* overpredict the amount of laser energy absorbed by the window during disassembly, and the difference between the two codes suggests that the reason for this may be related to instabilities such as laser self-focusing and ponderomotive pressure applied by the laser field that causes the window to form a channel into the gas. Despite overpredicting the window absorption, the plasma temperature evolution is the same between the simulation predictions and experiment as expected for inverse bremsstrahlung heating. Lower initial gas density is shown to lower the preheat, and higher initial density is shown to raise the total preheat relative to the simulation predictions

for the nominal case. There is no discernible difference between magnetized and unmagnetized preheat in terms of the electron temperature within the shot-to-shot variation and calculated error bars. The plasma temperature in the implosion region has been shown to meet the 100-eV requirement set in the point design specifications, although measuring the time evolution of the laser heating in the implosion region proved to be impossible. Implosion-region measurements are consistent with the measurements made of the front 1 mm of the cylinder and simulation results. The comparisons between the experimental results and simulations indicate that using *DRACO* as a prediction for the design of future preheating schemes is adequate.

The information, data, or work presented herein was funded in part by the Advanced Research Projects Agency-Energy (ARPA-E), U.S. Department of Energy, under Award No. DE-AR0000568, the Department of Energy National Nuclear Security Administration under Award No. DE-NA0003856, and in part under contract 89233218CNA000001, the U.S. Department of Energy Office of Fusion Energy Sciences under award No. DE-SC0016258, the U.S. Department of Energy Office of Inertial Confinement Fusion under Cooperative Agreement No. DE-FC52-08NA28302, the University of Rochester, and the New York State Research and Development Authority. Los Alamos National Laboratory, an affirmative action/equal opportunity employer, is operated by Triad National Security, LLC for the National Nuclear Security Administration of U.S. Department of Energy under contract 89233218CNA000001.

1. A. J. Harvey-Thompson *et al.*, *Phys. Plasmas* **22**, 122708 (2015).
2. M. Geissel *et al.*, *Phys. Plasmas* **25**, 022706 (2018).
3. A. J. Harvey-Thompson *et al.*, *Phys. Plasmas* **26**, 032707 (2019).
4. A. J. Harvey-Thompson *et al.*, *Phys. Plasmas* **25**, 112705 (2018).
5. J. R. Davies *et al.*, *Phys. Plasmas* **25**, 062704 (2018).
6. C. Sorce *et al.*, *Rev. Sci. Instrum.* **77**, 10E518 (2006).
7. R. E. Marrs *et al.*, *Rev. Sci. Instrum.* **86**, 103511 (2015).
8. A. Seifter and G. A. Kyrala, *Rev. Sci. Instrum.* **79**, 10F323 (2008).
9. D. H. Barnak *et al.*, *Rev. Sci. Instrum.* **91**, 073102 (2020).
10. J. J. MacFarlane *et al.*, in *Inertial Fusion and Sciences Applications 2003*, edited by B. A. Hammel *et al.* (American Nuclear Society, La Grange Park, IL, 2003), pp. 457–460.

Constraining Physical Models at Gigabar Pressures

J. J. Ruby,^{1,2} J. R. Rygg,^{1,2,3} D. A. Chin,^{1,2} J. A. Gaffney,⁴ P. Adrian,⁵ D. Bishel,^{1,2} C. J. Forrest,² V. Yu. Glebov,²
 N. V. Kabadi,⁵ P. M. Nilson,² Y. Ping,⁴ C. Stoeckl,² and G. W. Collins^{1,2,3}

¹Department of Physics & Astronomy, University of Rochester

²Laboratory for Laser Energetics, University of Rochester

³Department of Mechanical Engineering, University of Rochester

⁴Lawrence Livermore National Laboratory

⁵Plasma Science and Fusion Center, Massachusetts Institute of Technology

Large-scale, high-energy-density (HED) experimental facilities are able to generate states of matter that push beyond the limits of where most physical models were developed. This necessitates quantitative experiments to guide theories and techniques at such conditions. Convergent geometries, either spherical or cylindrical, amplify the pressure generated from HED drivers, such as lasers or pulsed-power machines, and create the most-extreme thermodynamic states currently achievable in the laboratory. These convergent experiments complicate measurements, however, making it difficult to directly measure the state of variables and transport properties. Often, measurements are the result of an integrated system, where many properties of the system are responsible for observations, rather than a small number of key physical quantities. Such integrated system analysis requires a new way of approaching how experimental data are interpreted.

This work proposes using the well-established methodology of Bayesian inference^{1,2} to derive quantitative physical information from integrated HED experiments. This process includes the synthesis of a model that contains the essential physics from the experiment and is used in a forward analysis, generating synthetic experimental data to directly compare to the measurements. Given the proper parameterization and set of measurements the model can be constrained, giving a quantitative assessment of the input parameters.

This process is demonstrated using a direct-drive exploding-pusher experiment carried out on the 60-beam OMEGA Laser System, where the trajectory of an exploding shell is measured via x-ray self-emission on an x-ray framing camera. Synthetic data generated using the 1-D hydrodynamics code *LILAC* is also analyzed, confirming that the parameterization accurately represents the physical quantities of interest. The process is used to infer the temporal pressure profile felt by an in-flight shell and the subsequent trajectory from experimental measurements, demonstrating how a large amount of physical insight can be gained by using integrated measurements.

The model used to describe the experimental data is a thin-shell subject to force pushing in to greater convergence due to mass ablation and an outward force resisting convergences due to pressure from the compressed fuel. The equation of motion

$$\frac{d^2 R}{dt^2} = a, \tag{1}$$

is solved, where R is the trajectory of the shell and a is the acceleration given by

$$a(t) = \begin{cases} 0 & t < t_a \\ \frac{4\pi R^2 P}{M} - \frac{\dot{M}v_e}{M} & t_a \leq t < t_1 \\ \frac{4\pi R^2 P}{M} & t \geq t_1 \end{cases} \quad (2)$$

where P is pressure at the fuel–shell interface given by

$$P(t) = \begin{cases} (P_{rs})e^{-\gamma_g(t_s - t)} & t \leq t_s \\ (P_{rs})e^{-\gamma_d(t - t_s)} & t \geq t_s \end{cases} \quad (3)$$

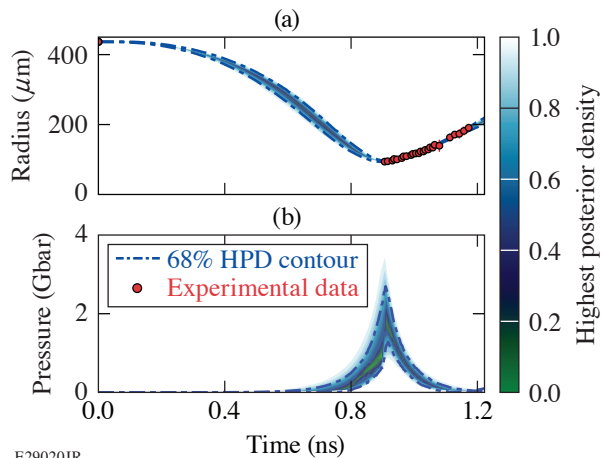
and M is the shell mass given by

$$M(t) = \begin{cases} M_0 - \dot{M}(t - t_a) & t \leq \min[t_s, t_M] \\ M_{\min} + \dot{M}[t - \min(t_s, t_M)] & t > \min[t_s, t_M] \end{cases} \quad (4)$$

with \dot{M} and all subscripted variables parameters in the model.

The resulting trajectory and pressure profile that follow from the Bayesian inference process are shown in Figs. 1(a) and 1(b), respectively. The framing-camera measurements of the outgoing shell trajectory, in conjunction with conservation laws and initial conditions, are sufficient to constrain the shell trajectory at all times, from laser on to shell decompression, and also to constrain the pressure profile at the fuel–shell interface.

The methods presented here showed how a seemingly isolated, integrated measurement of an evolving system can be used to reconstruct a model of the entire system with enough fidelity to gain quantifiable physical insight. This methodology has a strong



E29020JR

Figure 1

The highest posterior density (HPD) confidence intervals for the (a) shell trajectory and (b) pressure profile at the fuel–shell interface determined from fitting the shell model described here. The trajectory measurements of the outgoing shell and initial conditions of the shell are sufficient to constrain the trajectory and pressure at all times.

history of being used in other fields of physics and has the potential to greatly impact HED physics by making possible quantified measurements in conditions otherwise inaccessible.

The combination of high-quality experimental methods and facilities that already exist in HED physics are able to create conditions otherwise impossible on Earth, and new analysis techniques for integrated measurements promise to provide new insight into our understanding of physics at extreme conditions.

This material is based upon work supported by the Department of Energy National Nuclear Security Administration under Award Number DE-NA0003856, the U.S. Department of Energy, Office of Science, Office of Acquisition and Assistance under Award No. DE-SC001926, the University of Rochester, and the New York State Energy Research and Development Authority.

1. J. A. Gaffney *et al.*, Nucl. Fusion **53**, 073032 (2013).
2. M. F. Kasim *et al.*, Phys. Plasmas **26**, 112706 (2019).

Molecular Dynamics Simulations Reveal Hydrogen Streaming upon Release from Polystyrene Shocked to Inertial Confinement Fusion Conditions

S. Zhang and S. X. Hu

Laboratory for Laser Energetics, University of Rochester

Shock release from inertial confinement fusion (ICF) shells poses a great challenge to radiation-hydrodynamic simulations because the kinetic effects and large Knudson numbers are beyond the regular single-fluid approximation and cannot be included in standard equation-of-state (EOS) models. This has been evidenced by a recent experiment¹ on polystyrene (CH), in which low-density plasmas (10^{19} to 10^{20} cm⁻³) released from a laser-shocked CH shell were observed to travel significantly ahead of what regular hydro-simulations predict. Further hydro-simulations were rendered to agree with experiments by *assuming* excessive pre-expansion at the rear surface of the CH shell before arrival of the shock. In this work, we take a novel route to elucidate the microscopic shock-release physics of CH by large-scale nonequilibrium molecular dynamics (MD) at the experimental conditions. Our results revealed species separation and hydrogen streaming out of CH upon shock release and provided excellent explanation to experimental observations. Such kinetic effect of species separation as revealed by our simulations is currently missing in single-fluid radiation-hydrodynamic simulations, which could have profound implications to ICF target designs.

CH is an important ablator material in ICF and high-energy-density experiments. In experiments, it can be shocked to warm-dense-matter states with multimegabar pressures and tens-of-electron-volt temperatures, while the unshocked regime remains under ambient conditions; after shock breakout, electron-ion recombination occurs and chemical bonding may be expected while the system is cooling down. The various pressures and temperatures and distinction between up- and downstream of the shock front challenge regular hydro-simulations that are based on the single-fluid approximation and MD simulations that use empirical potentials. Previous MD studies of hydrocarbons are limited to pressures up to ~ 200 GPa (Refs. 2–4). Recently, we have developed an approach that uses many-body reactive force fields, combines with first-principles ionization models, and greatly extends the regime of fidelity of the MD simulations to ~ 2100 GPa (associated shock velocity ~ 55 km/s, temperature $\sim 1.5 \times 10^5$ K), which is more than $10\times$ the maximum previous record. This approach is justified according to benchmark calculations of various atomistic models with up to several million atoms, which uniformly show small differences (3%–20%) in the Hugoniot EOS in comparison with those predicted by accurate first-principles calculations.⁵

By studying the time evolution of spatial and velocity distributions of hydrogen and carbon after shock breakout, we find that hydrogen atoms stream far ahead of carbon. In addition, the motion of both species is linear throughout the simulation, whereas hydrogen travels much faster than carbon, more so at the lower density of 10^{19} than at 10^{20} cm⁻³ [Fig. 1(a)]. In comparison with the experiment, the hydrogen velocities calculated from our MD simulations at both densities of 10^{19} and 10^{20} cm⁻³ compare favorably well with the measured values, while the carbon velocity along with its dependence on density is clearly off trend [Fig. 1(b)]. Furthermore, by exponentially fitting the hydrogen distribution profile at 10^{19} to 10^{20} cm⁻³, we estimated the plasma scale length and found that it increases tenfold from 2 to 10 ps [Fig. 1(c)].

We note that the above comparisons to experimentally measured plasma properties are based on the assumption that $\langle Z \rangle = 1$. While this provides a reasonable estimation for the upper bound of hydrogen ionization, we notice that the temperature remains above 10,000 to 30,000 K until after 10 ps. We have, therefore, performed average-atom model calculations⁶ using density functional theory for carbon and hydrogen plasmas at the temperature of 20,000 K and densities between 10^{19} to 10^{20} cm⁻³ to estimate a lower bound for the ionization. From these calculations, we have found $\langle Z \rangle$ to be approximately 0.5. Therefore, we have

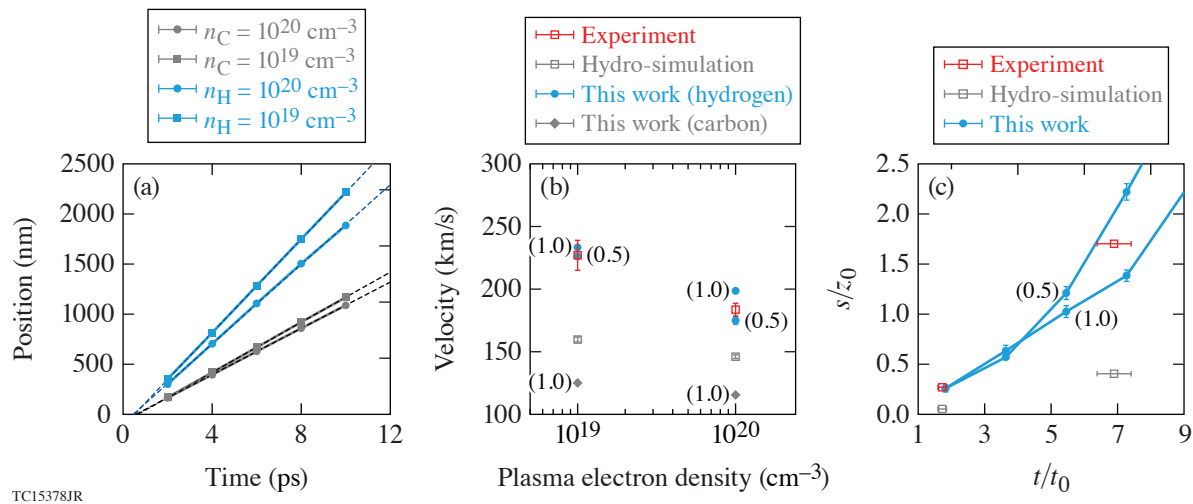


Figure 1

(a) Drifting of carbon and hydrogen, (b) plasma velocities, and (c) scale lengths (normalized by sample thickness z_0) as a function of time (normalized by shock duration t_0) at 10^{19} and 10^{20} cm^{-3} according to our simulations of shock-released CH and in comparison with experiment and regular single-fluid hydro-simulations from Ref. 1. The solid lines in (a) and (c) are guides to the eyes and the dashed lines in (a) are linear fits to the data. In (b) and (c), error bars denote the fit error; the labels of “1.0” and “0.5” indicate the estimated charge state $\langle Z \rangle$ for carbon or hydrogen.

considered the range of $\langle Z \rangle = 0.5$ to 1 to directly compare with the experimental results. For the lower bound of $\langle Z \rangle = 0.5$, the re-evaluated plasma velocity decreases slightly by 7 km/s at 10^{19} cm^{-3} and by 24 km/s at 10^{20} cm^{-3} , while scale length remains constant at 2 ps but increases by the amount of sample thickness (z_0) at 10 ps. Giving these ionization estimates, the hydrogen plasma velocities and scale lengths all match the experimental values very well (Fig. 1).

These results provide a clear microscopic picture of post-shock-release hydrogen streaming that offers an important factor to be considered in improving radiation-hydrodynamic simulations. We expect similar species-separation processes can occur during shock release of deuterium–tritium (DT) fuel in ICF implosions, especially for strong shocks. The other implication to ICF is the likely hydrogen streaming into the DT layer upon shock transits through DT/CH interfaces, which might induce atomic mixing, thereby reducing the final compression areal density.

This material is based upon work supported by the Department of Energy National Nuclear Security Administration under Award Number DE-NA0003856, the University of Rochester, and the New York State Energy Research and Development Authority.

1. D. Haberberger *et al.*, Phys. Rev. Lett. **123**, 235001 (2019).
2. S. Root *et al.*, J. Appl. Phys. **114**, 103502 (2013).
3. T. R. Mattsson *et al.*, Phys. Rev. B **81**, 054103 (2010).
4. T. C. O’Connor *et al.*, Phys. Rev. Mater. **2**, 035601 (2018).
5. S. Zhang *et al.*, J. Chem. Phys. **148**, 102318 (2018).
6. S. X. Hu *et al.*, Phys. Plasmas **23**, 042704 (2016).

Impact of Spatiotemporal Smoothing on the Two-Plasmon–Decay Instability

D. Turnbull, A. V. Maximov, D. Cao, A. R. Christopherson, D. H. Edgell, R. K. Follett, V. Gopaldaswamy, J. P. Knauer, J. P. Palastro, A. Shvydky, C. Stoeckl, H. Wen, and D. H. Froula

Laboratory for Laser Energetics, University of Rochester

Higher levels of hot electrons from the two-plasmon–decay (TPD) instability are observed when smoothing by spectral dispersion (SSD)¹ is turned off in directly driven inertial confinement fusion experiments at the Omega Laser Facility. This finding is explained using a hot-spot model based on speckle statistics and simulation results from *LPSE*. The model accurately reproduces the relative increase in hot-electron activity at two different drive intensities, although it slightly overestimates the absolute number of hot electrons in all cases. Extrapolating from the current ≈ 360 -GHz system while adhering to the logic of the hot-spot model suggests that larger SSD bandwidth should significantly mitigate hot-electron generation; legacy 1-THz OMEGA experiments appear to support this conclusion. These results demonstrate that it is essential to account for laser speckles and spatiotemporal smoothing to obtain quantitative agreement with experiments.

The TPD instability—in which an electromagnetic pump decays into two electron plasma waves near the quarter-critical density $n_c/4$ —has long been a concern for directly driven inertial confinement fusion. This stems primarily from its tendency to generate hot electrons² that can preheat the fuel and decrease the areal density of the compressed shell.³ Although there has been extensive effort to understand many aspects of TPD, little consideration has been given to the impact of laser beam speckles and spatiotemporal smoothing schemes, despite the fact that they are ubiquitous features of modern experiments.

In this summary, we present experimental evidence that SSD does partially mitigate TPD (conversely, turning off SSD enhances TPD) in implosions at the Omega Laser Facility. The experiments used 860- μm -diam, 27- μm -thick, vacuum-filled spherical CH targets illuminated by all 60 OMEGA beams. On every shot, the beams were conditioned with distributed polarization rotators (i.e., polarization smoothing) and “SG5” phase plates. Both high- and low-power versions of a similar pulse shape [cf. Fig. 1(a)] were used in order to see how the impact of SSD on TPD activity varied with proximity to the TPD threshold. For each pulse shape, the SSD bandwidth was also tuned between shots from 100% (of the current ≈ 360 GHz) down to 50% and, ultimately, to zero. While varying the SSD bandwidth, laser amplifier settings were adjusted to reproduce the same delivered pulse shape. Radiation-hydrodynamic simulations using the *LILAC* code, including nonlocal and cross-beam energy transfer models, give the following quarter-critical conditions during the period of TPD activity: overlapped intensity $I_{14} = 3.5$ (in units of 10^{14} W/cm²), electron temperature $T_e = 2.4$ keV, and density scale length $L = 160$ μm for the high-power case (respectively, $I_{14} = 2.8$, $T_e = 2.25$ keV, and $L = 160$ μm for the low-power case).

The time-resolved hot-electron power for both the full-SSD and no-SSD shots of the two different pulse shapes are shown in Fig. 1(a), which shows that turning SSD off increased hot electrons in both cases. The total energy in hot electrons for each shot is shown in Fig. 1(b), with high power giving a more-than-twofold increase over the low-power pulse shape. The impact of SSD on TPD activity is most clearly seen in Fig. 1(c), which shows the change in hot electrons for each of the reduced-SSD shots relative to their full-SSD companions. There is a modest increase in TPD activity at 50% SSD and a much larger increase when SSD is turned off completely. It also shows that the relative effect of SSD on TPD is consistently larger at low power, closer to the TPD threshold. These measurements were obtained using the hard x-ray detector (HXRD). Note that the data have small relative error ($\approx 1\%$, comparable to the marker width) dominated by noise, but the systematic error could be as large as $\approx 50\%$.

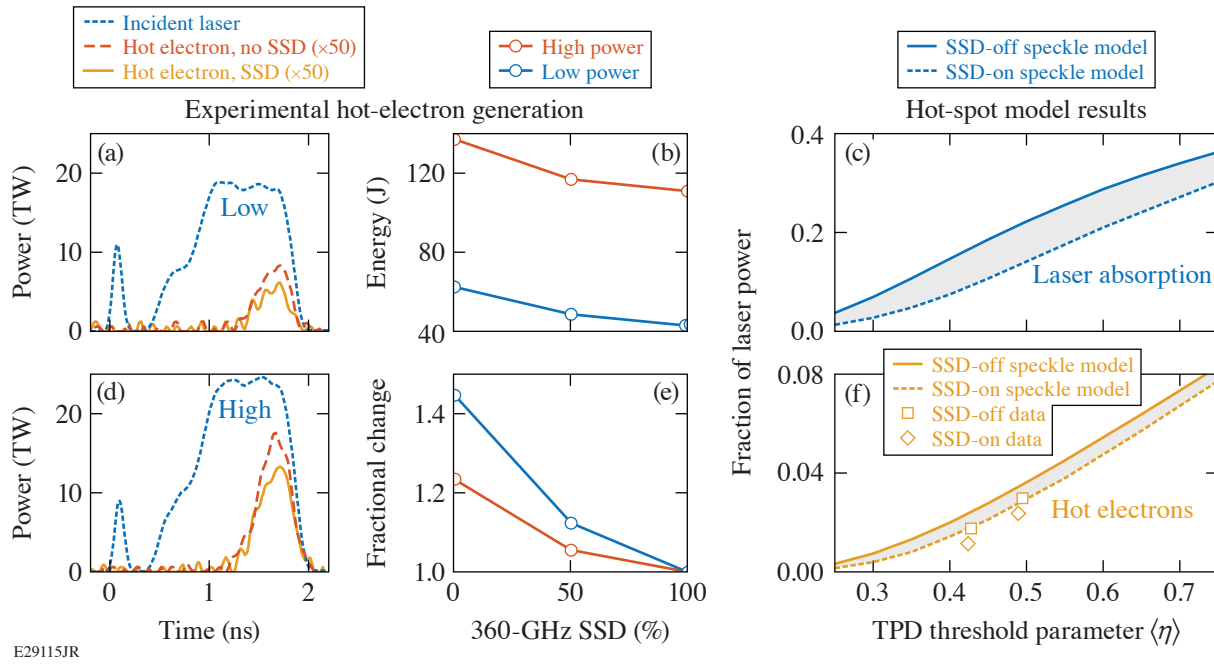


Figure 1

(a) For each pulse shape (high and low power), the SSD-off delivered laser pulse is shown alongside the hot-electron power for both the SSD-on and SSD-off cases. (b) The total energy in hot electrons for each shot is plotted as a function of the percentage of the current maximum SSD bandwidth. Reducing SSD increases the number of hot electrons. (c) The same hot-electron energies are shown normalized by their full-SSD companions, which shows that SSD has a relatively larger effect at low power. [(d),(e)] The hot-spot model. TPD activity, with (dashed) and without (solid) current OMEGA SSD, predicted as a function of average TPD threshold parameter, both in terms of (d) laser absorption, and (e) hot-electron generation. The data from the experiments (symbols) are in reasonably good agreement but all lie $\approx 20\%$ below their respective curves.

It has long been recognized that in many situations laser–plasma instability growth is primarily determined by high-intensity speckles.⁴ If intense speckles dominate instability growth, the speckle motion induced by spatiotemporal smoothing schemes can potentially mitigate instability growth. The lowest-order effect is the elimination of filamentation. Absent filamentation, it was found that speckle motion can reduce stimulated Brillouin scattering (SBS) directly if the laser coherence time is less than the time it takes the instability to reach steady state.^{5–7} Stimulated Raman scattering (SRS), on the other hand, was thought to grow too quickly for speckle motion to provide direct mitigation. Like SRS, TPD produces electron plasma waves as primary daughter waves, so one might naively assume that TPD also grows too quickly for direct mitigation. It is important to recognize, however, that absolute instability plays a key role in OMEGA-scale TPD,⁸ which implies that growth is unbounded until nonlinear saturation mechanisms set in. Since the strongest such mechanism is mode coupling to low-frequency ion-acoustic waves, saturation actually occurs on ion time scales more similar to SBS or filamentation, thereby facilitating direct mitigation by speckle motion.

Simulations with *LPSE* show that the speckles resulting from beam smoothing reduce the absolute TPD threshold by about a factor of 3 compared to the single-beam plane-wave⁹ threshold $\eta = I_{14}L/(233T_e)$, where I_{14} is the intensity in units of 10^{14} W/cm², L is the scale length in μm , and T_e is the electron temperature in keV (all specified at the quarter-critical density). This is due to the fact that a significant fraction of the laser power is carried by speckles with a maximum intensity of more than $3\times$ the average, and such speckles can therefore exceed the threshold locally. The region in parameter space in between the speckled-beam threshold and the plane-wave threshold (which is also where OMEGA experiments are situated) is exactly where spatiotemporal smoothing can have a big impact.

The *LPSE* simulations provided the following information to guide a hot-spot model: (1) the single-speckle TPD threshold is $\eta \approx 1.31$, where the speckle’s peak intensity is used in the Simon threshold formula; (2) speckles in the range $1.31 < \eta < 2$ take ≈ 20 ps to reach saturation (much longer than the laser coherence time with SSD: $\approx 360 \text{ GHz}^{-1} \approx 3 \text{ ps}$) and are therefore likely to

be stabilized by SSD, whereas speckles with $\eta > 2$ take less than 3 ps to reach saturation; (3) the scaling for laser absorption versus speckle intensity is $A = 0.66[(\eta - 1.31)/\eta]^{0.5}$; and (4) the scaling for hot-electron generation is $f_{\text{hot}} = 0.07[(\eta - 1.31)^{0.09}]$. Applied to a power-weighted speckle probability distribution derived from Garnier,¹⁰ the scalings can be used to determine total TPD laser absorption and hot-electron generation, for any average laser intensity, with SSD on (integrating only the activity in speckles with $\eta > 2$) or off (integrating all activity in speckles with $\eta > 1.31$). The results are shown in Figs. 1(d) and 1(e).

The experimental data included in Fig. 1(e) show that the fraction of laser power into hot electrons is as high as 3% for the case of high intensity without SSD. Definitions are very important here, and these values were obtained by comparing the average hot-electron power over 200 ps of the maximum TPD activity shown in Figs. 1(a) and 1(c) to the average laser power reaching $n_c/4$ according to the *LILAC* simulations over that same duration. The data lie below the speckle model by $\approx 20\%$. It is apparent, however, that the speckle model accurately reproduces the expected changes in TPD activity going both from low to high power, as well as from SSD on to SSD off. There are many possible explanations for the small remaining discrepancy, the most likely being the large systematic errors in quantifying the hot-electron activity ($\approx 50\%$), as well as the fact that the hot-spot model is trained on 2-D rather than 3-D simulations.

This material is based upon work supported by the Department of Energy National Nuclear Security Administration under Award Number DE-NA0003856, the University of Rochester, and the New York State Energy Research and Development Authority.

1. S. Skupsky *et al.*, J. Appl. Phys. **66**, 3456 (1989).
2. C. Stoeckl *et al.*, Phys. Rev. Lett. **90**, 235002 (2003).
3. V. A. Smalyuk *et al.*, Phys. Rev. Lett. **100**, 185005 (2008).
4. H. A. Rose and D. F. DuBois, Phys. Rev. Lett. **72**, 2883 (1994).
5. R. L. Berger *et al.*, Phys. Rev. Lett. **75**, 1078 (1995).
6. P. Mounaix *et al.*, Phys. Rev. Lett. **85**, 4526 (2000).
7. L. Divol, Phys. Rev. Lett. **99**, 155003 (2007).
8. J. Zhang *et al.*, Phys. Rev. Lett. **113**, 105001 (2014).
9. A. Simon *et al.*, Phys. Fluids **26**, 3107 (1983).
10. J. Garnier, Phys. Plasmas **6**, 1601 (1999).

Vacuum Acceleration of Electrons in a Dynamic Laser Pulse

D. Ramsey,^{1,2} P. Franke,^{1,2} T. T. Simpson,^{1,2} D. H. Froula,^{1,2} and J. P. Palastro¹

¹Laboratory for Laser Energetics, University of Rochester

²Department of Physics & Astronomy, University of Rochester

Vacuum laser acceleration (VLA) exploits the large electromagnetic fields of high-intensity laser pulses to accelerate electrons to relativistic energies over short distances.¹ The field of an intense pulse can far surpass that in conventional radio-frequency (rf) or advanced plasma-based accelerators, and the underlying interaction—involving only an electron and the electromagnetic field—has an appealing simplicity.

In the strong electromagnetic fields characteristic of pulses delivered by modern laser systems, nonlinear forces become a predominant driver of electron motion. Accordingly, many VLA schemes utilize the ponderomotive force, which pushes electrons against the gradient of the local intensity. For planar pulses, however, the ponderomotive force is insufficient to achieve net energy gains: The rising edge of an intensity peak that travels at the vacuum speed of light (c) will accelerate an electron in the direction of propagation, but the falling edge will eventually overtake and decelerate the electron back to rest [Fig. 1(a)]. To overcome this symmetry and impart net energy to an electron, the speed of the intensity peak must be subluminal, i.e., $|v_I| < c$.

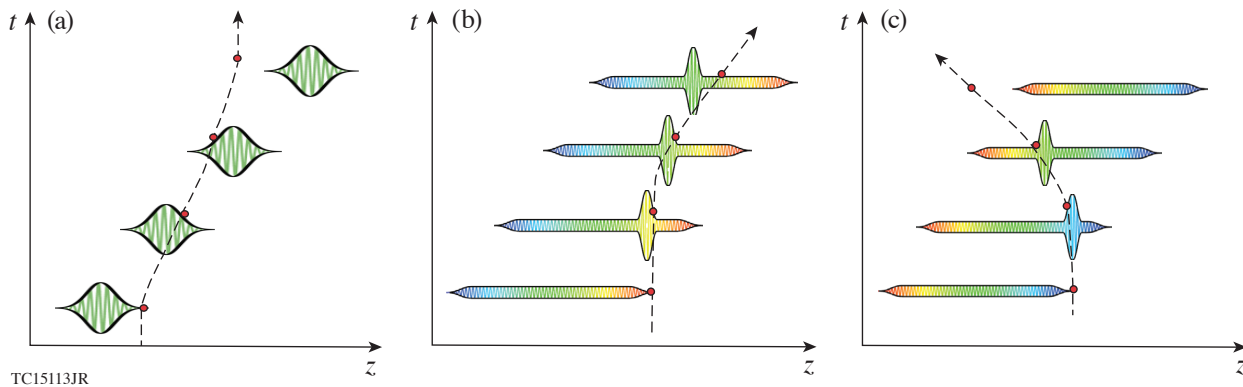


Figure 1

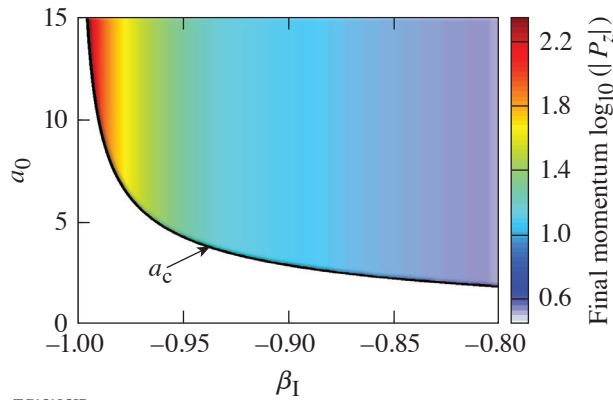
(a) A typical luminal intensity peak in vacuum. The electron, shown as a red dot, experiences equal and opposite ponderomotive accelerations on the leading and falling edges of the pulse, respectively, and gains no net energy. (b) A positively chirped flying focus with a subluminal intensity peak. After forward acceleration in the leading edge of the intensity peak, the electron outruns the peak and retains the energy it gained. (c) A negatively chirped flying focus with a subluminal intensity peak that travels in the opposite direction of the pulse. After backward acceleration in the leading edge, the electron outruns the intensity peak and retains the energy it gained.

We have demonstrated the first vacuum acceleration of electrons in a single planar-like laser pulse in either the forward or the backward direction. This novel mechanism for VLA utilizes the “flying focus”—a recently realized spatiotemporal pulse-shaping technique in which a chirped pulse focused by a hyperchromatic diffractive optic produces an intensity peak that can propagate at any velocity, including $|v_I| < c$, over distances much longer than the Rayleigh range.^{2,3} When the peak normalized vector potential

of the flying-focus pulse ($a_0 = eA_0/m_e c$) exceeds a critical value [$a_c = 2^{1/2} |\beta_I| \gamma_I$, where $\beta_I = v_I/c$ and $\gamma_I = (\beta_I^2)^{-1/2}$], it can accelerate electrons from rest to a final axial momentum that depends only on the velocity of the intensity peak: $p_f = 2m_e c \beta_I \gamma_I^2$. In principle, the spectral phase and power spectrum of a pulse can be adjusted to create an intensity peak with an arbitrary trajectory. Using this principle, we also show that matching the trajectory of an intensity peak to that of an electron enhances the momentum gain beyond $2m_e c \beta_I \gamma_I^2$.

Figures 1(b) and 1(c) illustrate the ponderomotive acceleration of an electron in either a subluminal forward or backward flying-focus intensity peak. In both cases, when $a_0 > a_c$, the electron can reach a velocity sufficient to outrun the intensity peak and retain its axial momentum, $2m_e c \beta_I \gamma_I^2$. The laser pulse propagates from left to right at the vacuum speed of light, while the flying-focus intensity peak moves independently at a velocity determined by the chirp and chromaticity of the diffractive optic (not shown). The chromatic aberration and chirp control the location and time at which each frequency comes to focus, respectively. Specifically, the intensity peak travels a distance $z_I = (\Delta\omega/\omega)f$ at a velocity $\beta_I = (1 \pm cT/z_I)^{-1}$, where ω is the central frequency of the pulse, $\Delta\omega/\omega$ is its fractional bandwidth, f is the focal length of the diffractive optic at ω , T is the stretched pulse duration, and \pm takes the sign of the chirp.

Figure 2 displays the final momentum as a function of the maximum vector potential and velocity of the intensity peak. The final momentum increases with the velocity of the intensity peak and diverges as $\beta_I \rightarrow 1$, but the required vector potential increases as well. Operating at the lowest-possible vector potential ($a_0 = a_c$) provides the scaling $|p_f| = m_e c a_0 (2 + a_0^2)^{1/2}$.



TC15105JR

Figure 2

Final momentum of an electron accelerated in a backward propagating flying focus intensity peak. Below the cutoff vector potential (a_c), an electron acquires a velocity insufficient to outrun the intensity peak. Above the cutoff, an accelerated electron can outrun the intensity peak, and the final momentum is independent of a_0 .

Accelerating the intensity peak to match the ponderomotive acceleration of an electron, i.e., “trajectory locking,” can substantially increase the momentum gain. Constant velocity intensity peaks limit the interaction distance and the momentum gain to a value determined by the maximum vector potential. By limiting the interaction distance, the constant velocity scheme wastes any length that the intensity peak has yet to travel. Trajectory locking, on the other hand, keeps the electron in the ponderomotive potential and can utilize the entire distance, z_I , to increase the final momentum.

In the trajectory-locked scheme, the intensity peak initially moves at a constant velocity, β_{I0} . Once the electron has accelerated from rest to the velocity of the intensity peak, which occurs at the location $a = a_c$, the intensity peak accelerates to keep the electron at this location (i.e., at $a = a_c$). In the trajectory locked peak, the cycle-averaged axial momentum of the electron evolves according to

$$\langle p_z(t > t_c) \rangle \approx m_e c \sqrt{(\beta_{I0} \gamma_{I0}^2)^2 + \frac{1}{2}(t - t_c) \frac{\partial a^2}{\partial z}} \Big|_{a=a_c}, \quad (1)$$

where $\beta_{10}\gamma_{10}^2$ is the cycle-averaged electron momentum upon reaching a_c at time t_c . Equation (1) predicts that optimizing the momentum gain requires co-locating a_c with the maximum intensity gradient of the peak. Asymptotically, the momentum gain has a relatively weak scaling with time, $\langle P_z \rangle \propto t^{1/2}$. This results from the diminished ponderomotive force as $\langle \gamma \rangle$ increases. Achieving a momentum gain greater than the constant velocity peak requires that the peak remains trajectory locked for a time $\Delta t > 2\tau a_c^{-2} \beta_{10}^3 \gamma_{10}^4$.

This material is based upon work supported by the Department of Energy National Nuclear Security Administration under Award Number DE-NA0003856, the University of Rochester, and the New York State Energy Research and Development Authority.

1. E. Esarey, P. Sprangle, and J. Krall, Phys. Rev. E **52**, 5443 (1995).
2. D. H. Froula *et al.*, Nat. Photonics **12**, 262 (2018).
3. J. P. Palastro *et al.*, Phys. Rev. A **97**, 033835 (2018).

Equation of State of CO₂ Shock Compressed to 1 TPa

L. E. Crandall,^{1,2} J. R. Rygg,^{1,2,3} D. K. Spaulding,⁴ T. R. Boehly,¹ S. Brygoo,⁵ P. M. Celliers,⁶ J. H. Eggert,⁶ D. E. Fratanduono,⁶ B. J. Henderson,^{1,2} M. F. Huff,^{1,2} R. Jeanloz,⁷ A. Lazicki,⁶ P. Loubeyre,⁵ M. C. Marshall,¹ D. N. Polsin,¹ M. Zaghoo,¹ M. Millot,⁶ and G. W. Collins^{1,2,3}

¹Laboratory for Laser Energetics, University of Rochester

²Department of Mechanical Engineering, University of Rochester

³Department of Physics and Astronomy, University of Rochester

⁴University of California, Davis

⁵Commissariat à l'énergie atomique et aux énergies alternatives

⁶Lawrence Livermore National Laboratory

⁷University of California, Berkeley

At terapascal pressures (10M atm), forces on atoms and molecules are comparable to their intrinsic quantum forces. Carbon dioxide is a simple molecular species with strong and stable chemical bonds at ambient conditions that exhibits complex phase transition behavior under increasing pressure and temperature. The physical, chemical, and thermodynamic behaviors of simple molecules comprising H, C, O, and N at hundreds of GPa and thousands of kelvin are vital to unraveling the dynamo, convective flow, and evolution of giant planets.^{1–3} Additionally, CO₂ is an important by-product of reacted chemical explosives, and its polarity, conductivity, and diffusivity at high pressure dictate the reactive dynamics of these explosives.^{4,5} The phase diagram of solid carbon dioxide has been extensively studied with heated diamond-anvil cells (DAC's) to 120 GPa (Refs. 6–11). This work demonstrates that the warm-dense-fluid regime of CO₂ is equally complex up to TPa pressures.

This work uses precompression and laser-driven shocks to explore the CO₂ equation of state (EOS) over a wide range of pressures and temperatures, extending to 1 TPa (10 Mbar) and 93,000 K (8 eV). CO₂ was precompressed to pressures up to 1.16 GPa in DAC's, attaining both liquid and solid initial states, and was then shock compressed. The temperature–pressure–density internal energy (T, P, ρ, E) EOS and optical reflectance (R) at 532 nm for these shocks were obtained with a velocity interferometer and an optical pyrometer. These data map a broad range of states from which thermodynamic derivatives were inferred, including the specific heat and the Grüneisen coefficient.

Combining these new data with previous results^{12–16} and theoretical calculations¹⁷ reveals a rich and complex phase diagram for CO₂. The shocked fluid exhibits at least three linear slopes in the shock velocity versus particle velocity plane; this may indicate three distinct phases or two phases with a transition region. Optical reflectivity measurements reveal an insulator-to-conductor transition between 100 and 200 GPa with a carrier density of roughly 0.3 electrons/atom. The observed trend in specific heat suggests a complex bonded fluid with increasing molecular degrees of freedom up to 1 TPa as opposed to an atomic fluid. We find that state-of-the-art modeling needs refinement to match the observed reflectivity and compressibility behavior of CO₂. High-pressure chemistry was once believed to be rather simple; this work reveals multiform behavior that is potentially quite general, as most of the known matter of the universe exists at high energy density ($P > 100$ GPa).

These shocked CO₂ experiments were performed at the Omega Laser Facility.¹⁸ CO₂ samples were precompressed to various initial pressures¹⁹ using DAC's^{20,21} to explore a family of Hugoniot. The velocity of the reflecting shock wave was measured throughout the shock transit of the entire experiment with a dual-channel velocity interferometer system for any reflector (VISAR).²²

A quartz or fused-silica pusher was used as a reference^{23–28} for impedance matching²⁹ at the pusher/CO₂ interface to determine the pressure and particle velocity of shocked CO₂. Density and internal energy were then determined from the Rankine–Hugoniot conservation relations. Compressibility data is plotted in Fig. 1(b). As initial density increases, the CO₂ Hugoniot becomes stiffer. Density-functional-theory (DFT) calculations³⁰ agree well with the initially 1.17-g/cm³ data [Fig. 1(b), blue circles, squares, and diamonds] (Refs. 12, 13, and 16), but the higher initial density CO₂ data [Fig. 1(b), green pentagons and triangles]¹⁴ exhibit less compressibility than that model predicts between 50 and 500 GPa. More-recent LEOS (Livermore equation of state) fits [dashed lines in Fig. 1(b)]³¹ match the OMEGA initial 1.4-g/cm³ and 1.7-g/cm³ data (green and red triangles), but they do not predict the increase in compressibility seen by Nellis *et al.* (blue squares)¹³ above 30 GPa.

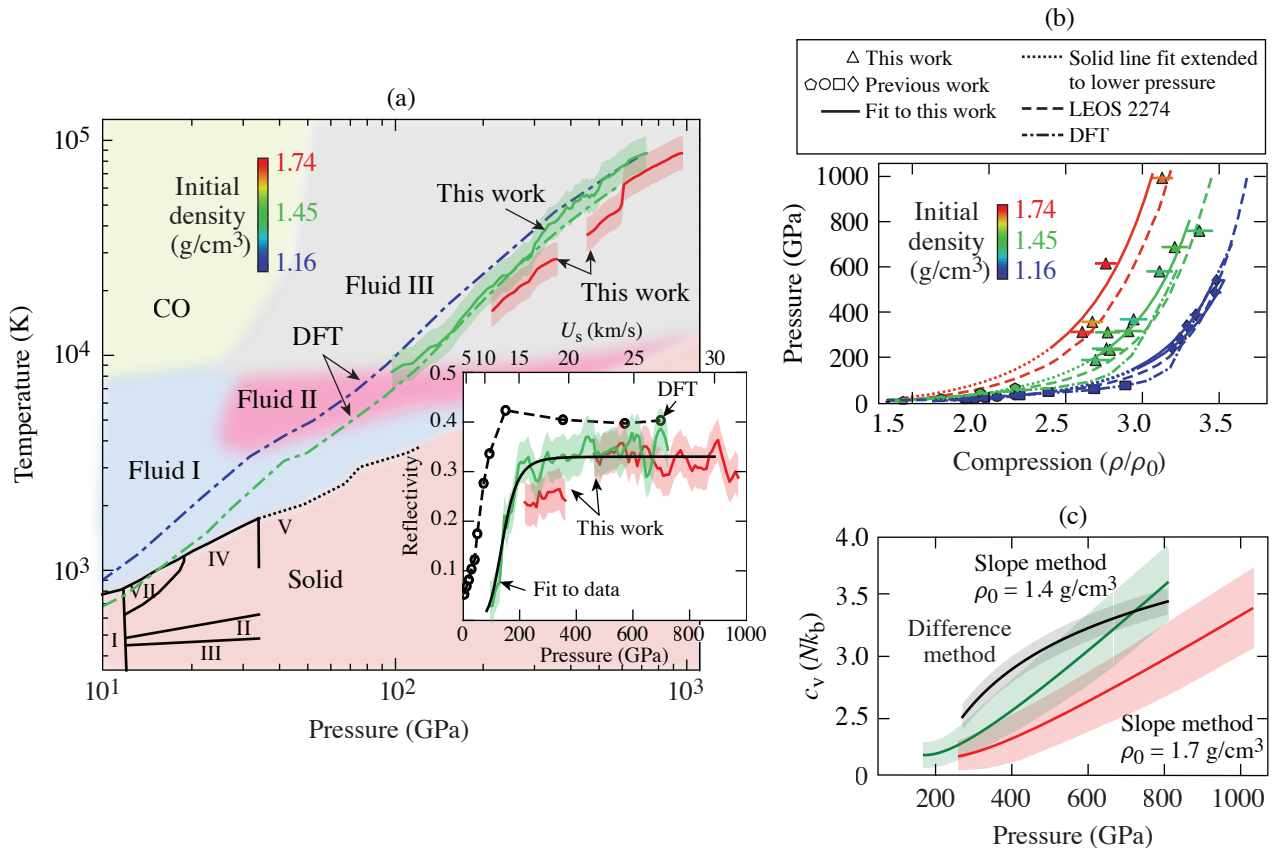


Figure 1

(a) Temperature versus pressure for shocked CO₂. Color of all data refers to initial density as given by the color bar. Inset: Reflectivity versus pressure. Saturated reflectivity implies a constant carrier density above 200 GPa. (b) Pressure versus compression, representing disagreement between the compression data and state-of-the-art models. (c) Specific heat versus pressure. The increasing trend implies increasing degrees of freedom with increasing pressure and temperature. Together, reflectivity and specific heat trends imply a moderately ionized and complex bonded state at extreme pressure.

The self-emission (590 to 850 nm) from the shock was measured using streaked optical pyrometry (SOP).³² The higher initial density Hugoniot is cooler than the lower initial density Hugoniot, and theoretical models³⁰ are consistent with our observed temperatures. The shock reflectivity at 532 nm [inset in Fig. 1(a)] is deduced from the VISAR amplitude and intensity as referenced to the known reflectivity of the quartz standard.^{25,33} The reflectivity rises steeply from a few percent at 100 GPa to saturation at 32% above 200 GPa, lower than the theory-predicted saturation of 40%. The steep rise is a result of the insulator-to-conductor transition driven by increasing pressure and temperature. Previous theoretical work predicted the onset of metallization to occur as low as 20 GPa (Ref. 34). We propose that metallization begins in Fluid-III, above 100 GPa on the Hugoniot. A multiphase fluid regime is constructed in Fig. 1(a) based on trends in the shock velocity of CO₂ in conjunction with theoretical calculations¹⁷ that predict a four-fluid system. The predicted boundaries of these fluids were adjusted to be consistent with the observed data.

Simultaneous temperature measurements allow one to calculate the isochoric specific heat [Fig. 1(c)]. The slope method³³ allows one to calculate the specific heat along the Hugoniot of initially liquid (1.4-g/cm³) and initially solid (1.7-g/cm³) CO₂. The specific heat steadily increases from 200 GPa to 1 TPa for both initially liquid and solid CO₂. The difference method, independent from the slope method, corroborates the trend of increasing specific heat. Increasing specific heat indicates increasing degrees of freedom (DOF's) in the fluid; because reflectivity is constant above 200 GPa, the increase in DOF's is not due to a rising carrier density. We conclude that the electrically conducting Fluid-III phase consists of a moderately ionized and bonded species of increasing chemical complexity, rather than a simple atomic fluid undergoing increasing ionization.

In summary, this work extends pressure and density measurements of the initially liquid and initially solid CO₂ Hugoniot to 1 TPa and provides the first temperature measurements of shocked CO₂ to 93,000 K. We propose a fluid phase diagram comprising at least three regimes to describe all existing shocked CO₂ data. Reflectivity and specific heat trends indicate that at pressures reaching 1 TPa, CO₂ is not likely a simple atomic fluid but instead a complex bonded and partially ionized species. Current models do not predict the observed compressibility and metallization behavior of high-pressure CO₂. This work demonstrates the rich behavior of nominally simple materials at high energy density and invites further inquiry into the chemistry of warm dense matter.

This material is based upon work supported by the Department of Energy National Nuclear Security Administration under Award Number DE-NA0003856, the University of Rochester, and the New York State Energy Research and Development Authority. A portion of this work was conducted at Lawrence Livermore National Laboratory under Contract Number DE-AC52-07NA27344.

1. T. Guillot, *Science* **286**, 72 (1999).
2. C. Cavazzoni *et al.*, *Science* **283**, 44 (1999).
3. S. Stanley and J. Bloxham, *Nature* **428**, 151 (2004).
4. M. van Thiel and F. H. Ree, *J. Appl. Phys.* **62**, 1761 (1987).
5. V. V. Chaban, E. E. Fileti, and O. V. Prezhdo, *J. Phys. Chem. Lett.* **6**, 913 (2015).
6. K. F. Dziubek *et al.*, *Nat. Commun.* **9**, 3148 (2018).
7. F. Datchi and G. Weck, *Z. Kristallogr.* **229**, 135 (2014).
8. C.-S. Yoo, *Phys. Chem. Chem. Phys.* **15**, 7949 (2013).
9. K. D. Litasov, A. F. Goncharov, and R. J. Hemley, *Earth Planet. Sci. Lett.* **309**, 318 (2011).
10. V. M. Giordano *et al.*, *J. Chem. Phys.* **133**, 144501 (2010).
11. V. M. Giordano, F. Datchi, and A. Dewaele, *J. Chem. Phys.* **125**, 054504 (2006).
12. G. L. Schott, *High Press. Res.* **6**, 187 (1991).
13. W. J. Nellis *et al.*, *J. Chem. Phys.* **95**, 5268 (1991).
14. V. N. Zubarev and G. S. Telegin, *Sov. Phys.-Dokl.* **7**, 34 (1962).
15. Zubarev and Telegin¹⁴ report two different initial densities for their solid CO₂: 1.45 and 1.54 g/cm³. Cited in Schott¹² are “verbal inquires and replies conveyed through C. L. Mader and A. N. Dremin, ca. 1983” that confirm that 1.54 g/cm³ is a misprint, and the initial density of the data published by Zubarev and Telegin is 1.45 g/cm³.
16. S. Root *et al.*, *Phys. Rev. B* **87**, 224102 (2013).
17. B. Boates, A. M. Toweldeberhan, and S. A. Bonev, *Proc. Natl. Acad. Sci.* **109**, 14808 (2012).

18. T. R. Boehly *et al.*, *Opt. Commun.* **133**, 495 (1997).
19. G. J. Piermarini *et al.*, *J. Appl. Phys.* **46**, 2774 (1975).
20. J. Eggert *et al.*, *Phys. Rev. Lett.* **100**, 124503 (2008).
21. P. M. Celliers *et al.*, *Phys. Rev. Lett.* **104**, 184503 (2010).
22. P. M. Celliers *et al.*, *Rev. Sci. Instrum.* **75**, 4916 (2004).
23. M. D. Knudson and M. P. Desjarlais, *Phys. Rev. B* **88**, 184107 (2013).
24. M. P. Desjarlais, M. D. Knudson, and K. R. Cochrane, *J. Appl. Phys.* **122**, 035903 (2017).
25. S. Brygoo *et al.*, *J. Appl. Phys.* **118**, 195901 (2015).
26. C. A. McCoy *et al.*, *J. Appl. Phys.* **119**, 215901 (2016).
27. C. Meade and R. Jeanloz, *Phys. Rev. B* **35**, 236 (1987).
28. R. G. Kraus *et al.*, *J. Geophys. Res. Planets* **117**, E09009 (2012).
29. Ya. B. Zel'dovich and Yu. P. Raizer, in *Physics of Shock Waves and High-Temperature Hydrodynamic Phenomena*, edited by W. D. Hayes and R. F. Probstein (Dover Publications, Mineola, NY, 2002).
30. B. Boates *et al.*, *J. Chem. Phys.* **134**, 064504 (2011).
31. C. J. Wu *et al.*, *J. Chem. Phys.* **151**, 224505 (2019).
32. J. E. Miller *et al.*, *Rev. Sci. Instrum.* **78**, 034903 (2007).
33. D. G. Hicks *et al.*, *Phys. Rev. Lett.* **97**, 025502 (2006).
34. C. Wang and P. Zhang, *J. Chem. Phys.* **133**, 134503 (2010).

Shock-Compressed Silicon: Hugoniot and Sound Speed to 2100 GPa

B. Henderson,^{1,2} M. C. Marshall,¹ T. R. Boehly,¹ R. Paul,^{1,3} C. McCoy,⁴ S. X. Hu,¹ D. N. Polsin,¹ L. E. Crandall^{1,2}
M. F. Huff,^{1,2} D. Chin,^{1,2} J. J. Ruby,^{1,2} X. Gong,^{1,3} D. E. Fratanduono,⁵ J. H. Eggert,⁵ J. R. Rygg,^{1,2,3} and G. W. Collins^{1,2,3}

¹Laboratory for Laser Energetics, University of Rochester

²Department of Physics & Astronomy, University of Rochester

³Department of Mechanical Engineering, University of Rochester

⁴Sandia National Laboratories

⁵Lawrence Livermore National Laboratory

The behavior of silicon (Si) above millions of atmospheres >100 GPa is important to understand the structure and evolution of terrestrial planets,^{1–4} as well as the performance of inertial confinement fusion (ICF) capsule designs.^{5–8} In rocky planets, Si is thought to be intrinsically paired to oxygen and, to a lesser extent, metals since they are prevalent on Earth's surface. However, it is likely that atomic bonding and compound formation are quite different at the extreme pressures expected in super-Earth-like planets.⁹ In direct-drive ICF target designs, materials are selected based on a variety of properties at pressures exceeding several TPa (Ref. 5). Si has been proposed as a dopant for plastic shells⁸ to mitigate laser imprint and Rayleigh–Taylor instabilities. While there has been significant work understanding the behavior of carbon^{10–13} at TPa pressures, very little is understood about its group-14 analog, Si, at these extreme conditions.

Principal Hugoniot and sound-speed data are presented for silicon shocked to 320 to 2100 GPa. These Hugoniot data exhibit a different u_s – u_p slope ($S = 1.26 \pm 0.06$) from the measurements of Ref. 14 ($S = 1.80 \pm 0.10$) at lower pressures (80 to 200 GPa). A change in Hugoniot slope can point to a significant structural change in the material, e.g., solid–solid phase transitions or melting,^{15,16} dissociation,¹⁷ or ionization.^{18,19} Quantum molecular dynamics (QMD) simulations performed at various points along silicon's principal Hugoniot predict an increase in ionic coordination and ionization of the $3s^2$ electron that is concurrent with the observed change in slope. Sound speeds were determined by time correlating the arrival of imposed acoustic perturbations at the shock front. The isentropic sound speed c_s of shock-compressed silicon was determined to be 15 to 23 km/s in the 5.7- to 7.6-g/cm³ density range.

Experiments were conducted on the OMEGA EP Laser System.²⁰ Targets were irradiated by one to four 351-nm laser beams directly onto a parylene-n (CH) ablator, producing strong shock waves that compress the planar samples. These experiments used laser intensities of 30 to 305 TW/cm² produced by 4- and 5-ns temporally square and ramp-top laser pulses with spot sizes of approximately 1100 or 1800 μ m. A portion of these experiments had preimposed acoustic perturbations on adjacent sides of the target stack, enabling a sound-speed determination.

The Hugoniot results are plotted in Fig. 1. Shock and particle velocity data from this work and four data points from Ref. 14 are fit separately using a weighted linear regression (method described in Ref. 21). This study is restricted to the high-pressure, single-wave regime, where shocked silicon does not form elastic and inelastic precursors; only Hugoniot data with pressure greater than 80 GPa are included in the fit. Functional forms were compared through a general linear F-test criterion, evaluated at the 1σ probability cutoff. An additional Bayesian statistical inference method was used for model selection, comparing a bilinear model against global linear and quadratic models through the Bayes factor. Accordingly, the bilinear model best represents silicon's

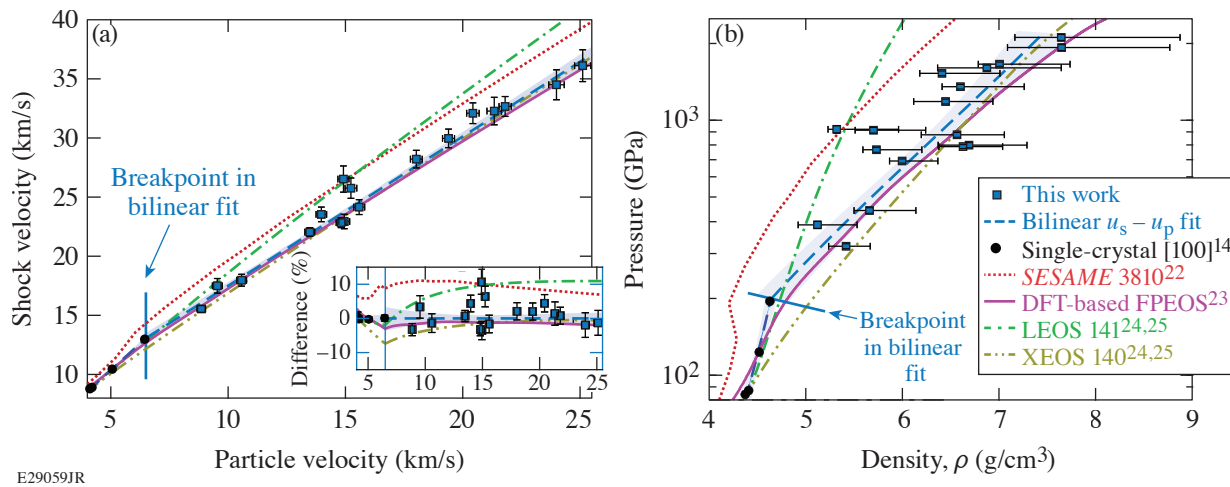


Figure 1

Silicon principal Hugoniot in (a) shock velocity u_s versus particle velocity u_p space and (b) pressure P versus density ρ space. Only dynamic compression data above 80 GPa, the single-wave compression regime in shocked silicon, are shown. Experimental data from this work (blue squares) and Ref. 14 (black circles) are fit with a bilinear functional form (dashed blue line) with a breakpoint at $u_p = 6.5$ km/s (solid blue line). A 1σ functional prediction band is shown as the shaded region surrounding the fit. Data is compared with Hugoniots from *SESAME* 3810 (red dotted curve),²² DFT-based FPEOS (pink curve),²³ LEOS 141 (dashed-dotted green curve) and XEOS 140 (dashed-dotted yellow curve).^{24,25} Inset in (a): Percent difference in shock velocity with respect to this work's u_s-u_p fit. FPEOS shows the best agreement with the experimental Hugoniot. The legend in (b) also corresponds to (a).

response to shock compression for shock pressures greater than 80 GPa. Using a χ^2 minimization, the breakpoint between the two linear regions was found at $u_{p,\text{break}} = 6.5$ km/s.

Theoretical calculations have played an important role in explaining observed changes in physical properties of high-energy-density materials.^{26–34} Changes in the Hugoniot slope are typically associated with ionic or electronic rearrangement. To better understand the physical mechanisms driving the change in Hugoniot slope for liquid silicon, density functional theory (DFT)-based QMD simulations were performed to examine changes in ionic coordination under shock compression. DFT-based QMD simulations suggest that the experimentally observed change in Hugoniot slope is coincident with an increase in ionic coordination and ionization of the $3s^2$ electron.

This material is based upon work supported by the Department of Energy National Nuclear Security Administration under Award Number DE-NA0003856, the University of Rochester, and the New York State Energy Research and Development Authority. A portion of this work was performed under the auspices of the U.S. Department of Energy by Lawrence Livermore National Laboratory under Contract No. DE-AC52-07NA27344 and Sandia National Laboratories under Contract No. DE-NA0003525.

1. E. J. Davies *et al.*, *J. Geophys. Res.: Planets* **125**, e2019JE006227 (2020).
2. J. E. Chambers, *Icarus* **152**, 205 (2001).
3. A. Benuzzi-Mounaix *et al.*, *Phys. Scr.* **2014**, 014060 (2014).
4. Y. Zhang *et al.*, *Geophys. Res. Lett.* **41**, 4554 (2014).
5. R. S. Craxton *et al.*, *Phys. Plasmas* **22**, 110501 (2015).
6. V. N. Goncharov *et al.*, *Phys. Plasmas* **21**, 056315 (2014).
7. G. Fiksel *et al.*, *Phys. Plasmas* **19**, 062704 (2012).

8. S. X. Hu *et al.*, Phys. Rev. Lett. **108**, 195003 (2012).
9. H. Niu *et al.*, Sci. Rep. **5**, 18347 (2015).
10. R. F. Smith *et al.*, Nature **511**, 330 (2014).
11. D. G. Hicks *et al.*, Phys. Rev. B **78**, 174102 (2008).
12. D. K. Bradley *et al.*, Phys. Rev. Lett. **93**, 195506 (2004).
13. M. C. Gregor *et al.*, Phys. Rev. B **95**, 144114 (2017).
14. M. N. Pavlovskii, Sov. Phys.-Solid State **9**, 2514 (1968).
15. O. Strickson and E. Artacho, Phys. Rev. B **93**, 094107 (2016).
16. R. Paul, S. X. Hu, and V. V. Karasiev, Phys. Rev. Lett. **122**, 125701 (2019).
17. W. J. Nellis *et al.*, J. Chem. Phys. **94**, 2244 (1991).
18. J. Eggert *et al.*, Phys. Rev. Lett. **100**, 124503 (2008).
19. R. F. Trunin, Phys.-Usp. **37**, 1123 (1994).
20. D. D. Meyerhofer *et al.*, J. Phys.: Conf. Ser. **244**, 032010 (2010).
21. P. M. Celliers *et al.*, J. Appl. Phys. **98**, 113529 (2005).
22. D. E. Fratanduono *et al.*, Phys. Rev. B **94**, 184107 (2016).
23. B. Boates *et al.*, J. Chem. Phys. **134**, 064504 (2011).
24. J. Zhang *et al.*, J. Appl. Phys. **114**, 173509 (2013).
25. Y. Zhang *et al.*, J. Chem. Phys. **135**, 064501 (2011).
26. Y. Zhang, C. Wang, and P. Zhang, Phys. Plasmas **19**, 112701 (2012).
27. S. Root *et al.*, Phys. Rev. B **87**, 224102 (2013).
28. R. J. Magyar, S. Root, and T. R. Mattsson, J. Phys.: Conf. Ser. **500**, 162004 (2014).
29. T. R. Mattsson *et al.*, Phys. Rev. B **90**, 184105 (2014).
30. D. Li, P. Zhang, and J. Yan, J. Chem. Phys. **139**, 134505 (2013).
31. G. I. Kerley, Kerley Publishing Services, Albuquerque, NM, Report KPS96-8 (September 1996).
32. S. X. Hu *et al.*, Phys. Rev. E **95**, 043210 (2017).
33. D. A. Young and E. M. Corey, J. Appl. Phys. **78**, 3748 (1995).
34. R. M. More *et al.*, Phys. Fluids **31**, 3059 (1988).

Thermal Effects on the Electronic Properties of Sodium Electride Under High Pressures

R. Paul,^{1,2} S. X. Hu,¹ V. V. Karasiev,¹ D. N. Polsin,¹ and S. A. Bonev³

¹Laboratory for Laser Energetics, University of Rochester

²Department of Mechanical Engineering, University of Rochester

³Lawrence Livermore National Laboratory

Despite being one of the simplest alkali metals at ambient pressure and temperature conditions, sodium exhibits a remarkably complex behavior under compression. The transition from lower-pressure metallic phases to the electride hP4 phase commences at approximately 160 GPa. This phase is structurally similar to a double hexagonal close-packed (dhcp) structure but has a higher compression along the c axis ($c/a = 1.391$) compared to the ideal dhcp ($c/a = 3.266$) at 320 GPa (Ref. 1). Due to the existence of a band gap, this phase has been described as a transparent insulator, deviating from the reflective metallic behavior observed at lower pressures. However, all diamond-anvil-cell (DAC) experiments performed on sodium at such pressures have been along the $T \approx 300$ K isotherm, while accompanying calculations were performed for static, nonthermalized crystals. To address the lack of systematic studies on the effects of thermal excitations on the electronic properties of electride sodium, we used density functional theory (DFT) to perform molecular dynamics (MD) and electro-optical calculations.

Canonical ensemble MD simulations were performed along different isochores while gradually increasing the ensemble temperature. This is termed as the “heat-until-melt” method, and the temperature regulation was attained using a Nosé–Hoover thermostat. The resulting melt curve for the tI19- and hP4-to-liquid transition demonstrates a monotonically increasing behavior as pressure increases, as can be seen in Fig. 1(a). Formerly, in order to establish the insulator nature of the phase, the orthonormalized single-particle Kohn–Sham orbitals Ψ_n^{KS} were used to construct the one-particle density operator, which in turn was used to create the real-space, one-particle density matrix $\rho(\mathbf{r}, \mathbf{r}') \sim \langle \exp(-\gamma|\mathbf{r} - \mathbf{r}'|) \rangle$. For normal insulators $\gamma \propto E^{1/2}$ and for semiconductors $\gamma \propto E$, where E is the band-gap energy.² Along the $\rho = 5.872\text{-g/cm}^3$ isochore, our analyses indicate that $\rho(\mathbf{r}, \mathbf{r}')$ varies with a band-gap exponent γ of 0.460, 0.438, 0.421, and 0.414 at $T = 300$ K, 700 K, 1200 K, and 1800 K, respectively. Therefore, the hP4 phase of sodium behaves like an insulator and not a semiconductor, when quantitatively analyzed using the *nearsightedness* of the density matrix as a criterion.

The band gaps obtained from the electronic density-of-state (DOS) calculations show a gradual decrease with increasing temperatures along the $\rho = 5.872\text{-g/cm}^3$ isochore until it abruptly decreases to zero upon melting, as shown in Fig. 1(b) for various exchange-correlation functionals. At $T = 300$ K, the calculated band gap was in the range of 1.54 eV (SCAN-L) to 1.84 eV Perdew–Burke–Ernzerhof (PBE), which corresponds to a photon wavelength of 673.83 nm (PBE) to 805.09 nm (SCAN-L). For wavelengths shorter than this threshold, hP4 sodium would exhibit reflectivity resembling that of an optical insulator.

Taking a closer look into the electronic charge distributions, it can be seen that one exceptional feature of high-pressure electrides is the localization of electrons in the interstices between ions, which leads to the formation of pockets with an electron localization function (ELF) value of near unity existing as pseudoanions. The hP4 phase of sodium exhibits such features, resulting in an insulating behavior owing to the band gap that develops from such an electronic distribution. This is true all the way up to the melt point, beyond which, using *a priori* knowledge from the band gap, one would expect these localization features to almost completely disappear and the system to transform into a near free electron (NFE)-type metallic liquid with $\text{ELF} \approx 0.5$. This is not seen to be the case, however, and even though the liquid phase is metallic, electron bubbles with paired localization exist in

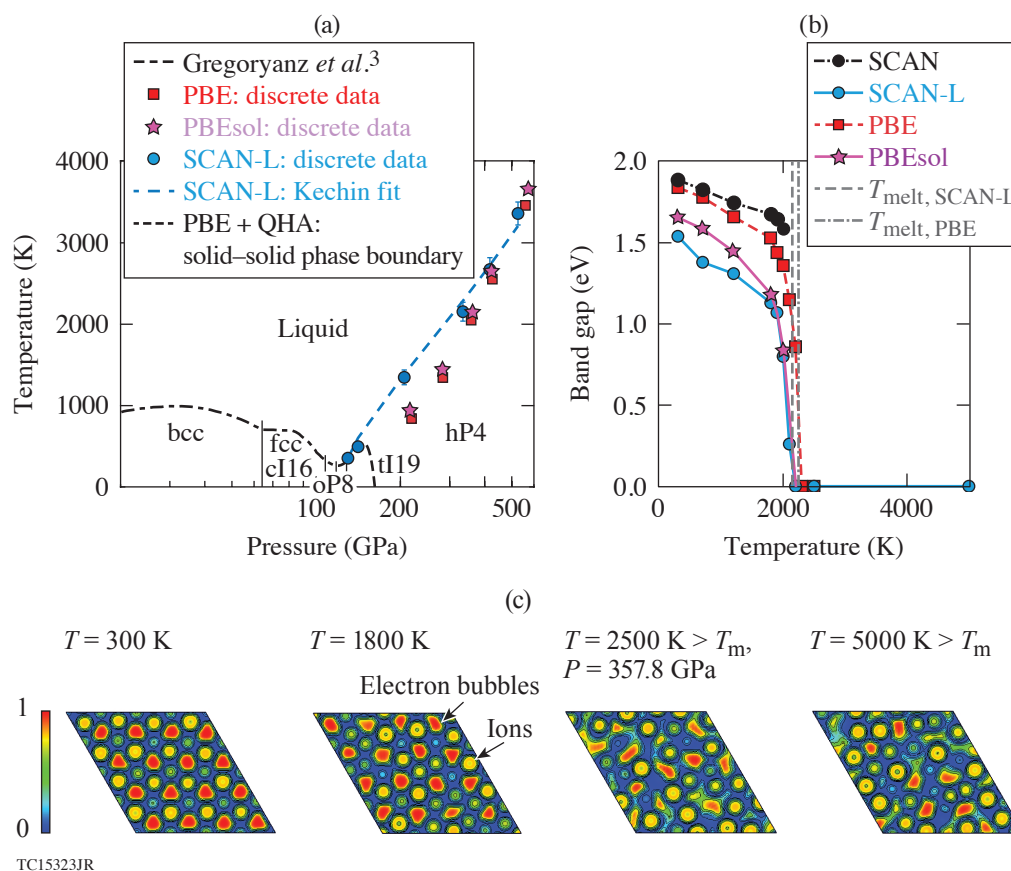


Figure 1

(a) The T - P phase diagram of sodium from literature³ combined with our work, with the existing melt curve data plotted. The tI19-hP4 phase boundary was constructed by comparing the Gibbs free energy computed by combining DFT and quasiharmonic approximated (QHA) phonon calculations. The uncertainty for the six isochoric melt data points, calculated using SCAN-L, are 20, 35, 90, 115, 145, and 140 K, respectively, calculated using five separate sets of MD calculations, with differing starting solid geometry, for each isochose. (b) The evolution of the band gap with temperature during heating along the $\rho = 5.872\text{-g/cm}^3$ isochose demonstrates the abrupt closing of the band gap on melting at $T_m \sim 2100$ to 2200 K, corresponding to an insulator-to-metal transition. Four sets of data corresponding to different exchange-correlation functionals: PBE, PBEsol, SCAN, and SCAN-L have been shown. (c) Planar static ELF on the (001) plane along the $\rho = 5.872\text{-g/cm}^3$ isochose, which shows the existence of paired interstitial electron bubbles (red) even beyond the melt point ($T_m \sim 2100$ to 2200 K).

tandem with a NFE distribution. The (001) planar ELF along the $\rho = 5.872\text{-g/cm}^3$ isochose clearly exhibits localized clusters of paired electrons, in the form of electron bubbles with $0.8 < \text{ELF} < 1.0$, that persist even beyond the melt point, as can be seen in Fig. 1(c). Rough estimation of the total number of electrons in certain pseudoanionic attractor regions yields a value of 1.91 to 2.0 in the solid phase and 1.77 to 1.94 in the liquid phase. This implies that the ELF attractors in the liquid phase are paired as well. Since planar cross-sectional representation of volumetric data can be misleading, we also calculated the all-volume, charge-weighted ELF histograms. Such an analysis also showed an abundant existence of regions with $\text{ELF} > 0.8$ in the liquid phase. However, increased temperatures along any isochose gradually dissipates these electron bubbles and the liquid ultimately reverts back to a NFE liquid beyond 5000 K.

Whereas in the solid state, interstitial electrons are predominantly p - d hybridized, two separate phenomena take place upon melting: (a) the thermal disorder in the ionic configuration in liquids, vis-à-vis solids, leads to delocalization of the p electrons from the p - d hybridized ELF attractors, alongside drastically increasing the s character and (b) delayed plasmon onset for the d electrons, compared to s and p electrons, due to higher effective mass caused by more localization. The combination of these

two effects reduces the contribution of the localized d electrons in the liquid-phase electron bubbles, despite being coalescent, to electro-optical properties and prevents such electrons from hybridizing. This also results in a change in hybridization from $p-d$ to $s-p$ upon melting. Electro-optical properties calculated using the Kubo–Greenwood formula also show this insulator-to-metal transition upon melting. In essence, the hP4 phase of sodium exhibits a decrease in band gap with thermalization, culminating in an insulator-to-metal transition upon melting, accompanied by the formation of residual electron bubbles and a change in electronic hybridization.

This material is based upon work supported by the Department of Energy National Nuclear Security Administration under Award Number DE-NA0003856, the University of Rochester, and the New York State Energy Research and Development Authority.

1. Y. Ma *et al.*, *Nature* **458**, 182 (2009).
2. S. Ismail-Beigi and T. A. Arias, *Phys. Rev. Lett.* **82**, 2127 (1999).
3. E. Gregoryanz *et al.*, *Phys. Rev. Lett.* **94**, 185502 (2005).

Optimization of a Short-Pulse-Driven Si He α Soft X-Ray Backlighter

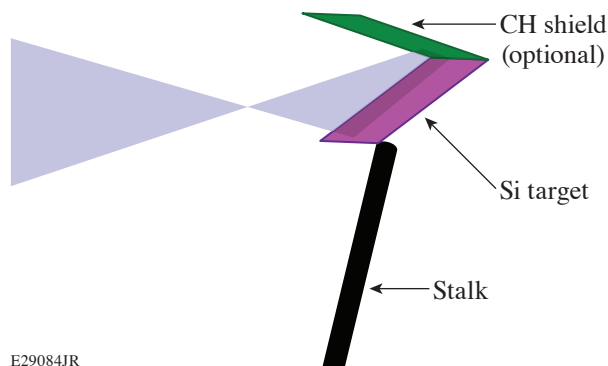
C. Stoeckl,¹ M. J. Bonino,¹ C. Mileham,¹ S. P. Regan,¹ W. Theobald,¹ T. Ebert,² and S. Sander²

¹Laboratory for Laser Energetics, University of Rochester

²Technical University of Darmstadt

Backlighting is a powerful method to interrogate the plasma density distribution in high-energy-density plasma experiments. A high backlighter brightness is not only important to maximize the photon-counting statistics, but it also helps to minimize the background from the self-emission of the plasma object. Backlighting high-performance layered cryogenic DT implosions¹ is especially challenging because of the strong self-emission from the hot core of the stagnated assembly and the low opacity of DT. This requires a soft x-ray backlighter with a photon energy of less than 2 keV, which is close to the maximum of the self-emission spectrum for cryogenic implosions on OMEGA.¹

A number of approaches are described in literature to increase the brightness of laser-driven x-ray backlighters. Some experiments have used low-density foams;^{2,3} others employed prepulses to increase the plasma density scale length.^{3,4} Some groups used V-shaped or cylindrical targets to create a cavity to absorb reflected laser light.^{3,5} These ideas were tested on the OMEGA EP laser⁶ at energies of the order of ~1 kJ and ~20-ps pulse length. Figure 1 shows the illumination geometry of the backlighter targets used for these experiments.



E29084JR

Figure 1
Illumination geometry for the backlighter targets.

An extensive suite of diagnostics was used to evaluate the improvements from each of these three approaches. The time-integrated x-ray emission spectrum from the backlighter target was measured using a flat crystal x-ray spectrometer.⁷ The temporal history of the x-ray emission from the backlighter targets was recorded using an ultrafast x-ray streak camera.⁸ To observe the effect of the different backlighter configurations on the number of photons that can be used for imaging, the shaped crystal imager (SCI) on OMEGA EP was run in the Si He α configuration⁹ for some of the backlighter tests. The best backlighter configuration was fielded on OMEGA to radiograph cryogenic DT implosions. In these experiments the data are recorded on a fast (~40-ps) time-gated x-ray framing camera.¹⁰

The data from the low-density (20-mg/cm³ and 100-mg/cm³) SiO₂ foam targets showed some changes in the shape of the hot K-shell spectrum but no significant increase in x-ray emission. In its optimum configuration (50 J of UV laser energy, 100-ps

pulse duration, 1 ns before the short pulse, 400- μ m distributed phase plate defocus) the prepulse experiment showed an $\sim 5\times$ improvement in time-integrated emission. However, time-resolved measurement showed a large tail in the x-ray emission lasting more than 300 ps, making this setup not suitable for the 40-ps, time-gated cryo backlighting application. The targets with the CH shield showed the best performance, with a 5 to $10\times$ improvement in time-integrated emission of the Si He α line compared to a simple solid target (see Fig. 2). The duration of ~ 25 ps for the main x-ray emission pulse was only marginally longer than the emission from the flat target (20 ps). In addition a low-level “afterglow” that lasted for a few 100 ps was observed. Tests with the time-integrated narrowband (~ 10 eV) SCI system showed an improvement consistent with the time-integrated spectral measurement. To evaluate the effect of the afterglow, one experiment was performed with the 40-ps time-gated SCI system, which as expected showed a small reduction of the benefit of the “shield” target to $\sim 6\times$ over a flat target.

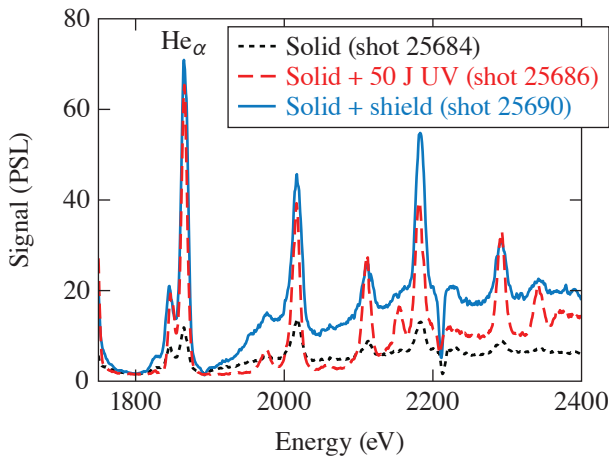


Figure 2
K-shell spectra from targets with and without shield compared to data from experiments with a 50-J UV prepulse.

To help guide future experiments, the conversion efficiency from laser light into Si He α photons was inferred from the time-integrated spectra and the time-integrated SCI measurements. Both instruments gave similar values of the order of 1×10^{-5} .

This material is based upon work supported by the Department of Energy National Nuclear Security Administration under Award Number DE-NA0003856, the University of Rochester, and the New York State Energy Research and Development Authority.

1. C. Stoeckl *et al.*, Phys. Plasmas **24**, 056304 (2017).
2. C. M. Huntington *et al.*, Rev. Sci. Instrum. **83**, 10E114 (2012).
3. F. Girard, Phys. Plasmas **23**, 040501 (2016).
4. M. Afshari *et al.*, Struct. Dynam. **7**, 014301 (2020).
5. H.-S. Park *et al.*, Phys. Plasmas **13**, 056309 (2006).
6. C. Stoeckl *et al.*, Fusion Sci. Technol. **49**, 367 (2006).
7. D. B. Thorn *et al.*, Rev. Sci. Instrum. **89**, 10F119 (2019).
8. C. Stoeckl *et al.*, Bull. Am. Phys. Soc. **52**, BAPS.2007.DPP.CO6.2 (2007).
9. C. Stoeckl *et al.*, Rev. Sci. Instrum. **83**, 033107 (2012); C. Stoeckl *et al.*, Rev. Sci. Instrum. **83**, 10E501 (2012).
10. C. Stoeckl *et al.*, Rev. Sci. Instrum. **85**, 11E501 (2014).

High-Resolution X-Ray Radiography with Fresnel Zone Plates on the OMEGA and OMEGA EP Laser Systems

F. J. Marshall,¹ S. T. Ivancic,¹ C. Mileham,¹ P. M. Nilson,¹ J. J. Ruby,¹ C. Stoeckl,¹ B. S. Scheiner,² and M. J. Schmitt²

¹Laboratory for Laser Energetics, University of Rochester

²Los Alamos National Laboratory

In this summary we report on the development of, along with the results from, the use of Fresnel zone plates (FZP's) to image x rays emitted by laser-generated plasmas on the OMEGA and OMEGA EP Laser Systems.^{1,2} An FZP manufactured by Applied Nanotools³ was used in this work. The FZP specifications are a 284.9 μm outer diameter, 512 zones, a 140-nm outermost zone width, and a resulting focal length of 151.86 mm for an energy of 4.750 keV (Ti He $_{\alpha}$ resonance line). The FZP zone bars consisted of 1.3- μm -thick Au bars on a 1.0- μm -thick Si $_3$ N $_4$ support membrane. For an example distance from object to image of $L = 3708.4$ mm, calculated values are then $p = 158.65$ mm, $q = 3549.75$ mm, and $M = 22.37$. At best focus, for a single-line energy, the FZP resolution is given by the diffraction limit $\delta = 1.22\Delta r_n$, where Δr_n is the width of the outermost zone.⁴ For the above example FZP, this implies a best single-line resolution of 171 nm. A range of possible resolutions is obtainable, limited not by the FZP, but by the detector. As an example, for a magnification of ~ 20 , the best obtainable resolution with a CCD (charge-coupled device) having 13.5- μm pixels is when the feature can be discerned by only two pixels (Nyquist limit), yielding a resolution limit of $\delta(\text{CCD}) \approx 27 \mu\text{m}/20 = 1.35 \mu\text{m}$. Other example detector resolutions of those used on OMEGA and OMEGA EP are $\delta(\text{film}) \approx 10$ to $20 \mu\text{m}$, $\delta(\text{image plate}) \approx 90 \mu\text{m}$, and $\delta(\text{framing camera}) \approx 50$ to $60 \mu\text{m}$. The higher the magnification, the better for these cases since all can severely compromise the resolution obtained at low magnification.

A resolution grid test was performed on the OMEGA EP target chamber using the same FZP assembly. The FZP was positioned to be focused on a grid placed at target chamber center, with a Ti foil 5 mm behind the grid. A pulsed OMEGA EP beam with 1 kJ of UV (351-nm) light in a 0.5-ns pulse was used to generate Ti He $_{\alpha}$ x rays. The magnification of the arrangement was $M = 22.37$, with $L = 3708.4$ mm, $p = 158.65$ mm, $q = 3549.8$ mm, and $f = 151.86$ mm, respectively, corresponding to the focus for Ti He $_{\alpha}$ x rays. The grid, which consisted of 6- μm -wide by 20- μm -thick Au bars, spaced by 25 μm , was covered by a 25- μm -thick Ta foil into which a 100- μm -diam aperture (mask) was laser cut. Figure 1(a) shows the grid image obtained with an SI800 CCD. A lineout through the image is shown in Fig. 1(b); Fig. 1(c) shows the line spread function (LSF) calculated by taking the derivative of the lineout. When averaging over eight edges, the width of the features implies an LSF full width at half maximum (FWHM) of $1.62 \pm 0.31 \mu\text{m}$. In this case the Nyquist limit is $27 \mu\text{m}/22.39 = 1.19 \mu\text{m}$, implying that the resolution obtained is partly detector limited and partly by spectral content, provided that the focus positioning was otherwise effectively perfect.

A series of experiments known as the *Revolver* experiments,⁵ whose principal investigators are the Los Alamos National Laboratory co-authors of this summary, were performed on the OMEGA target chamber. Fe backlighters were used to radiograph a set of concentric, double-shell implosions, where the outer shell was $\sim 1200 \mu\text{m}$ in diameter and the inner shell was $\sim 400 \mu\text{m}$ in diameter. The inner shell consisted of a 15- to 2- μm -thick Cr shell, held in place by a two-photon polymerization, 3-D-printed lattice with a volume-averaged density of 50 to 200 mg/cm 3 . The outer 25- μm -thick CH shell was driven by 40 beams with 11.4 kJ of UV light in a 1-ns pulse. Two backlighter foils were used per double-shell implosion. One foil backlit a pinhole array in front of a framing camera, and the other backlit the single FZP in front of a framing camera. The Fe-foil backlighters had principal line emission of the He-like line at 6.701 keV. Six beams were used to illuminate the pinhole-imaged framing camera backlighter and eight beams for the FZP-imaged framing camera backlighter. All backlighter beams were ~ 423 J/beam in a 1-ns pulse. Figure 2 shows a qualitative comparison between an Fe backlit image obtained with the pinhole arrays and an image

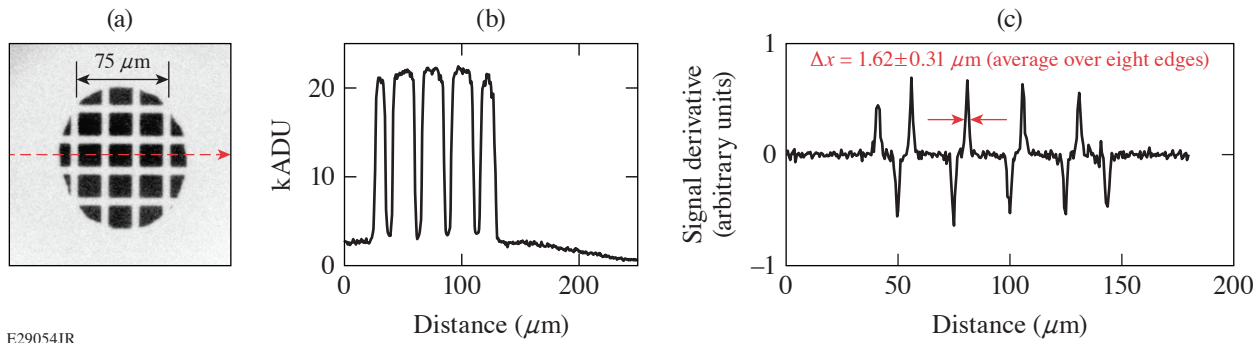


Figure 1

FZP image of a backlit grid obtained on OMEGA EP shot 30382 using a Ti-foil backlighter (4.75 keV). (a) CCD image of the grid with a 100- μm -diam mask over the grid; (b) lineout through the grid showing the grid bar shadows; (c) LSF (derivative) from which the resolution of $1.62 \pm 0.31 \mu\text{m}$ is inferred.

obtained with the FZP. The image from the FZP is shown in Fig. 2(a) and the pinhole image in Fig. 2(b) (both at $t = 4.5 \text{ ns}$). Whereas the expected resolution of the framed FZP image is ~ 3.3 to $4.0 \mu\text{m}$, the pinhole image was acquired with a $15\text{-}\mu\text{m}$ -diam pinhole d_{ph} at a magnification of 4. The two ten-inch-manipulator (TIM)-based framing cameras were nearly orthogonal to each other on the target chamber sphere, so only a qualitative comparison between the resolution of features is possible. The pinhole image was geometrically limited to a resolution of $(M + 1)d_{\text{ph}}/M = 18.75 \mu\text{m}$. The framing camera increases that to ~ 22.5 to $27.0 \mu\text{m}$ when taken in quadrature. Figure 2(c) shows the FZP image blurred to the approximate resolution of the pinhole image dramatically illustrating the loss of detail in the pinhole image as compared to the FZP image.

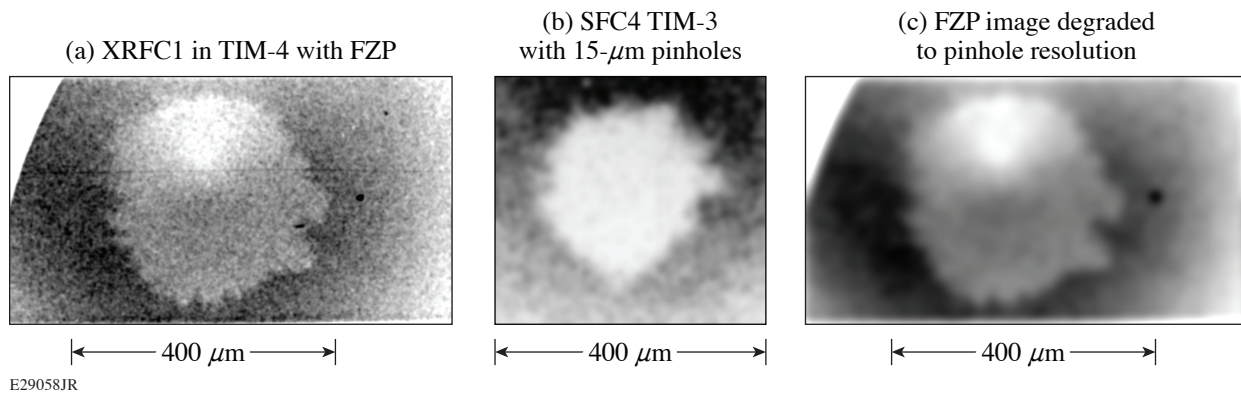


Figure 2

Comparison of a framed FZP image and pinhole image of a *Revolver* double-shell implosion on OMEGA, each backlit by Fe-foil emission (6.70 keV) at $t = 4.5 \text{ ns}$. (a) The FZP image, (b) the pinhole image, and (c) the FZP image blurred to the resolution of the pinhole image.

This material is based upon work supported by the Department of Energy National Nuclear Security Administration under Award Number DE-NA0003856, the University of Rochester, and the New York State Energy Research and Development Authority.

1. T. R. Boehly *et al.*, *Opt. Commun.* **133**, 495 (1997).
2. L. J. Waxer *et al.*, *Opt. Photonics News* **16**, 30 (2005).
3. Applied Nanotools Inc., NRC-NANO Building, Edmonton, Alberta T6G 2M9, Canada.
4. A. G. Michette, *Optical Systems for Soft X Rays* (Plenum Press, New York, 1986).
5. B. Scheiner *et al.*, *Phys. Plasmas* **26**, 072707 (2019).

Overcoming Gas Ionization Limitations with Divided-Pulse Nonlinear Compression

G. W. Jenkins, C. Feng, and J. Bromage

Laboratory for Laser Energetics, University of Rochester

Nonlinear compression in gas-filled hollow-core fiber (HCF) has been very successful for the spectral broadening and subsequent temporal compression of high-average-power Yb systems to ~ 10 -fs pulses. Pulse energy in an HCF is limited, however, by self-focusing and ionization.¹ In this summary, we examine the limits on HCF energy scaling and simulate a method to overcome those limits: divided-pulse nonlinear compression.

In HCF nonlinear compression, a glass cladding guides light within a gas-filled hollow core. The gas provides the nonlinearity to broaden the pulse's spectrum through self-phase modulation, and after the fiber, the pulse can be compressed to a shorter duration with devices such as chirped mirrors and prisms.² Self-focusing can be controlled by reducing the nonlinear index of the gas as the peak power of the pulse is increased.^{3,4} The gas pressure is a convenient variable to tune the nonlinear index and can be set to keep $>90\%$ of the power in the fundamental mode. Ionization is controlled with fiber diameter. At small diameters, the peak intensity is high enough to ionize gas and give rise to plasma effects. A small-diameter fiber is optimal for maximum spectral broadening, as long as plasma effects remain small.

To overcome ionization limits, we have simulated divided-pulse nonlinear compression (DPNLC), as depicted in Fig. 1(a). The intensity of the divided pulses will be lower than the intensity of the single pulse so smaller fibers can be used without ionizing the gas. We simulated a 10-mJ, 1-ps (FWHM) pulse centered at a 1030-nm wavelength, propagating through a 1.8-m, xenon-filled HCF with a model adapted from Horak and Poletti.⁵ We set the gas pressure to half the value given by Tempea and Brabec³ and varied the fiber radius to vary the strength of plasma effects.

Simulations with one pulse show significant energy loss from plasma effects, as shown in Fig. 1(b). Due to intrinsic fiber losses, some energy loss is unavoidable, and the ideal pulse would only lose energy to the intrinsic loss of the fundamental mode. The ideal energy is plotted as a black dotted line for reference. The output energy tracks the ideal energy line well for large fiber diameters, but with the onset of ionization around $550 \mu\text{m}$, there is a sharp loss of energy. Using two pulses shifts the onset of ionization to a diameter of around $400 \mu\text{m}$, and using four pulses shifts the onset to around $300 \mu\text{m}$. Figure 1(c) plots all loss channels for the two-pulse simulation and shows that energy losses are dominated by linear fiber losses and recombination losses. The linear fiber losses increase after the onset of ionization because the generated plasma defocuses the pulse.⁶ The HCF lacks total internal reflection, so it fails to confine the defocused pulse. Recombination losses increase because the trailing pulses pass through a gas-plasma mixture ionized by the first pulse and acquire phase artifacts from the index difference. Those phase artifacts appear as interference between the pulses when they are recombined and are removed by the polarizer. By shifting the onset of ionization to smaller fiber diameters, these losses can be avoided and the spectral broadening can be increased.

The ultimate figure of merit that demonstrates improvements from DPNLC is the peak power of the compressed pulse. We assumed we could compensate Kerr and plasma effects with up to second-order spectral phase during compression and plotted the peak power in Fig. 2. Because smaller-diameter fibers provide more spectral broadening, the general trend is that the smaller

fibers give a higher peak power as long as plasma effects are avoided. Plasma effects decrease the energy more than a small diameter and increase the bandwidth, so the peak power falls after the onset of ionization. DPNLC improves the optimum peak power achievable from 60 GW with one pulse to about 90 GW with four pulses.

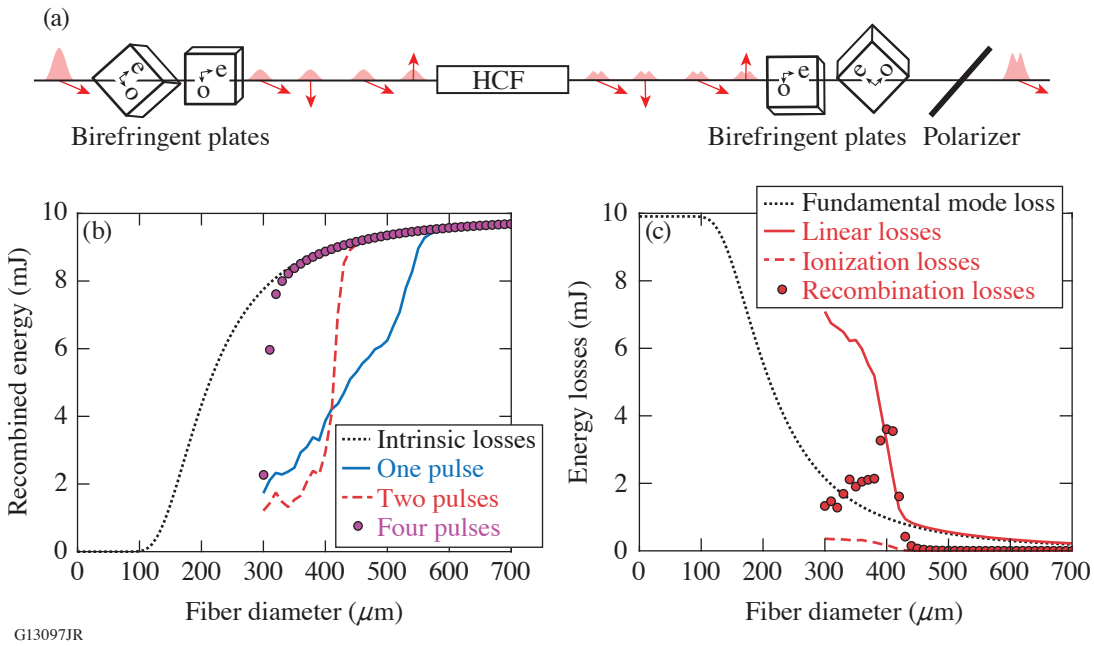


Figure 1

(a) Schematic of DPNLC with four pulses. Birefringent plates with extraordinary axis "e" and ordinary axis "o" can be used to separate the pulses temporally, and identical birefringent plates and a polarizer recombine the pulses. Red arrows indicate the pulse's polarization. (b) Simulated output energy after HCF and recombination for a range of fiber diameters. Onset of ionization is clearly visible and results in large energy losses. (c) Simulated energy losses for two divided pulses. The majority of energy loss is due to plasma-defocusing-induced linear and recombination losses.

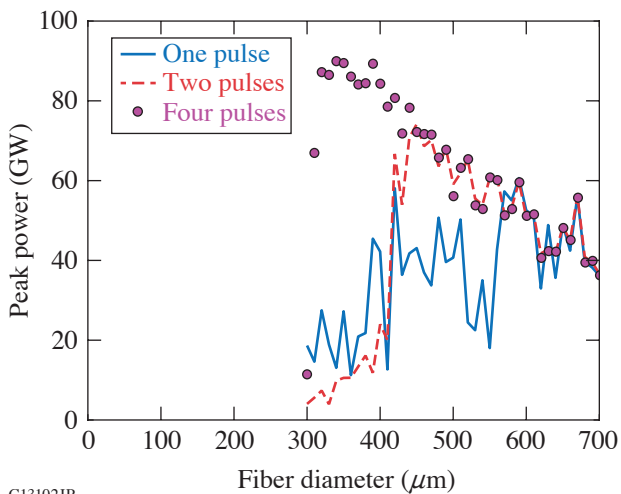


Figure 2

Peak power after recombination and compression with up to second-order spectral phase. Energy improvements from DPNLC give a significant improvement in peak power, with 60 GW achievable with one pulse improved to 90 GW with four pulses.

This material is based upon work supported by the Department of Energy National Nuclear Security Administration under Award Number DE-NA0003856, the University of Rochester, and the New York State Energy Research and Development Authority.

1. C. Vozzi *et al.*, *Appl. Phys. B* **80**, 285 (2005).
2. M. Nisoli *et al.*, *Appl. Phys. B* **65**, 189 (1997).
3. G. Tempea and T. Brabec, *Opt. Lett.* **23**, 762 (1998).
4. N. Milosevic, G. Tempea, and T. Brabec, *Opt. Lett.* **25**, 672 (2000).
5. P. Horak and F. Poletti, in *Recent Progress in Optical Fiber Research*, edited by M. Yasin (InTechOpen, Rijeka, Croatia, 2012), Chap. 1, pp. 3–24.
6. A. Couairon and A. Mysyrowicz, *Phys. Rep.* **441**, 47 (2007).

FY20 Q3 Laser Facility Report

J. Puth, M. Labuzeta, D. Canning, and R. T. Janezic

Laboratory for Laser Energetics, University of Rochester

During the third quarter of FY20, the Omega Laser Facility was in safe stand-down for eight weeks, with additional weeks of recovery activities due to the COVID-19 pandemic and associated state regulations. During the remaining weeks of the quarter, the facility conducted 89 target shots on OMEGA and 69 target shots on OMEGA EP for a total of 158 target shots (see Tables I and II). OMEGA averaged 9.3 target shots per operating day, averaging 84.9% Availability and 99.4% Experimental Effectiveness. OMEGA EP averaged 8.3 target shots per operating day, averaging 92.5% Availability and 99.2% Experimental Effectiveness.

During this quarter, the system was fitted with additional computer resources and audio/video equipment to facilitate remote principal investigator collaboration with the shot crew, enabling experiments to proceed during social distancing. The Control Rooms were rearranged to maximize operator separation, and protocol was enhanced to minimize the passing of paper and equipment. At this time, LLE continues to operate with a decreased personnel density by maximizing work from home.

Table I: OMEGA Laser System target shot summary for Q3 FY20.

Program	Laboratory	Planned Number of Target Shots	Actual Number of Target Shots
ICF	LLE	38.5	36
ICF Subtotal		38.5	36
HED	LLE	11	13
	LLNL	22	23
HED Subtotal		33	36
NLUF		11	14
Calibration	LLE	0	3
Grand Total		82.5	89

Table II: OMEGA EP Laser System target shot summary for Q3 FY20.

Program	Laboratory	Planned Number of Target Shots	Actual Number of Target Shots
ICF	LLNL	7	7
ICF Subtotal		7	7
HED	LLE	7	9
	LANL	7	6
	LLNL	7	6
HED Subtotal		21	21
AIBS		7	12
LaserNetUS		7	11
Calibration	LLE	0	16
Grand Total		42	67

Publications and Conference Presentations

Publications

- Y. Arikawa, M. Ota, M. Nakajima, T. Shimizu, S. Segawa, T. N. K. Phan, Y. Sakawa, Y. Abe, A. Morace, S. R. Mirfayzi, A. Yogo, S. Fujioka, M. Nakai, H. Shiraga, H. Azechi, R. Kodama, K. Kan, J. Frenje, M. Gatu Johnson, A. Bose, N. V. Kabadi, G. D. Sutcliffe, P. Adrian, C. Li, F. H. Séguin, and R. Petrasso, “The Conceptual Design of 1-ps Time Resolution Neutron Detector for Fusion Reaction History Measurement at OMEGA and the National Ignition Facility,” *Rev. Sci. Instrum.* **91**, 063304 (2020).
- S. H. Cao, R. Yan, H. Wen, J. Li, and C. Ren, “Cogeneration of Hot Electrons from Multiple Laser-Plasma Instabilities,” *Phys. Rev. E* **101**, 053205 (2020).
- L. Ceurvorst, R. Betti, A. Casner, V. Gopalaswamy, A. Bose, S. X. Hu, E. M. Campbell, S. P. Regan, C. A. McCoy, M. Karasik, J. L. Peebles, M. Tabak, and W. Theobald, “Hybrid Target Design for Imprint Mitigation in Direct-Drive Inertial Confinement Fusion,” *Phys. Rev. E* **101**, 063207 (2020).
- L. E. Chen, A. F. A. Bott, P. Tzeferacos, A. Rigby, A. Bell, R. Bingham, C. Graziani, J. Katz, M. Koenig, C. K. Li, R. Petrasso, H.-S. Park, J. S. Ross, D. Ryu, T. G. White, B. Reville, J. Matthews, J. Meinecke, F. Miniati, E. G. Zweibel, S. Sarkar, A. A. Schekochihin, D. Q. Lamb, D. H. Froula, and G. Gregori, “Transport of High-Energy Charged Particles Through Spatially Intermittent Turbulent Magnetic Fields,” *Astrophys. J.* **892**, 114 (2020).
- A. R. Christopherson, R. Betti, S. Miller, V. Gopalaswamy, O. M. Mannion, and D. Cao, “Theory of Ignition and Burn Propagation in Inertial Fusion Implosions,” *Phys. Plasmas* **27**, 052708 (2020).
- D. J. Erskine, “Forward Modeling of Doppler Velocity Interferometer System for Improved Shockwave Measurements,” *Rev. Sci. Instrum.* **91**, 043103 (2020).
- C. Fagan, M. Sharpe, W. T. Shmayda, and W. U. Schröder, “A Thin Alumina Film as a Tritium Adsorption Inhibitor for Stainless Steel 316,” *Fusion Sci. Technol.* **76**, 424 (2020).
- K. Falk, C. J. Fontes, C. L. Fryer, C. W. Greeff, M. Holec, H. M. Johns, D. S. Montgomery, D. W. Schmidt, and M. M. Šmíd, “Experimental Observation of Elevated Heating in Dynamically Compressed CH Foam,” *Plasma Phys. Control. Fusion* **62**, 074001 (2020).
- F. Fiuza, G. F. Swadling, A. Grassi, H. G. Rinderknecht, D. P. Higginson, D. D. Ryutov, C. Bruulsema, R. P. Drake, S. Funk, S. Glenzer, G. Gregori, C. K. Li, B. B. Pollock, B. A. Remington, J. S. Ross, W. Rozmus, Y. Sakawa, A. Spitkovsky, S. Wilks, and H.-S. Park, “Electron Acceleration in Laboratory-Produced Turbulent Collisionless Shocks,” *Nat. Phys.* **16**, 916 (2020).
- R. K. Follett, J. G. Shaw, J. F. Myatt, D. H. Froula, and J. P. Palastro, “Multibeam Absolute Stimulated Raman Scattering and Two-Plasmon Decay,” *Phys. Rev. E* **101**, 043214 (2020).
- Y. Frank, G. E. Kemp, E. V. Marley, G. P. Callejo, M. E. Foord, M. B. Schneider, Y. Ehrlich, and M. Fraenkel, “Hydrodynamic Conditions in Laser Irradiated Buried Layer Experiments,” *Phys. Plasmas* **27**, 063301 (2020).
- B. M. Haines, D. E. Keller, J. A. Marozas, P. W. McKenty, K. S. Anderson, T. J. B. Collins, W. W. Dai, M. L. Hall, S. Jones, M. D. McKay Jr., R. M. Rauenzahn, and D. N. Woods, “Coupling Laser Physics to Radiation-Hydrodynamics,” *Comput. Fluids* **201**, 104478 (2020).
- E. C. Hansen, J. R. Davies, D. H. Barnak, R. Betti, E. M. Campbell, V. Yu. Glebov, J. P. Knauer, L. S. Leal, J. L. Peebles, A. B. Sefkow, and K. M. Woo, “Neutron Yield Enhancement and Suppression by Magnetization in Laser-Driven Cylindrical Implosions,” *Phys. Plasmas* **27**, 062703 (2020) (invited).
- S. X. Hu, V. V. Karasiev, V. Recoules, P. M. Nilson, N. Brouwer, and M. Torrent, “Interspecies Radiative Transition in Warm and Superdense Plasma Mixtures,” *Nat. Commun.* **11**, 1989 (2020).

- A. Kar, S. X. Hu, G. Duchateau, J. Carroll-Nellenback, and P. B. Radha, "Implementing a Microphysics Model in Hydrodynamic Simulations to Study the Initial Plasma Formation in Dielectric Ablator Materials for Direct-Drive Implosions," *Phys. Rev. E* **101**, 063202 (2020).
- P. R. C. Kent, A. Annaberdiyev, A. Benali, M. C. Bennett, E. J. L. Borda, P. Doak, H. Hao, K. D. Jordan, J. T. Krogel, I. Kylänpää, J. Lee, Y. Luo, F. D. Malone, C. A. Melton, L. Mitas, M. A. Morales, E. Neuscammann, F. A. Reboledo, B. Rubenstein, K. Saritas, S. Upadhyay, G. Wang, S. Zhang, and L. Zhao, "QMCPACK: Advances in the Development, Efficiency, and Application of Auxiliary Field and Real-Space Variational and Diffusion Quantum Monte Carlo," *J. Chem. Phys.* **152**, 174105 (2020).
- B. Lahmann, M. Gatu Johnson, J. A. Frenje, V. Yu. Glebov, H. G. Rinderknecht, F. H. Séguin, G. Sutcliffe, and R. D. Petrasso, "CR39 Nuclear Track Detector Response to Inertial Confinement Fusion Relevant Ions," *Rev. Sci. Instrum.* **91**, 053502 (2020).
- O. M. Mannion, J. P. Knauer, V. Yu. Glebov, C. J. Forrest, A. Liu, Z. L. Mohamed, M. H. Romanofsky, T. C. Sangster, C. Stoeckl, and S. P. Regan, "A Suite of Neutron Time-of-Flight Detectors to Measure Hot-Spot Motion in Direct-Drive Inertial Confinement Fusion Experiments on OMEGA," *Nucl. Instrum. Methods Phys. Res. A* **964**, 163774 (2020).
- D. I. Mihaylov, V. V. Karasiev, and S. X. Hu, "Thermal Hybrid Exchange-Correlation Density Functional for Improving the Description of Warm Dense Matter," *Phys. Rev. B* **101**, 245141 (2020).
- J. L. Peebles, J. R. Davies, D. H. Barnak, T. Cracium, M. J. Bonino, and R. Betti, "Axial Proton Probing of Magnetic and Electric Fields Inside Laser-Driven Coils," *Phys. Plasmas* **27**, 063109 (2020).
- H. G. Rinderknecht, D. T. Casey, R. Hatarik, R. M. Bionta, B. J. MacGowan, P. Patel, O. L. Landen, E. P. Hartouni, and O. A. Hurricane, "Azimuthal Drive Asymmetry in Inertial Confinement Fusion Implosions on the National Ignition Facility," *Phys. Rev. Lett.* **124**, 145002 (2020).
- M. J. Rosenberg, A. A. Solodov, W. Seka, R. K. Follett, J. F. Myatt, A. V. Maximov, C. Ren, S. Cao, P. Michel, M. Hohenberger, J. P. Palastro, C. Goyon, T. Chapman, J. E. Ralph, J. D. Moody, R. H. H. Scott, K. Glize, and S. P. Regan, "Stimulated Raman Scattering Mechanisms and Scaling Behavior in Planar Direct-Drive Experiments at the National Ignition Facility," *Phys. Plasmas* **27**, 042705 (2020).
- J. R. Rygg, R. F. Smith, A. E. Lazicki, D. G. Braun, D. E. Fratanduono, R. G. Kraus, J. M. McNaney, D. C. Swift, C. E. Wehrenberg, F. Coppari, M. F. Ahmed, M. A. Barrios, K. J. M. Blobaum, G. W. Collins, A. L. Cook, P. Di Nicola, E. G. Dzenitis, S. Gonzales, B. F. Heidl, M. Hohenberger, A. House, N. Izumi, D. H. Kalantar, S. F. Khan, T. R. Kohut, C. Kumar, N. D. Masters, D. N. Polsin, S. P. Regan, C. A. Smith, R. M. Vignes, M. A. Wall, J. Ward, J. S. Wark, T. L. Zobrist, A. Arsenlis, and J. H. Eggert, "X-Ray Diffraction at the National Ignition Facility," *Rev. Sci. Instrum.* **91**, 043902 (2020).
- R. W. Short, "Absolute Stimulated Raman Side Scatter in Direct-Drive Laser-Produced Plasmas," *Phys. Plasmas* **27**, 042703 (2020).
- A. A. Solodov, M. J. Rosenberg, W. Seka, J. F. Myatt, M. Hohenberger, R. Epstein, C. Stoeckl, R. W. Short, S. P. Regan, P. Michel, T. Chapman, R. K. Follett, J. P. Palastro, D. H. Froula, P. B. Radha, J. D. Moody, and V. N. Goncharov, "Hot-Electron Generation at Direct-Drive Ignition-Relevant Plasma Conditions at the National Ignition Facility," *Phys. Plasmas* **27**, 052706 (2020).
- R. B. Spielman and A. B. Sefkow, "Modeling Variable-Impedance, Magnetically Insulated, Transmission Lines," in *2019 IEEE Pulsed Power & Plasma Science (PPPS)* (IEEE, Piscataway, NJ, 2020).
- G. F. Swadling, C. Bruulsema, F. Fiuza, D. P. Higginson, C. M. Huntington, H. S. Park, B. B. Pollock, W. Rozmus, H. G. Rinderknecht, J. Katz, A. Birkel, and J. S. Ross, "Measurement of Kinetic-Scale Current Filamentation Dynamics and Associated Magnetic Fields in Interpenetrating Plasmas," *Phys. Rev. Lett.* **124**, 215001 (2020).
- D. Turnbull, A. V. Maximov, D. H. Edgell, W. Seka, R. K. Follett, J. P. Palastro, D. Cao, V. N. Goncharov, C. Stoeckl, and D. H. Froula, "Anomalous Absorption by the Two-Plasmon Decay Instability," *Phys. Rev. Lett.* **124**, 185001 (2020).
- T. Walton, J. L. Sebold, I. E. Golovkin, J. J. MacFarlane, V. N. Golovkina, A. A. Solodov, P. M. Nilson, and R. Epstein, "Parameterizing Hot Electron Energy Distributions for Tabular Emissivities and Opacities," *High Energy Density Phys.* **35**, 100730 (2020).
- K. M. Woo, R. Betti, O. M. Mannion, C. J. Forrest, J. P. Knauer, V. N. Goncharov, P. B. Radha, V. Gopalaswamy, and V. Yu. Glebov, "Inferring Thermal Ion Temperature and Residual

Kinetic Energy from Nuclear Measurements in Inertial Confinement Fusion Implosions,” *Phys. Plasmas* **27**, 062702 (2020) (invited).

J. Zhang, R. Wei, M. ElKabbash, E. M. Campbell, and C. Guo, “Thin-Film Perfect Infrared Absorbers over Single- and Dual-Band Atmospheric Windows,” *Opt. Lett.* **45**, 2800 (2020).

Y. Zhao and W. R. Donaldson, “Ultrafast UV AlGaIn Metal–Semiconductor–Metal Photodetector with a Response Time Below 25 ps,” *IEEE J. Quantum Electron.* **56**, 4000607 (2020).

A. B. Zylstra, H. W. Herrmann, Y. H. Kim, A. McEvoy, J. A. Frenje, M. Gatu Johnson, R. D. Petrasso, V. Yu. Glebov, C. Forrest, J. Delettrez, S. Gales, and M. Rubery, “ $^2\text{H}(p,\gamma)^3\text{He}$ Cross Section Measurement Using High-Energy-Density Plasmas,” *Phys. Rev. C* **101**, 042802(R) (2020).

A. B. Zylstra, J. R. Rygg, G. W. Collins, C. K. Li, J. A. Frenje, R. D. Petrasso, S. R. Nagel, P. Fitzsimmons, and H. Reynolds, “Platform Development for dE/dx Measurements on Short-Pulse Laser Facilities,” *High Energy Density Phys.* **35**, 100731 (2020).

Forthcoming Publications

K. L. Baker, C. A. Thomas, D. T. Casey, M. Hohenberger, S. Khan, B. K. Spears, O. L. Landen, R. Nora, D. T. Woods, J. L. Milovich, R. L. Berger, D. Strozzi, C. Weber, D. Clark, O. A. Hurricane, D. A. Callahan, A. L. Kritcher, B. Bachmann, L. R. Benedetti, R. Bionta, P. M. Celliers, D. Fittinghoff, C. Goyon, R. Hatarik, N. Izumi, M. Gatu Johnson, G. Kyrala, T. Ma, K. Meaney, M. Millot, S. R. Nagel, P. K. Patel, D. Turnbull, P. L. Volegov, C. Yeaman, and C. Wilde, “Hot-Spot Parameter Scaling with Velocity and Yield for High-Adiabatic Layered Implosions at the National Ignition Facility,” to be published in *Physical Review E*.

D. H. Barnak, J. R. Davies, J. P. Knauer, and P. M. Kozlowski, “Soft X-Ray Spectrum Unfold of K-Edge–Filtered X-Ray Diode Arrays Using Cubic Splines,” to be published in *Review of Scientific Instruments*.

K. A. Bauer, M. Heimbueger, J. Kwiatkowski, S. Sampat, L. J. Waxer, E. C. Cost, J. H. Kelly, V. Kobilansky, S. F. B. Morse, D. Nelson, D. Weiner, G. Weselak, and J. Zou, “Optical Characterization of the On-Target OMEGA Focal Spot at High Energy Using the Full-Beam In-Tank Diagnostic,” to be published in *Applied Optics*.

P. T. Campbell, C. A. Walsh, B. K. Russell, J. P. Chittenden, A. Crilly, G. Fiksel, P. M. Nilson, A. G. R. Thomas, K. Krushelnick, and L. Willingale, “Magnetic Signatures of Radiation-Driven Double Ablation Fronts,” to be published in *Physical Review Letters*.

Y.-H. Chen, J. R. Peterson, L. A. Johnson, T. G. Jones, B. Hafizi, A. B. Stamm, A. C. Ting, J. P. Palastro, M. H. Helle, and D. Kaganovich, “Nonlinear Underwater Propagation of Pico-second Ultraviolet Laser Beams,” to be published in *Optic Letters*.

L. E. Crandall, J. R. Rygg, D. Spaulding, T. R. Boehly, S. Brygoo, P. M. Celliers, J. H. Eggert, D. E. Fratanduono, B. J. Henderson, M. F. Huff, R. Jeanloz, A. Lazicki, M. C. Marshall, D. N. Polsin, M. Zaghoo, M. Millot, and G. W. Collins, “Equation of State of CO_2 Shock Compressed to 1 TPa,” to be published in *Physical Review Letters*.

W. A. Farmer, C. Bruulsema, G. F. Swadling, M. W. Sherlock, M. D. Rosen, W. Rozmus, D. H. Edgell, J. Katz, B. B. Pollock, and J. S. Ross, “Validation of Heat Transport Modeling Using Directly Driven Beryllium Spheres,” to be published in *Physics of Plasmas*.

M. Gatu Johnson, B. M. Haines, P. J. Adrian, C. Forrest, J. A. Frenje, V. Yu. Glebov, W. Grimble, R. Janezic, J. P. Knauer, B. Lahmann, F. J. Marshall, T. Michel, F. H. Séguin, C. Stoeckl, and R. D. Petrasso “3-D $xRAGE$ Simulation of Inertial Confinement Fusion Implosion with Imposed Mode-2 Laser Drive Asymmetry,” to be published in *High Energy Density Physics*.

V. N. Goncharov, I. V. Igumenshchev, D. R. Harding, S. F. B. Morse, S. X. Hu, P. B. Radha, D. H. Froula, S. P. Regan, T. C. Sangster, and E. M. Campbell, “Novel Hot-Spot Ignition Designs for Inertial Confinement Fusion with Liquid Deuterium–Tritium Spheres,” to be published in *Physical Review Letters*.

D. R. Harding, M. D. Wittman, N. P. Redden, D. H. Edgell, and J. Ulreich, “Comparison of Shadowgraphy and X-Ray Phase Contrast Methods for Characterizing a DT Ice Layer in an Inertial Confinement Fusion Target,” to be published in *Fusion Science and Technology*.

A. J. Harvey-Thompson, M. R. Weis, D. E. Ruiz, M. S. Wei, A. Sefkow, T. Nagayama, E. M. Campbell, J. Fooks, M. Glinsky, and K. J. Peterson, “The Effect of Laser Entrance Hole Foil Thickness on MagLIF-Relevant Laser Preheat,” to be published in *Physics of Plasmas*.

J. Hinz, V. V. Karasiev, S. X. Hu, M. Zaghou, D. Mejía-Rodríguez, S. B. Trickey, and L. Calderin, “Fully Consistent Density Functional Theory Determination of the Insulator-Metal Transition Boundary in Warm Dense Hydrogen,” to be published in *Physical Review Research*.

B. N. Hoffman, A. A. Kozlov, N. Liu, H. Huang, J. B. Oliver, A. L. Rigatti, T. J. Kessler, A. A. Shestopalov, and S. G. Demos, “Mechanisms of Picosecond Laser-Induced Damage in Common Multilayer Dielectric Gratings,” to be published in *Optics Express*.

G. W. Jenkins, C. Feng, and J. Bromage, “Overcoming Gas Ionization Limitations with Divided-Pulse Nonlinear Compression,” to be published in *Optics Express*.

T. Z. Kosc, H. Huang, T. J. Kessler, R. A. Negres, and S. G. Demos, “Determination of the Raman Polarizability Tensor in the Optically Anisotropic Crystal Potassium Dihydrogen Phosphate and Its Deuterated Analog,” to be published in *Scientific Reports*.

A. L. Kritcher, D. C. Swift, T. Döppner, B. Bachmann, L. X. Benedict, G. W. Collins, J. L. DuBois, F. Elsner, G. Fontaine, J. A. Gaffney, S. Hamel, A. Lazicki, W. R. Johnson, N. Kostinski, D. Kraus, M. J. MacDonald, B. Maddox, M. E. Martin, P. Neumayer, A. Nikroo, J. Nilsen, B. A. Remington, D. Saumon, P. A. Sterne, W. Sweet, A. A. Correa, H. D. Whitley, R. W. Falcone, and S. H. Glenzer, “A Measurement of the Equation of State of Carbon Envelopes of White Dwarfs,” to be published in *Nature*.

A. V. Maximov, J. G. Shaw, and J. P. Palastro, “Nonlinear Transmission of Laser Light Through Coronal Plasma Due to Self-Induced Incoherence,” to be published in *Physical Review E*.

R. Paul, S. X. Hu, V. V. Karasiev, S. A. Bonev, and D. N. Polsin, “Thermal Effects on the Electronic Properties of Sodium Electride Under High Pressures,” to be published in *Physical Review B*.

M. Sharpe, W. T. Shmayda, and K. Glance, “Measurement of Palladium Hydride and Palladium Deuteride Isotherms

between 130 K and 393 K,” to be published in *Fusion Science and Technology*.

D. B. Sinars, M. A. Sweeney, C. S. Alexander, D. J. Ampleford, T. Ao, J. P. Apruzese, C. Aragon, D. J. Armstrong, K. N. Austin, T. J. Awe, A. D. Baczewski, J. E. Bailey, K. L. Baker, C. R. Ball, H. T. Barclay, S. Beatty, K. Beckwith, K. S. Bell, J. F. Benage, N. L. Bennett, K. Blaha, D. E. Bliss, J. J. Boerner, C. J. Bourdon, B. A. Branch, J. L. Brown, E. M. Campbell, R. B. Campbell, D. G. Chacon, G. A. Chandler, K. Chandler, P. J. Christenson, M. D. Christison, E. B. Christner, R. C. Clay, K. R. Cochrane, A. P. Colombo, B. M. Cook, C. A. Coverdale, M. E. Cuneo, J. S. Custer, A. Dasgupta, J.-P. Davis, M. P. Desjarlais, D. H. Dolan, J. D. Douglass, G. S. Dunham, S. Duwal, A. D. Edens, M. J. Edwards, E. G. Evstatiev, B. G. Farfan, J. R. Fein, E. S. Field, J. A. Fisher, T. M. Flanagan, D. G. Flicker, M. D. Furnish, B. R. Galloway, P. D. Gard, T. A. Gardiner, M. Geissel, J. L. Giuliani, M. E. Glinsky, M. R. Gomez, G. P. Grim, K. D. Hahn, T. A. Hail, N. D. Hamlin, J. H. Hammer, S. B. Hansen, H. L. Hanshaw, E. C. Harding, A. J. Harvey-Thompson, D. Headley, M. C. Herrmann, M. H. Hess, C. Highstrete, O. A. Hurricane, B. T. Hutsel, C. A. Jennings, O. M. Johns, D. Johnson, M. D. Johnston, B. M. Jones, M. C. Jones, P. A. Jones, P. E. Kalita, R. J. Kamm, J. W. Kellogg, M. L. Kiefer, M. W. Kimmel, P. F. Knapp, M. D. Knudson, A. Kreft, G. R. Laity, P. W. Lake, D. C. Lamma, W. L. Langston, J. S. Lash, K. R. LeChien, J. J. Leckbee, R. J. Leeper, G. T. Leifeste, R. W. Lemke, W. Lewis, S. A. Lewis, G. P. Loisel, Q. M. Looker, A. J. Lopez, D. J. Lucero, S. A. MacLaren, R. J. Magyar, M. A. Mangan, M. R. Martin, T. R. Mattsson, M. K. Matzen, A. J. Maurer, M. G. Mazarakis, R. D. McBride, H. S. McLean, C. A. McCoy, G. R. McKee, J. L. McKenney, A. R. Miles, J. A. Mills, M. D. Mitchell, N. W. Moore, C. E. Myers, T. Nagayama, G. Natoni, A. C. Owen, S. Patel, K. J. Peterson, T. D. Pointon, J. L. Porter, A. J. Porwitzky, S. Radovich, K. S. Raman, P. K. Rambo, W. D. Reinhart, G. K. Robertson, G. A. Rochau, S. Root, D. V. Rose, D. C. Rovang, C. L. Ruiz, D. E. Ruiz, D. Sandoval, M. E. Savage, M. E. Sceiford, M. A. Schaeuble, P. F. Schmit, M. S. Schollmeier, J. Schwarz, C. T. Seagle, A. B. Sefkow, D. B. Seidel, G. A. Shipley, J. Shores, L. Shulenburger, S. C. Simpson, S. A. Slutz, I. C. Smith, C. S. Speas, P. E. Specht, M. J. Speir, D. C. Spencer, P. T. Springer, A. M. Steiner, B. S. Stolzhus, W. A. Stygar, J. Ward Thornhill, J. A. Torres, J. P. Townsend, C. Tyler, R. A. Vesey, P. E. Wakeland, T. J. Webb, E. A. Weinbrecht, M. R. Weis, D. R. Welch, J. L. Wise, M. Wu, D. A. Yager-Elorriaga, A. Yu, and E. P. Yu, “Review of Pulsed-Power-Driven High-Energy-Density Physics Research on Z at Sandia,” to be published in *Physics of Plasmas*.

R. Sobolewski, “Optical Detectors and Sensors,” to be published in the Handbook of Superconducting Materials.

S. Tochitsky, A. Pak, F. Fiuza, D. Haberberger, N. Lemos, A. Link, D. H. Froula, and C. Joshi, “Laser-Driven Collisionless Shock Acceleration of Ions from Near-Critical Plasmas,” to be published in Physics of Plasmas.

S. Zhang and S. X. Hu, “Species Separation and Hydrogen Streaming upon Shock Release from Polystyrene Under Inertial Confinement Fusion Conditions,” to be published in Physical Review Letters.

S. Zhang, H. D. Whitley, and T. Ogitsu, “Phase Transformation in Boron Under Shock Compression,” to be published in Solid State Sciences.

Conference Presentations

The following presentations were made at the APS April Meeting, virtual, 18–21 April 2020:

C. J. Forrest, G. Hale, W. U. Schröder, J. P. Knauer, P. B. Radha, V. Yu. Glebov, O. M. Mannion, Z. L. Mohamed, S. P. Regan, T. C. Sangster, A. Schwemmlin, and C. Stoeckl, “Evidence for a ${}^7\text{Li}$ State at $E_x = 10.2$ MeV from Inelastic Neutron Scattering at 14 MeV.”

A. K. Schwemmlin, W. U. Schröder, C. Stoeckl, C. J. Forrest, J. P. Knauer, and S. P. Regan, “Using the Multi-Terawatt Laser at the Laboratory for Laser Energetics to Generate a High-Yield, 0.5-MeV Deuteron Beam.”

The following presentations were made at Technology of Fusion Energy (TOFE) 2020, virtual, 20–23 April 2020:

C. Fagan, M. Sharpe, W. T. Shmayda, and W. U. Schröder, “Tritium Concentration Profiles in Stainless-Steel 316 Samples.”

M. Sharpe, W. T. Shmayda, J. Wermer, and C. A. Bond, “Permeation Rate of Deuterium and Tritium Through Iron–Chromium–Aluminum Alloys.”

The following presentations were made at High Energy Density Science, virtual, 20–24 April 2020:

S. P. Regan, V. N. Goncharov, T. C. Sangster, R. Betti, E. M. Campbell, K. A. Bauer, M. J. Bonino, D. Cao, A. R. Christopherson, G. W. Collins, T. J. B. Collins, R. S. Craxton, D. H. Edgell, R. Epstein, P. Fan, M. Farrell,

P. Fitzsimmons, C. J. Forrest, R. K. Follett, J. A. Frenje, D. H. Froula, M. Gatu Johnson, V. Yu. Glebov, V. Gopalaswamy, D. R. Harding, S. X. Hu, H. Huang, I. V. Igumenshchev, Y. Lu, R. Luo, D. W. Jacobs-Perkins, R. T. Janezic, M. Karasik, T. J. Kessler, J. P. Knauer, T. Z. Kosc, A. Lees, O. M. Mannion, J. A. Marozas, F. J. Marshall, P. W. McKenty, Z. L. Mohamed, S. F. B. Morse, P. M. Nilson, S. P. Obenschain, J. P. Palastro, D. Patel, J. L. Peebles, R. D. Petrasso, P. B. Radha, H. G. Rinderknecht, M. J. Rosenberg, S. Sampat, A. J. Schmitt, W. Seka, R. C. Shah, J. R. Rygg, J. G. Shaw, W. T. Shmayda, M. J. Shoup III, C. Shulberg, A. Shvydky, A. A. Solodov, C. Sorce, C. Stoeckl, W. Sweet, W. Theobald, D. Turnbull, J. Ulreich, L. J. Waxer, M. D. Wittman, K. M. Woo, and J. D. Zuegel, “Laser-Direct-Drive Inertial Confinement Fusion Research on OMEGA: Current Status.”

J. J. Ruby, J. R. Rygg, D. A. Chin, C. J. Forrest, V. Yu. Glebov, C. Stoeckl, N. V. Kabadi, P. Adrian, B. Bachmann, Y. Ping, J. A. Gaffney, and G. W. Collins, “Spherical Shock Wave Experiments on the OMEGA Laser.”

G. W. Collins, “Laboratory for Laser Energetics Contributions to the Stockpile Stewardship Mission,” presented at the HEDP Briefing to DOE, virtual, 29 April 2019.

The following presentations were made at CLEO 2020, virtual, 10–15 May 2020:

I. A. Begishev, V. V. Ivanov, S. Patankar, P. S. Datte, S. T. Yang, J. D. Zuegel, and J. Bromage, “Nonlinear Crystals for Efficient High-Energy Fifth-Harmonic Generation of Near-IR Lasers.”

C. Dorrer, I. A. Begishev, S.-W. Bahk, and J. Bromage, “Broadband Parametric-Gain Optimization of Partially Deuterated KDP with Two-Wavelength Tuning Curves.”

C. Dorrer, E. M. Hill, and T. Borger, “Record-Bandwidth Spectrally Incoherent UV Laser Pulses.”

C. Dorrer, E. M. Hill, and J. D. Zuegel, “High-Efficiency Parametric Amplification of Broadband Spectrally Incoherent Pulses.”

D. H. Froula, S.-W. Bahk, I. A. Begishev, R. Boni, J. Bromage, A. Davies, P. Franke, R. K. Follett, D. Haberberger, A. Howard, G. W. Jenkins, J. Katz, T. J. Kessler, J. P. Palastro, J. B. Oliver, D. Ramsey, T. Simpson, J. L. Shaw, D. Turnbull, N. Vafaei-Najafabadi, and J. Vieira, “From Chromatic to Achromatic Flying Foci.”

V. Gruzdev and K. R. P. Kafka, “Ultrafast Multiphoton Absorption in Optical-Coating Materials at Near-Damage-Threshold Fluence.”

E. P. Power, J. Bromage, and J. D. Zuegel, “Integrated-Flow Active Cooling for Thermal Management of Reflective Optics Under High-Average-Power Load.”

E. M. Campbell, “Direct-Drive Laser Fusion, Status, Plans, and the Future,” presented at the Cornell University Talk, virtual, 11 May 2020.

D. H. Froula, J. P. Palastro, S.-W. Bahk, I. V. Begishev, R. Boni, J. Bromage, A. Davies, P. Franke, R. K. Follett, D. Haberberger, A. Howard, G. W. Jenkins, J. Katz, T. J. Kessler, J. B. Oliver, D. Ramsey, T. Simpson, J. L. Shaw, D. Turnbull, N. Vafaei-Najafabadi, and J. Vieira, “Progress in Flying Focus for Plasma-Based Applications: From Chromatic to Achromatic Flying Foci,” presented at UR Colloquia, virtual, 17 June 2020.

E. M. Campbell, “Laboratory for Laser Energetics (LLE) Contributions to the Stockpile Stewardship Mission,” presented at OES Executives Meeting, virtual, 23 June 2020.

D. R. Harding, S. M. Fess, M. J. Bonino, R. F. Earley, T. C. Sangster, E. M. Campbell, V. N. Goncharov, J. L. Peebles, M. D. Wittman, C. Stoeckl, Y.-F. Lu, P. Fan, and X. Huang, “Laser-Based Microfabrication and Metrology of Laser-Driven Inertial Fusion Targets,” presented at the 21st International Symposium on Laser Precision Microfabrication, virtual, 23–26 June 2020.

G. W. Collins, “High Energy Density (HED) Quantum Matter,” presented at the Office of Science Meeting, virtual, 29 June 2020.

